

**AN INVESTIGATION OF THE RELATIONSHIPS BETWEEN
 m_{bLg} AND M_w AND BETWEEN $m_{Lg}(f)$ AND M_w USING
RECENT UNITED STATES EARTHQUAKES
AND RANDOM VIBRATION THEORY**

Christopher Rigsby, B.S.

An Abstract Presented to the Graduate Faculty of
Saint Louis University in Partial Fulfillment
of the Requirements for the Degree of
Master of Science (Research)

2012

Abstract

The $m_{Lg}(f)$ magnitude is an important regional magnitude scale because of the ease of its calculation and because the Lg phase is a prominent phase observed in eastern North America as a result of paths in the continental platform and the Canadian Shield. A variant of $m_{Lg}(f)$ employed by the National Earthquake Information Center (NEIC) of the United States Geological Survey (USGS) is m_{bLg} , a magnitude scale that uses the Lg phase but does not explicitly include the frequency of the phase in the computation.

We derive empirical relationships between M_w and m_{bLg} and between M_w and $m_{Lg}(f)$. We use random vibration theory to model the relationships between M_w and m_{bLg} and between M_w and $m_{Lg}(f)$ in order to address seismic source scaling and in order to determine the Lg magnitude range over which the empirical predictive relationships are valid. We address whether a single-valued γ , a measure of anelastic attenuation, is appropriate for the central and eastern United States.

**AN INVESTIGATION OF THE RELATIONSHIPS BETWEEN
 m_{bLg} AND M_w AND BETWEEN $m_{Lg}(f)$ AND M_w USING
RECENT UNITED STATES EARTHQUAKES
AND RANDOM VIBRATION THEORY**

Christopher Rigsby, B.S.

A Thesis Presented to the Graduate Faculty of
Saint Louis University in Partial Fulfillment
of the Requirements for the Degree of
Master of Science (Research)

2012

COMMITTEE IN CHARGE OF CANDIDACY

Professor Robert B. Herrmann
Chairperson and Advisor

Associate Professor Lupei Zhu

Assistant Professor Linda M. Warren

Acknowledgements

I wish to thank Dr. Robert B. Herrmann for his tireless patience, thorough explanations, and dedication to teaching and research. Without his vast knowledge of geophysics, physics, geology, programming, and mathematics, among other fields, I would not have been able to complete this thesis nor gain as much as I have from the graduate program.

I wish to thank Dr. Linda M. Warren and Dr. Lupei Zhu for their time and helpful comments in order to improve this writing.

I wish to thank Dr. David J. Crossley for his advice and especially for his teaching of Time Series in Geophysics.

I wish to thank Dr. John P. Encarnación for his clear geological explanations and for his delightful analogies.

I wish to thank Laurie Hausmann and Karen Nydegger for their help and their diligence.

I wish to thank my fellow graduate students who aided me in classes and research.

Finally, I wish to thank my friend and partner, Jennifer Stone, for her support and tolerance during my graduate years.

Table of Contents

List of Tables	v
List of Figures	vi
Chapter 1: Introduction	1
1.1 Purpose of Current Study.....	1
1.2 Review of Literature	1
Chapter 2: Method 1 Calculation of m_{bLg} and $m_{Lg}(f)$	8
2.1 Empirical Data Set	8
2.2 Method 1 Calculation of m_{bLg} for Central and Eastern US Earthquakes	8
2.3 Method 1 Calculation of $m_{Lg}(f)$	13
2.4 Method 1 m_{bLg} Results and Discussion	15
2.5 Method 1 $m_{Lg}(f)$ Results and Discussion	19
2.6 Comparisons of Method 1 m_{bLg} , Method 1 $m_{Lg}(f)$, and published m_{bLg}	22
2.7 Adjustments to the Method 1 Lg magnitude relationships	25
2.8 Residuals for Method 1 m_{bLg} and $m_{Lg}(f)$	29
Chapter 3: Method 2 Calculation of m_{bLg} and $m_{Lg}(f)$	34
3.1 Empirical Data Set	34
3.2 Method 2 Calculation of m_{bLg} for Central and Eastern US Earthquakes ..	34
3.3 Method 2 Calculation of $m_{Lg}(f)$	38
3.4 Method 2 m_{bLg} Results and Discussion	40
3.5 Method 2 $m_{Lg}(f)$ Results and Discussion	42
3.6 Comparisons of Method 1 m_{bLg} , Method 1 $m_{Lg}(f)$, Method 2 m_{bLg} , and Method 2 $m_{Lg}(f)$	44
3.7 Adjustments to the Method 2 Lg magnitude relationships	44
Chapter 4: Modeling	50
4.1 Stochastic Method	50
4.2 Random Vibration Theory	51
4.3 Models	53
4.4 Modeling m_{bLg} versus M_w	54
4.5 Modeling $m_{Lg}(f)$ versus M_w	61
4.6 Modeling a modified m_{bLg} versus M_w	65
4.7 Modeling a modified $m_{Lg}(f)$ versus M_w	69
Chapter 5: An Examination of γ	73
5.1 Model for Ground Motion	73
5.2 Results and Discussion	74
Chapter 6: Summary and Conclusions	88

References 91
Vita Auctoris 94

List of Tables

Table 2.1:	The table lists the parameters for the WWSSN short-period velocity response	11
Table 2.2:	The table lists the parameters for the WWSSN short-period displacement response	12
.Table 3.1:	The table lists the parameters for the WWSSN short-period velocity response	37
Table 4.1:	Frankel <i>et al.</i> hard-rock model parameters	55
Table 4.2:	Frankel <i>et al.</i> modified hard-rock model parameters. The modified hard-rock model contains a different site effect term	56
Table 4.3:	Atkinson and Boore model parameters	57
Table 5.1:	Earthquake dates, M_w , Method 1 m_{bLg} , Method 1 $m_{Lg}(f)$, and associated coefficients of anelastic attenuation. The last 2 columns gives coefficients of anelastic attenuation for different distance ranges	75

List of Figures

- Figure 2.1: A map of the locations of the epicenters (yellow stars) of the 38 earthquakes for which magnitudes were calculated. The stations (red dots) include every station that recorded motion from any of the earthquakes. The Method 1 calculation of magnitudes eliminated many seismograms, and thus only a subset of stations was used for any given earthquake ... 9
- Figure 2.2: The velocity response of the WWSSN short-period instrument. 11
- Figure 2.3: The displacement response of the WWSSN short-period instrument. The constant was adjusted so that the gain at 1 Hz is 1. Note that the displacement response $D(f) = (i2\pi f)V(f)$ where $V(f)$ is the complex velocity response for the instrument 12
- Figure 2.4: Flowchart for Method 1 calculation of m_{bLg} 14
- Figure 2.5: Regression analysis for Method 1 m_{bLg} . The red line is the regression line, the inner blue lines are the confidence intervals, and the outer blue lines are the prediction intervals 16
- Figure 2.6: A comparison of the regression analyses for Method 1 m_{bLg} and the published data for the NEIC m_{bLg} 18
- Figure 2.7: Regression analysis for Method 1 $m_{Lg}(f)$. The red line is the regression line, the inner blue lines are the confidence intervals, and the outer blue lines are the prediction intervals 20
- Figure 2.8: A comparison of the regression analyses for Method 1 $m_{Lg}(f)$ and the published data for the NEIC m_{bLg} 21
- Figure 2.9: A plot of the Method 1 m_{bLg} versus the published NEIC m_{bLg} for the 19 earthquakes common to both groups. A 1-to-1 reference line is shown .. 23
- Figure 2.10: A plot of the Method 1 $m_{Lg}(f)$ versus the published NEIC m_{bLg} for the 19 earthquakes common to both groups. A 1-to-1 reference line is shown .. 24
- Figure 2.11: A plot of the Method 1 m_{bLg} versus the Method 1 $m_{Lg}(f)$ for all 38 earthquakes used in Method 1. A 1-to-1 reference line is shown 26
- Figure 2.12: A regression graph of the M_w (SLU) versus the Method 1 m_{bLg} based on a bilinear division. Modeling, described in Chapter 4, and empirical iterations of a regression program suggest that the regression line slope change at around $m_{bLg} = 4.5$. For the regression line for smaller magnitudes, the

	slope is fixed at 2/3. For the regression line for larger magnitudes, the slope is determined by the data	27
Figure 2.13:	A regression graph of the the M_w (SLU) versus the Method 1 $m_{Lg}(f)$ based on a bilinear division. Modeling, described in Chapter 4, and empirical iterations of a regression program suggest that the regression line slope change at around $m_{Lg}(f) = 4.5$	28
Figure 2.14:	A regression analysis of Method 1 m_{bLg} in which the maximum peak-to-peak amplitude, rather than the third-largest peak-to-peak amplitude, is used in the calculation of m_{bLg}	30
Figure 2.15:	A regression analysis of Method 1 $m_{Lg}(f)$ in which the maximum peak-to-peak amplitude, rather than the third-largest peak-to-peak amplitude, is used in the calculation of $m_{Lg}(f)$	31
Figure 2.16:	The Method 1 m_{bLg} residuals for each individual earthquake are overlaid (<i>top</i>), and the standard deviation of those residuals is given. The Method 1 $m_{Lg}(f)$ residuals for each individual earthquake are overlaid (<i>bottom</i>), and the the standard deviation of those residuals is given	32
Figure 3.1:	A map of the locations of the epicenters (yellow stars) of the 35 earthquakes for which magnitudes were calculated. The stations (red dots) include every station that recorded motion from any of the earthquakes. The Method 2 calculation of magnitudes eliminated many seismograms, and thus only a subset of stations was used for any given earthquake ..	35
Figure 3.2:	The velocity response of the WWSSN short-period instrument	37
Figure 3.3:	Flowchart for Method 2 calculation of m_{bLg}	39
Figure 3.4:	Regression analysis for the Method 2 m_{bLg} compared against the regression analysis for the Method 1 m_{bLg} . The red line is the regression line, the inner blue lines are the confidence intervals, and the outer blue lines are the prediction intervals	41
Figure 3.5:	Regression analysis for Method 2 $m_{Lg}(f)$ compared against the regression analysis for Method 1 $m_{Lg}(f)$. The red line is the regression line, the inner blue lines are the confidence intervals, and the outer blue lines are the prediction intervals	43
Figure 3.6:	A plot of the Method 2 m_{bLg} versus the Method 1 m_{bLg} for the 35 earthquakes common to both groups	45

Figure 3.7: A plot of the Method 2 $m_{Lg}(f)$ versus the Method 1 $m_{Lg}(f)$ for the 35 earthquakes common to both groups 46

Figure 3.8: A regression graph of the M_w (SLU) versus the Method 2 m_{bLg} based on a bilinear division. Modeling, described in Chapter 4, and empirical iterations of a regression program suggest that the regression line slope change at around $m_{bLg} = 4.3$. For the regression line for smaller magnitudes, the slope is fixed at $2/3$. For the regression line for larger magnitudes, the slope is determined by the data 47

Figure 3.9: A regression graph of the M_w (SLU) versus the Method 2 $m_{Lg}(f)$ based on a bilinear division. Modeling, described in Chapter 4, and empirical iterations of a regression program suggest that the regression line slope change at around $m_{Lgi}(f) = 4.4$ 49

Figure 4.1: The Method 1 m_{bLg} data points lie over the m_{bLg} versus M_w relationship derived from the Frankel hard-rock model. The green, red, and black curves give the relationships between m_{bLg} and M_w for different constant epicentral distances. The model uses the instrument-corrected maximum zero-to-peak amplitude, while the Method 1 m_{bLg} points use half the instrument-corrected third-largest peak-to-peak amplitude 58

Figure 4.2: The Method 1 m_{bLg} data points lie over the m_{bLg} versus M_w relationship derived from the Frankel modified hard-rock model. The green, red, and black curves give the relationships between m_{bLg} and M_w for different constant epicentral distances. The model uses the instrument-corrected maximum zero-to-peak amplitude, while the Method 1 m_{bLg} points use half the instrument-corrected third-largest peak-to-peak amplitude..... 59

Figure 4.3: The Method 1 m_{bLg} data points lie over the m_{bLg} versus M_w relationship derived from the Atkinson-Boore model. The green, red, and black curves give the relationships between m_{bLg} and M_w for different constant epicentral distances. The model uses the instrument-corrected maximum zero-to-peak amplitude, while the Method 1 m_{bLg} points use half the instrument-corrected third-largest peak-to-peak amplitude 59

Figure 4.4: The Method 1 $m_{Lg}(f)$ data points lie over the $m_{Lg}(f)$ versus M_w relationship derived from the Frankel hard-rock model. The green, red, and black curves give the relationship between $m_{Lg}(f)$ and M_w for different constant epicentral distances. The model uses the instrument-corrected maximum zero-to-peak amplitude, while the Method 1 $m_{Lg}(f)$ points use half the instrument-corrected third-largest peak-to-peak amplitude 62

Figure 4.5: The Method 1 $m_{Lg}(f)$ data points lie over the $m_{Lg}(f)$ versus M_w

relationship derived from the modified Frankel hard-rock model. The green, red, and black curves give the relationship between $m_{Lg}(f)$ and M_w for different constant epicentral distances. The model uses the instrument-corrected maximum zero-to-peak amplitude, while the Method 1 $m_{Lg}(f)$ points use half the instrument-corrected third-largest peak-to-peak amplitude 63

Figure 4.6: The Method 1 $m_{Lg}(f)$ data points lie over the $m_{Lg}(f)$ versus M_w relationship derived from the Atkinson-Boore model. The green, red, and black curves give the relationships between $m_{Lg}(f)$ and M_w for different constant epicentral distances. The model uses the instrument-corrected maximum zero-to-peak amplitude, while the Method 1 $m_{Lg}(f)$ points use half the instrument-corrected third-largest peak-to-peak amplitude 64

Figure 4.7: The Method 1 m_{bLg} data points lie over the m_{bLg} versus M_w relationship derived from the Frankel hard-rock model. The green, red, and black curves give the relationships between m_{bLg} and M_w for different constant epicentral distances. The model uses the instrument-corrected maximum zero-to-peak amplitude, while the Method 1 m_{bLg} points use half the instrument-corrected maximum peak-to-peak amplitude 66

Figure 4.8: The Method 1 m_{bLg} data points lie over the m_{bLg} versus M_w relationship derived from the modified Frankel hard-rock model. The green, red, and black curves give the relationships between m_{bLg} and M_w for different constant epicentral distances. The model uses the instrument-corrected maximum peak-to-peak amplitude, while the Method 1 m_{bLg} points use half the instrument-corrected maximum peak-to-peak amplitude 67

Figure 4.9: The Method 1 m_{bLg} data points lie over the m_{bLg} versus M_w relationship derived from the Atkinson-Boore model. The green, red, and black curves give the relationships between m_{bLg} and M_w for different constant epicentral distances. The model uses the instrument-corrected maximum zero-to-peak amplitude, while the Method 1 m_{bLg} points use half the instrument-corrected maximum peak-to-peak amplitude 68

Figure 4.10: The Method 1 $m_{Lg}(f)$ data points lie over the $m_{Lg}(f)$ versus M_w relationship derived from the modified Frankel hard-rock model. The green, red, and black curves give the relationships between $m_{Lg}(f)$ and M_w for different constant epicentral distances. The model uses the instrument-corrected maximum zero-to-peak amplitude, while the Method 1 $m_{Lg}(f)$ points use half the instrument-corrected maximum peak-to-peak amplitude 70

Figure 4.11: The Method 1 $m_{Lg}(f)$ data points lie over the $m_{Lg}(f)$ versus M_w

relationship derived from the Frankel hard-rock model. The green, red, and black curves give the relationships between $m_{Lg}(f)$ and M_w for different constant epicentral distances. The model uses the instrument-corrected maximum zero-to-peak amplitude, and the Method 1 $m_{Lg}(f)$ points use half the instrument-corrected maximum peak-to-peak amplitude 71

- Figure 4.12: The Method 1 $m_{Lg}(f)$ data points lie over the $m_{Lg}(f)$ versus M_w relationship derived from the Atkinson-Boore model. The green, red, and black curves give the relationships between $m_{Lg}(f)$ and M_w for different constant epicentral distances. The model uses the instrument-corrected maximum zero-to-peak amplitude, while the Method 1 $m_{Lg}(f)$ points use half the instrument-corrected maximum peak-to-peak amplitude 72
- Figure 5.1: The linear least-squares regression analysis is shown for the 15 January 2010 earthquake. Two distance ranges, 50-1200 km (*top*) and all distances (*bottom*), are illustrated, and the accompanying M_w , Method 1 m_{bLg} , and Method 1 $m_{Lg}(f)$ are given..... 77
- Figure 5.2: The linear least-squares regression analysis is shown for the 27 February 2010 earthquake. Two distance ranges, 50-1200 km (*top*) and all distances (*bottom*), are illustrated, and the accompanying M_w , Method 1 m_{bLg} , and Method 1 $m_{Lg}(f)$ are given 78
- Figure 5.3: The linear least-squares regression analysis is shown for the 13 October 2010 earthquake. Two distance ranges, 50-1200 km (*top*) and all distances (*bottom*), are illustrated, and the accompanying M_w , Method 1 m_{bLg} , and Method 1 $m_{Lg}(f)$ are given 79
- Figure 5.4: The linear least-squares regression analysis is shown for the 20 November 2010 earthquake. Two distance ranges, 50-1200 km (*top*) and all distances (*bottom*), are illustrated, and the accompanying M_w , Method 1 m_{bLg} , and Method 1 $m_{Lg}(f)$ are given. 80
- Figure 5.5: The linear least-squares regression analysis is shown for the 24 November 2010 earthquake. Two distance ranges, 50-1200 km (*top*) and all distances (*bottom*), are illustrated, and the accompanying M_w , Method 1 m_{bLg} , and Method 1 $m_{Lg}(f)$ are given 81
- Figure 5.6: The linear least-squares regression analysis is shown for the 18 February 2011 earthquake. Two distance ranges, 50-1200 km (*top*) and all distances (*bottom*), are illustrated, and the accompanying M_w , Method 1 m_{bLg} , and Method 1 $m_{Lg}(f)$ are given 82
- Figure 5.7: The linear least-squares regression analysis is shown for the 28 February

2011 earthquake. Two distance ranges, 50-1200 km (*top*) and all distances (*bottom*), are illustrated, and the accompanying M_w , Method 1 m_{bLg} , and Method 1 $m_{Lg}(f)$ are given 83

Figure 5.8: The linear least-squares regression analysis is shown for the 6 November 2011 earthquake. Two distance ranges, 50-1200 km (*top*) and all distances (*bottom*), are illustrated, and the accompanying M_w , Method 1 m_{bLg} , and Method 1 $m_{Lg}(f)$ are given 84

Figure 5.9: The linear least-squares regression analysis is shown for the 5 November 2011 earthquake. Two distance ranges, 50-1200 km (*top*) and all distances (*bottom*), are illustrated, and the accompanying M_w , Method 1 m_{bLg} , and Method 1 $m_{Lg}(f)$ are given 85

Figure 5.10: The linear least-squares regression analysis is shown for the 8 November 2011 earthquake. Two distance ranges, 50-1200 km (*top*) and all distances (*bottom*), are illustrated, and the accompanying M_w , Method 1 m_{bLg} , and Method 1 $m_{Lg}(f)$ are given 86

CHAPTER 1: Introduction

1.1 Purpose of Current Study

The $m_{Lg}(f)$ magnitude is an important regional magnitude scale because of the ease of its calculation and because the Lg phase is a prominent phase observed in eastern North America as a result of paths in the continental platform and the Canadian Shield. A variant of $m_{Lg}(f)$ employed by the National Earthquake Information Center (NEIC) of the United States Geological Survey (USGS) is m_{bLg} , a magnitude scale that uses the Lg phase but does not explicitly include the frequency of the phase in the computation.

Since the preferred magnitude scale of the NEIC is the moment magnitude M_w , which is the basis for the ShakeMap and other products of the NEIC, determining associations between M_w and the NEIC m_{bLg} and between M_w and $m_{Lg}(f)$ is extremely important. Thus, the primary aims of the current study are (1) to understand the relationship between M_w and m_{bLg} and (2) to understand the relationship between $m_{Lg}(f)$ and M_w . Other objectives are (1) to model the relationships between M_w and m_{bLg} and between M_w and $m_{Lg}(f)$ using random vibration theory simulations in a way that addresses seismic source scaling and (2) to answer the question of whether a single-valued γ , a measure of anelastic attenuation, is appropriate for the central and eastern United States.

1.2 Review of Literature

Press and Ewing (1952) first identified two large-amplitude surface waves on seismograms from Palisades, New York. One of the surface waves had an onset period of 0.5 – 6 seconds, a group velocity of 3.44 – 3.58 km/s, and movement primarily in the vertical and transverse directions (Press and Ewing, 1952). Because the velocity was consistent with Love waves and appeared only for continental crustal paths, Press and Ewing (1952) labeled the waves *Lg*. Oliver and Ewing (1957, 1958) recognized that the *Lg* phase contains P-SV and SH motion. Ewing *et al.* (1957) noted that the efficient transmission of energy indicated a coherent waveguide and that a lateral length of as little as 220 km of oceanic crustal path could prevent the formation of the phase.

Subsequent investigators refined the characteristics of the *Lg* wave. Herrmann and Kijko (1983b) modeled the vertical motion of a World-Wide Standard Seismograph Network (WWSSN) short-period seismogram and showed that higher-mode Rayleigh waves accounted for the vertical motion. Kennett (1983, 1986) showed that synthetic seismograms from higher-mode surface waves, both Rayleigh and Love, matched observed seismograms well and that changes in the continental crustal thickness, especially decreasing the thickness, significantly attenuated or eliminated the phase. Using finite-difference modeling and normal-mode analysis, Zhang and Lay (1995) explained the absence of *Lg* waves in the oceanic crust as a result of fewer modes, in the frequency range 0.3 – 2 Hz, for a nominal 6 km thick oceanic crust; they also demonstrated that 15 km thick continental crust is typically sufficiently stable for the development of the *Lg* phase.

Nuttli (1973) defined a magnitude scale by associating an *Lg* amplitude, with a

frequency near 1 Hz observed on a WWSSN short-period seismograph, with an m_b magnitude. The resulting magnitude was called m_{bLg} :

$$m_{bLg} = 3.75 + 0.90\log_{10}(\Delta) + \log_{10}\left(\frac{A}{T}\right) \text{ for } 0.5^\circ \leq \Delta \leq 4^\circ \quad (1.1)$$

$$m_{bLg} = 3.30 + 1.66\log_{10}(\Delta) + \log_{10}\left(\frac{A}{T}\right) \text{ for } 4.0^\circ \leq \Delta \leq 30^\circ \quad (1.2)$$

where Δ is the epicentral distance in degrees, A is the instrument-corrected third-largest zero-to-peak amplitude in μm , and T is the period in s. In addition to developing the m_{bLg} scale, Nuttli (1973) determined that γ , the coefficient of anelastic attenuation, had an average value of 0.0006 km^{-1} for the central United States.

Because the original Nuttli (1973) definition of the m_{bLg} was valid only for 1 Hz Lg waves recorded on a WWSSN short-period seismograph and because some seismologists noted potential problems with the definition, Herrmann and Kijko (1983a) revised the definition to account for the instrument-corrected amplitude at a given frequency, labeling the revised magnitude $m_{Lg}(f)$ to explicitly emphasize the frequency used. Further, they dropped the b subscript in order to avoid the implication that the $m_{Lg}(f)$ is equivalent to the teleseismic body wave magnitude. Herrmann and Kijko (1983a) defined $m_{Lg}(f)$ as

$$m_{Lg}(f) = 2.94 + 0.8333\log_{10}\left(\frac{r}{10}\right) + .4342\gamma r + \log_{10}A \quad (1.3)$$

where f is the frequency in Hz, r is the epicentral distance in km, γ is the coefficient of anelastic attenuation in km^{-1} , and A is the instrument-corrected ground amplitude in μm .

For the central United States, Herrmann and Kijko (1983) used $\gamma = 0.001f^{0.7}$.

Herrmann (1987) studied broadband magnitudes from Lg data and suggested that the $m_{Lg}(f)$ must be modified if the objective is to learn about source spectrum scaling:

$$m_{Lg}(f)_{mod} = m_{Lg}(f) + \log_{10} T^{\frac{1}{2}} \quad (1.4)$$

where the parameters are the same as in $m_{Lg}(f)$. The $m_{Lg}(f)_{mod}$ is expected to vary as $\log S(f)$ where $S(f)$ is the source spectrum.

While devising an estimate of m_b and yield for explosions using Lg waves, Nuttli (1986a, 1986b) measured Lg waves observed on WWSSN short-period seismograms in the group velocity window of 3.2 to 3.6 km/s and found that the associated periods were always between 0.7 and 1.3 s; he then defined an Lg magnitude of 5 as having 115 μm of motion for a seismograph 10 km away from the source. The NEIC currently employs a version of the Herrmann-Kijko $m_{Lg}(f)$ and calls its magnitude m_{bLg} :

$$m_{bLg} = 2.96 + 0.8333 \log_{10} \left(\frac{r}{10} \right) + .4343 \gamma r + \log_{10} A \quad \text{for } 50 \text{ km} \leq r \leq 1110 \text{ km} \quad (1.5)$$

where r is the epicentral distance in km, $\gamma = 0.00063 \text{ km}^{-1}$, and A is half the instrument-corrected third-largest peak-to-peak amplitude in μm as measured on a seismogram emulating the response of the WWSSN short-period instrument with group velocity in the range 3.2–3.6 km/s and periods 0.7–1.3 s (Magnitude WG, 2011).

Aki (1966) defined the moment of an earthquake as the following:

$$M_0 = \mu AD \quad (1.6)$$

in which μ is the shear modulus of the rock in dyne/cm², A is the area of the rupture in cm², D is the average displacement in cm, and M_0 is the scalar seismic moment in dyne-

cm. Hanks and Kanamori (1979) developed a magnitude scale in order to estimate radiated seismic energy and to avoid the saturation problems associated with other magnitudes. The moment magnitude M_w is related to M_0 by the definition

$$M_w = \frac{2}{3} \log_{10} M_0 - 10.7. \quad (1.7)$$

Since the observed *Lg* wave is an ensemble of many ray paths through the crust, its characteristics may be modeled by considering the statistics of random noise representing ground motion filtered by a seismograph. Cartwright and Longuet-Higgins (1956) studied the statistical distribution of the extrema of a function, applying the results to ocean waves. Iyengar and Iyengar (1969) modeled strong-motion accelerograms by multiplying a stationary process by a deterministic function and noted that certain characteristics, such as frequency of zero crossings, could be quantitatively found. Vanmarcke and Lai (1980) used random vibration theory to derive a relationship between the maximum acceleration and the root-mean-square acceleration, observing that random vibration theory is applicable to earthquake studies because strong ground motion can be modeled as a finite-duration, stationary, stochastic process. By examining acceleration time series, Hanks and McGuire (1981) confirmed that strong ground motion can be modeled as a finite-duration, stationary, stochastic process in the S-wave arrival window; they further developed a relationship between the root-mean-square acceleration and the spectral corner frequency of acceleration. Boore (1983, 2003) extended Cartwright and Longuet-Higgins's work to peak earthquake ground motions by incorporating seismic source and propagation and site effects. Boore (1983, 2003) showed that random vibration theory could be used to quickly estimate peak

ground motion parameters consistent with more time consuming spectrally shaped white noise simulations. By predicting peak motions based on the moments of the frequency spectrum, random vibration theory is a convenient tool that closely matches characteristics from simulations (Boore 1983, 2003). Using synthetic seismograms, Herrmann (1985) demonstrated that, as epicentral distance increases, the signal duration of an earthquake also increases because of wave propagation effects; he suggested the following formula for signal duration:

$$T = \frac{1}{f_c} + .05r \quad (1.8)$$

where T is the signal duration in s, f_c is the corner frequency of the far-field S-wave displacement spectra in Hz, and r is the epicentral distance in km.

In addition to random vibration theory, Boore (1983, 2003) used a stochastic method for time-domain simulations. He windowed and normalized white noise, multiplied the spectrum of the noise by a source spectrum, and transformed the resulting spectrum back to the time domain.

Assuming similarity between small and large earthquakes, Aki (1967) used an ω -squared dislocation model in order to compare earthquakes having the same propagational paths but different surface wave magnitudes M_s ; he determined that the corner frequencies for the various magnitudes lie on a straight line on a logarithmic plot. Brune (1970, 1971) developed a spectral model for S-waves that gives relations among source duration, spectral corner frequency, seismic moment, source duration, and stress drop. Frankel (1996) used this source spectrum model to estimate peak motions for the national probabilistic seismic hazard maps. Using a stochastic model and a

source model with two corner frequencies, Atkinson and Boore (1995) developed ground-motion relations for eastern North America for various distances and frequencies.

CHAPTER 2: Method 1 Calculation of m_{bLg} and $m_{Lg}(f)$

2.1 Empirical Dataset

The initial dataset is comprised of 42 United States earthquakes from the years 2010 and 2011 with $3.01 \leq M_w \leq 5.65$, with M_w determined at Saint Louis University from regional moment tensor inversion (Herrmann *et al.*, 2011). The majority of earthquakes occurred in Oklahoma and Arkansas. The Virginia $M_w = 5.65$ on August 23, 2011, and the Oklahoma $M_w = 5.59$ on June 6, 2011, both included in the dataset, are the largest recorded in the eastern United States. The number of m_{Lg} magnitude estimates per earthquake varies from 4 to 661 for the earthquakes in the dataset.

After an initial check on the signal-to-noise ratio for all earthquakes, 4 earthquakes were excluded as having an insufficient number of acceptable observations with which to calculate the appropriate magnitudes. Thus, 38 earthquakes met the threshold criteria in order to calculate m_{bLg} and $m_{Lg}(f)$ (Figure 2.1). For 19 of the 38 earthquakes, the USGS published m_{Lg} magnitudes, which are used to compare with those determined with our dataset.

2.2 Method 1 Calculation of m_{bLg} for Central and Eastern US Earthquakes

The goal of Method 1 is to replicate NEIC's methodology in the calculation of its m_{bLg} . The following procedure describes the magnitude-calculation steps for each earthquake from its associated stations. To begin Method 1, ground velocity from each station, derived by deconvolving the original instrument response, is convolved with the

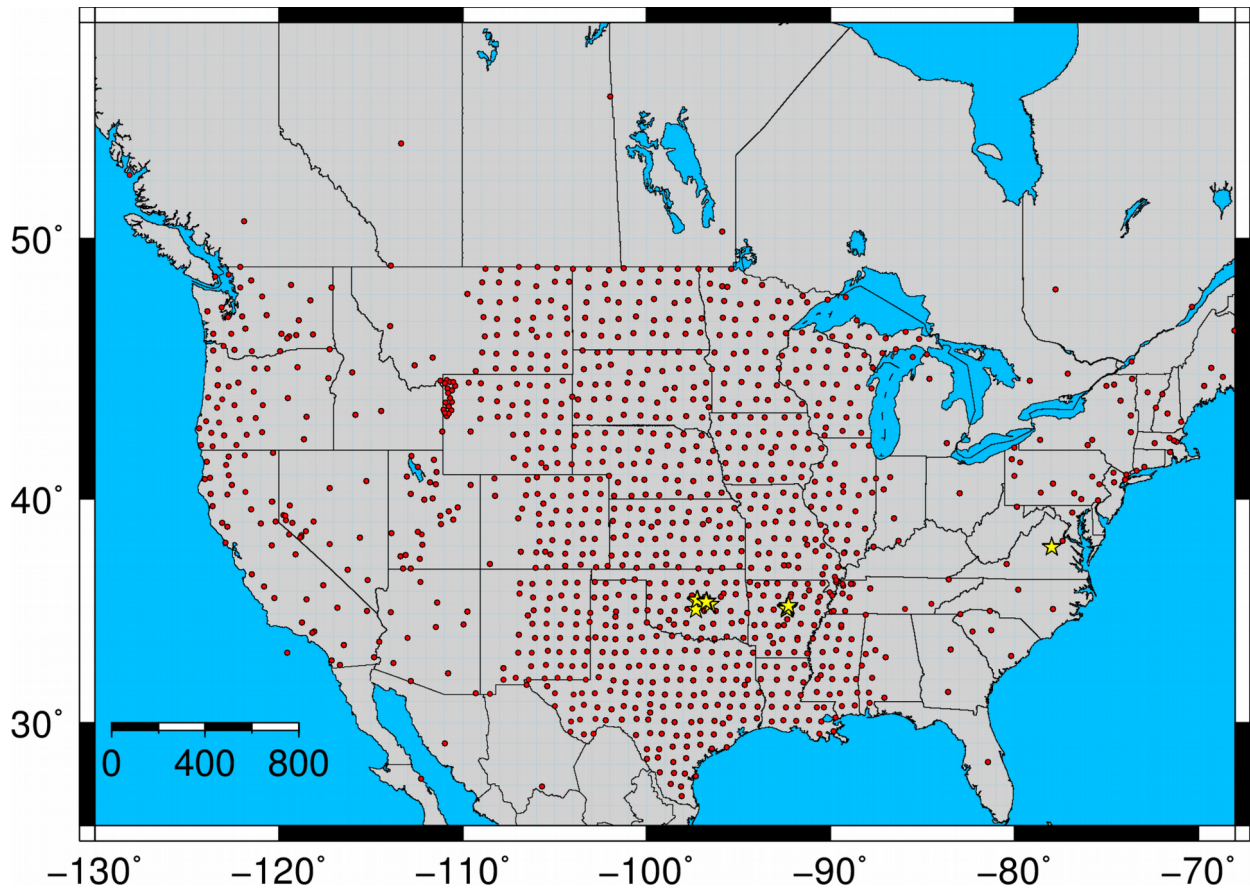


Figure 2.1. A map of the locations of the epicenters (yellow stars) of the 38 earthquakes for which magnitudes were calculated. The stations (red dots) include every station that recorded motion from any of the earthquakes. The Method 1 calculation of magnitudes eliminated many seismograms, and thus only a subset of stations was used for any given earthquake.

velocity response of the WWSSN short-period instrument in order to form the seismogram. Table 2.1 lists the parameters of the WWSSN short-period velocity response, and Figure 2.2 plots the velocity response.

For each waveform, a signal-to-noise test eliminates those stations with insufficiently distinguishable signals. Frequencies between 0.12 and 0.25 Hz are rejected in order to eliminate microseisms that would affect our procedure for determining the Lg amplitudes. The last 100 seconds of the seismogram are cut and labeled as noise. The part of the seismogram in the group velocity window between 3.2 and 3.6 km/s is labeled as signal. The positive peak amplitudes for both the noise and the signal are found. A trace is rejected if the peak signal amplitude is less than 3 times the peak noise amplitude.

Next, the absolute value of the seismogram is taken to yield a rectified trace, from which all peaks are found. Because the computation of m_{bLg} requires half the instrument-corrected peak-to-peak ground displacement, all peak-to-peak amplitudes are found by adding adjacent peaks of the rectified trace. The period is inferred as twice the time between rectified peaks used, and the frequency is the inverse of the period. Given a tabulation of peak-to-peak amplitudes, the third-largest is identified.

If the frequency of the third-largest peak-to-peak amplitude is between 0.77 and 1.43 Hz, the gain at that frequency is obtained from the WWSSN short-period displacement response; otherwise, the seismogram is rejected from further processing. Table 2.2 gives the parameters for the WWSSN short-period displacement response, and Figure 2.3 plots the response. For those seismograms containing third-largest

Table 2.1. The table lists the parameters for the WWSSN short-period velocity response.

CONSTANT	532.1425
ZEROS	
0.000	0.000
0.000	0.000
POLES	
-3.725	6.220
-3.725	-6.220
-5.612	0.000
-13.240	0.000
-21.080	0.000

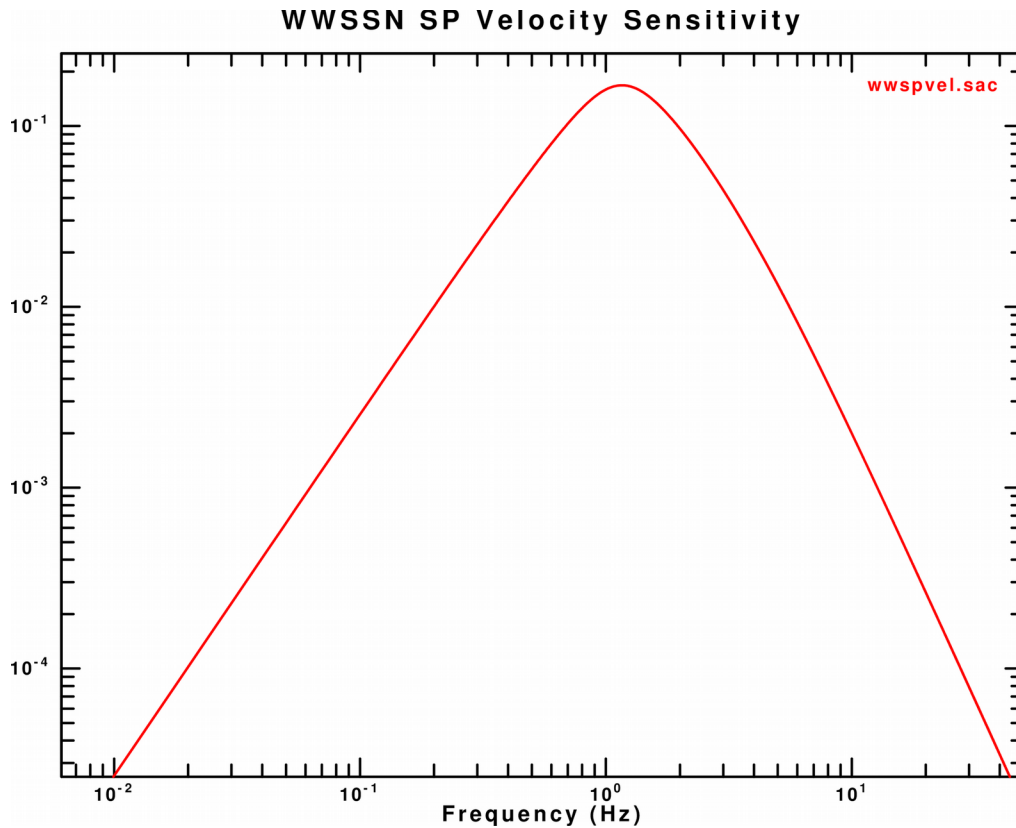


Figure 2.2. The velocity response of the WWSSN short-period instrument.

Table 2.2. The table lists the parameters for the WWSSN short-period displacement response.

CONSTANT	532.1425
ZEROS	
0.000	0.000
0.000	0.000
0.000	0.000
POLES	
-3.725	6.220
-3.725	-6.220
-5.612	0.000
-13.240	0.000
-21.080	0.000

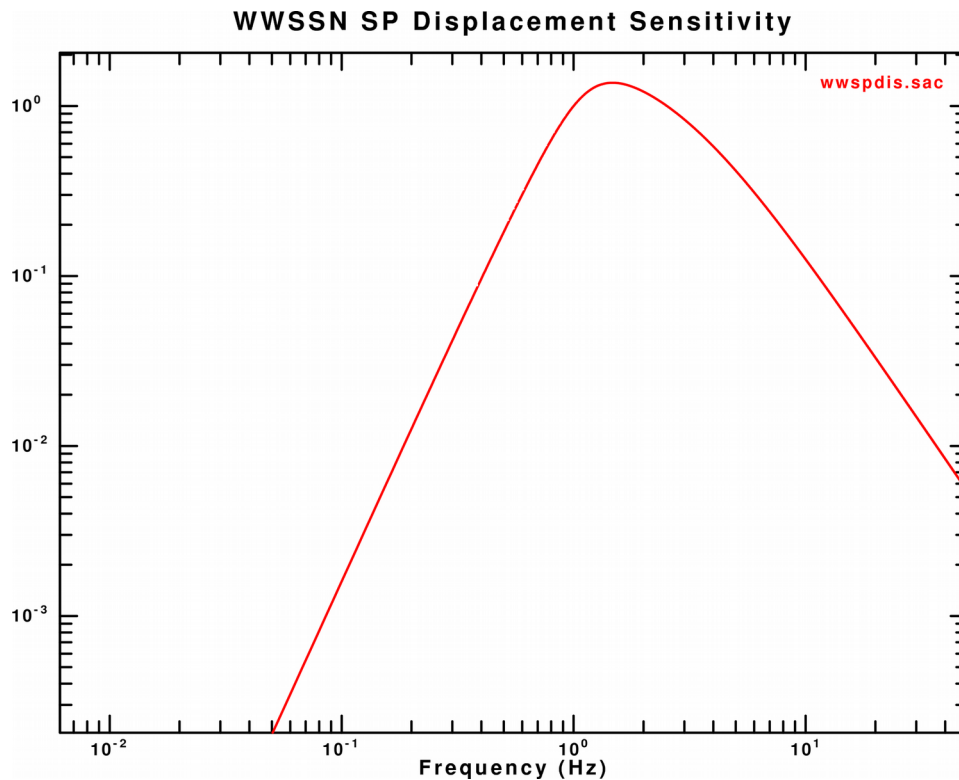


Figure 2.3. The displacement response of the WWSSN short-period instrument. The constant was adjusted so that the gain at 1 Hz is 1. Note that the displacement response $D(f) = (i2\pi f)V(f)$ where $V(f)$ is the complex velocity response for the instrument.

peak-to-peak amplitudes in the appropriate frequency range, half the third-largest peak-to-peak amplitude is divided by the displacement gain at that frequency in order to compute the instrument-corrected ground displacement A in μm . The m_{bLg} is then calculated for each station from the definition used by the NEIC

$$m_{\text{bLg}} = 2.96 + 0.8333 \log_{10} \left(\frac{r}{10} \right) + .4343 \gamma r + \log_{10} A \quad \text{for } 50 \text{ km} \leq r \leq 1200 \text{ km} \quad (2.1)$$

where γ is set at 0.00063 km^{-1} . A 25% trimmed mean is employed in order to determine a single magnitude for an earthquake. In the 25% trimmed mean method, magnitude estimates are sorted in increasing order, and the top 25% and the bottom 25% of values are cut. The remaining values each have equal weighting in the average. See Figure 2.4 for a flowchart of the procedure for Method 1.

2.3 Method 1 Calculation of $m_{\text{Lg}}(f)$

The procedure for calculating $m_{\text{Lg}}(f)$ using Method 1 is the same as the procedure for calculating m_{bLg} using Method 1 except for one difference: the frequency f is used to derive the coefficient of anelastic attenuation γ . The following formula is used for γ , as determined appropriate for the central United States by Herrmann and Kijko (1983a),

$$\gamma = 0.001 f^{0.7}. \quad (2.2)$$

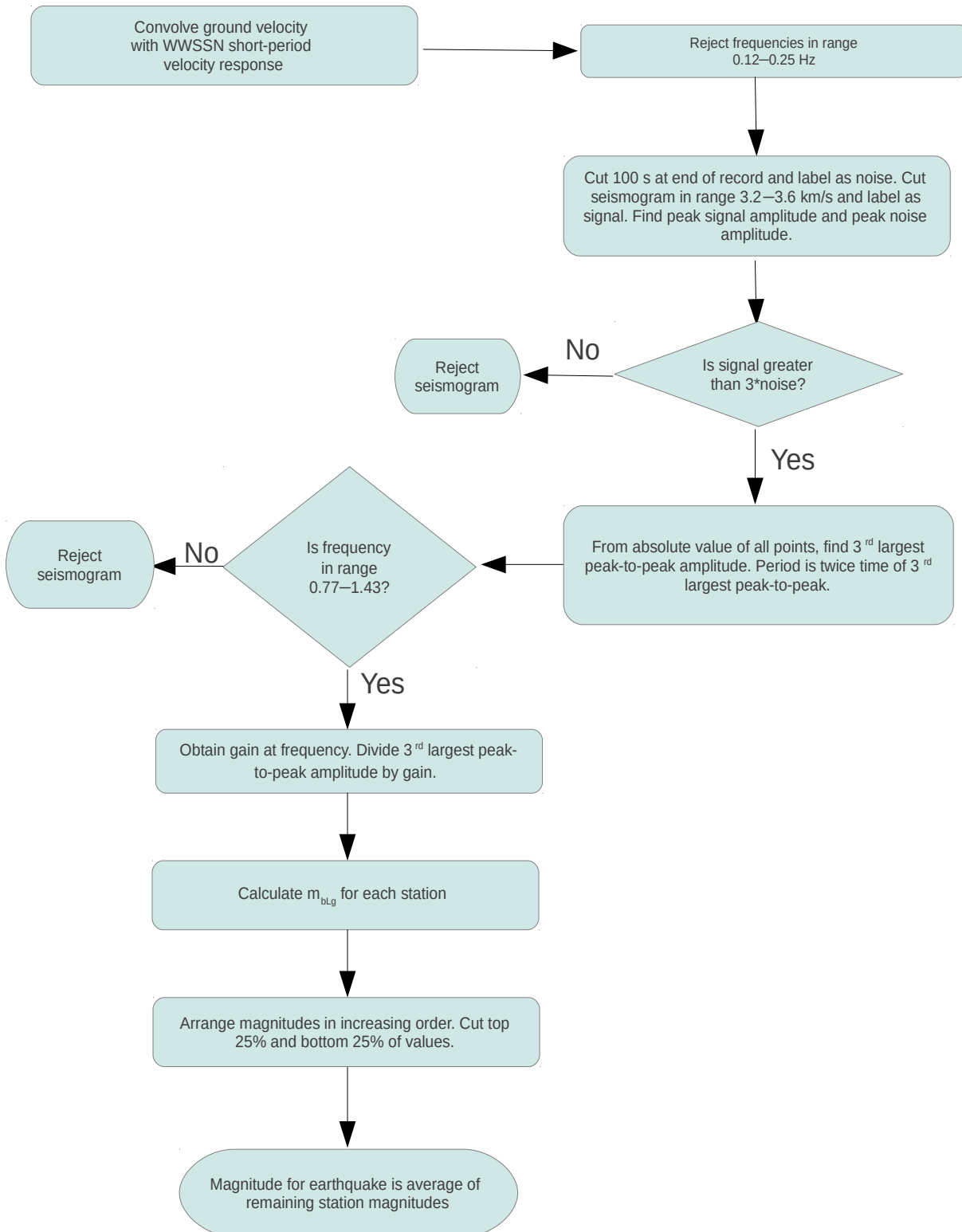


Figure 2.4. Flowchart for Method 1 calculation of m_{bLg} .

2.4 Method 1 m_{bLg} Results and Discussion

Figure 2.5 compares the M_w (SLU) versus Method 1 m_{bLg} . The linear regression estimate of M_w (SLU) for a given Method 1 m_{bLg} is

$$M_w = 0.60 + 0.81m_{bLg}. \quad (2.3)$$

The slope error is 0.047, which is about 6% of the estimated slope from Equation (2.3), and the intercept error is 0.189, which is about 32% of the estimated intercept from Equation (2.3). The sample variance is 0.012, implying low variability and a relatively good fit for the linear estimate. The coefficient of determination r^2 is 0.97, indicating that 97% of the variation in the predicted M_w (SLU) is explained by a linear relationship between Method 1 m_{bLg} and M_w (SLU). The red line in Figure 2.5 is the regression equation. The inner blue lines represent the 95% confidence interval on the regression line, and the outer blue lines represent the 95% prediction interval for new observations.

Although Equation (2.3) seems to closely fit the data, one caution in solely using Equation (2.3) for a Method 1 m_{bLg} above 5 is the lack of data for larger values of m_{bLg} . As described in Chapter 4, modeling suggests that the relationship between Method 1 m_{bLg} and M_w (SLU) is not linear. Thus, using Method 1 m_{bLg} to predict M_w (SLU) for m_{bLg} greater than 5.3 is unlikely to produce an accurate prediction for M_w (SLU).

For Method 1 m_{bLg} between 3 and 5.3, though, Equation (2.3) produces useful results. The tight clustering of data points in the range Method 1 m_{bLg} 3.2–3.8 causes the 95% confidence interval on the regression line to be the narrowest between those limits. Thus, especially in the reduced range, Equation (2.3) can be a valuable and valid predictor of M_w (SLU) from m_{bLg} .

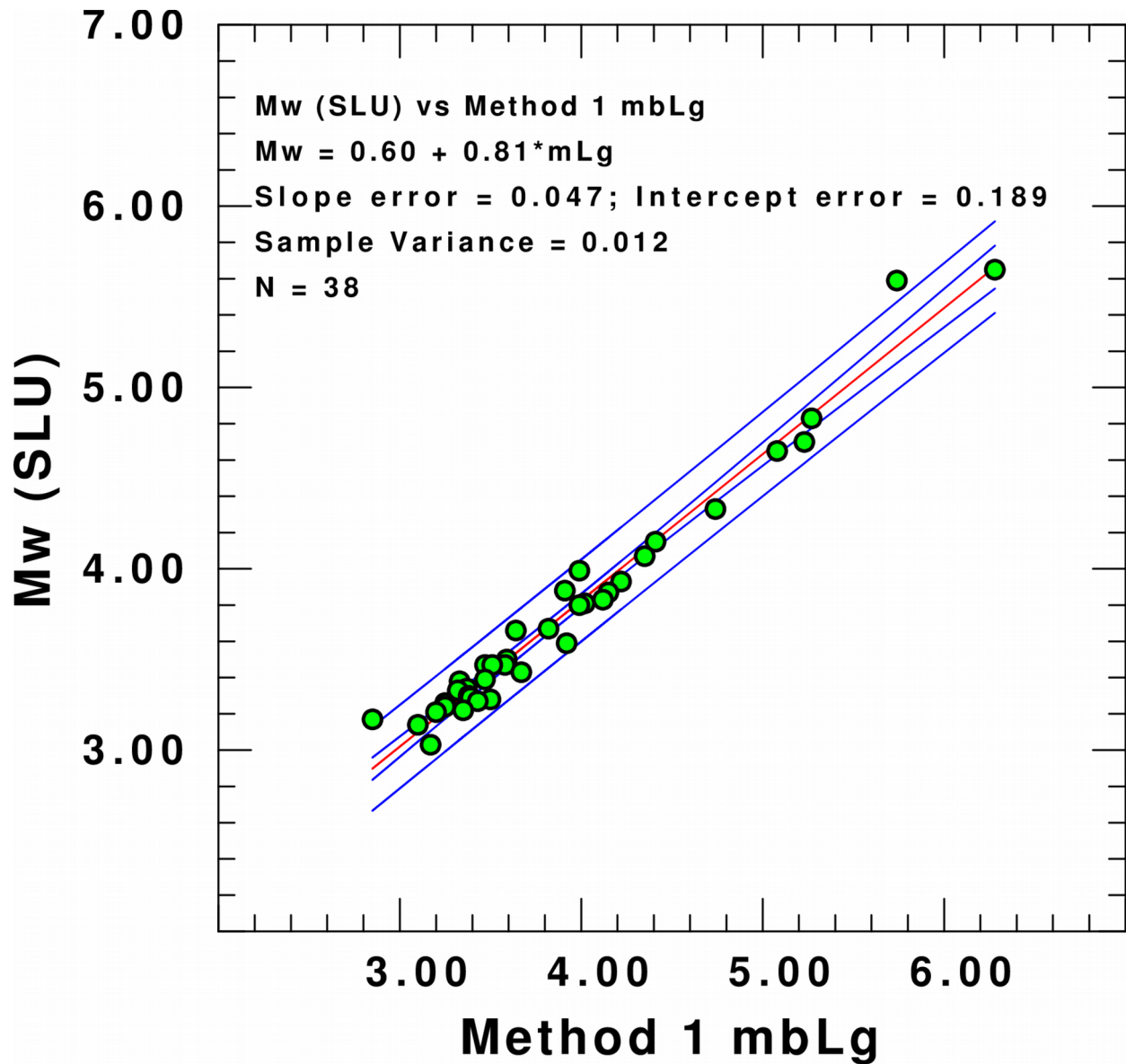


Figure 2.5. Regression analysis for Method 1 m_{bLg} . The red line is the regression line, the inner blue lines are the confidence intervals, and the outer blue lines are the prediction intervals.

Figure 2.6 compares the regression analysis of Method 1 m_{bLG} to the regression analysis for the published USGS m_{bLG} . The linear regression estimate of M_w (SLU) for a given NEIC m_{bLG} is

$$M_w = 0.39 + 0.85m_{bLG}. \quad (2.4)$$

The slope error is 0.076, which is about 9% of the estimated slope from Equation (2.4), and the intercept error is 0.324, which is about 83% of the estimated intercept from Equation (2.4). The sample variance is 0.017, which is not practically different than the Method 1 sample variance 0.012. The coefficient of determination r^2 is 0.97, indicating that 97% of the variation in the predicted M_w (SLU) is explained by a linear relationship between the USGS m_{bLG} and M_w (SLU). The red line in Figure 2.6 is the regression equation. The inner blue lines represent the 95% confidence interval on the regression line, and the outer blue lines represent the 95% prediction interval for new data.

Although Equations (2.3) and (2.4) both have $r^2 = 0.97$, there are three primary reasons that Equation (2.3) may be more appropriate than Equation (2.4) and, thus, to prefer Equation (2.3) over Equation (2.4). First, the regression analysis of Method 1 m_{bLG} has twice the data points of the NEIC dataset, while at the same time containing all the earthquakes in the NEIC dataset. Second, nearly all of the additional earthquake magnitudes in the Method 1 dataset and not in the NEIC dataset are less than $m_{bLG} = 4.5$, giving a narrower 95% confidence interval and a 95% prediction interval. Finally, the errors in the slope and particularly the intercept for the Method 1 m_{bLG} regression are much smaller

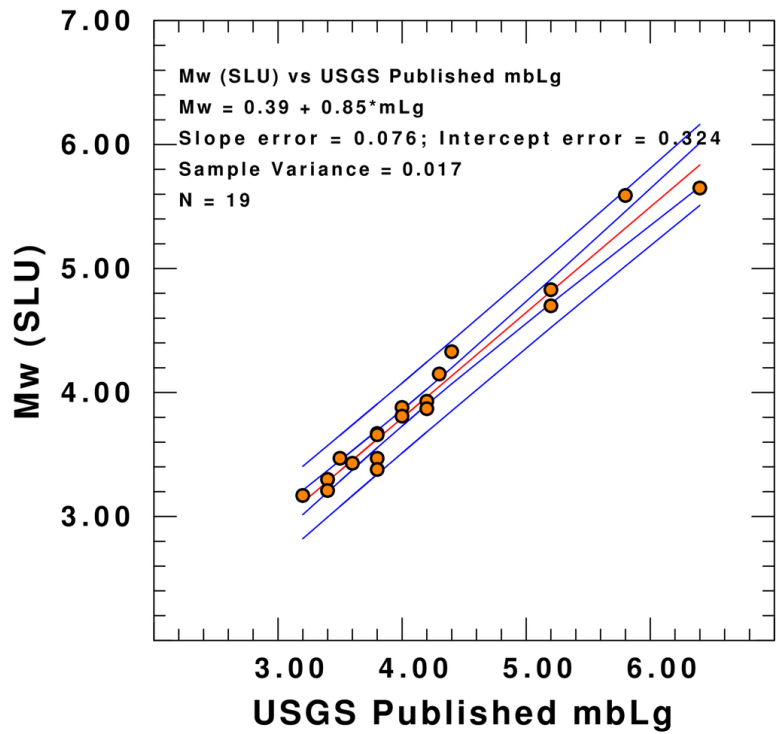
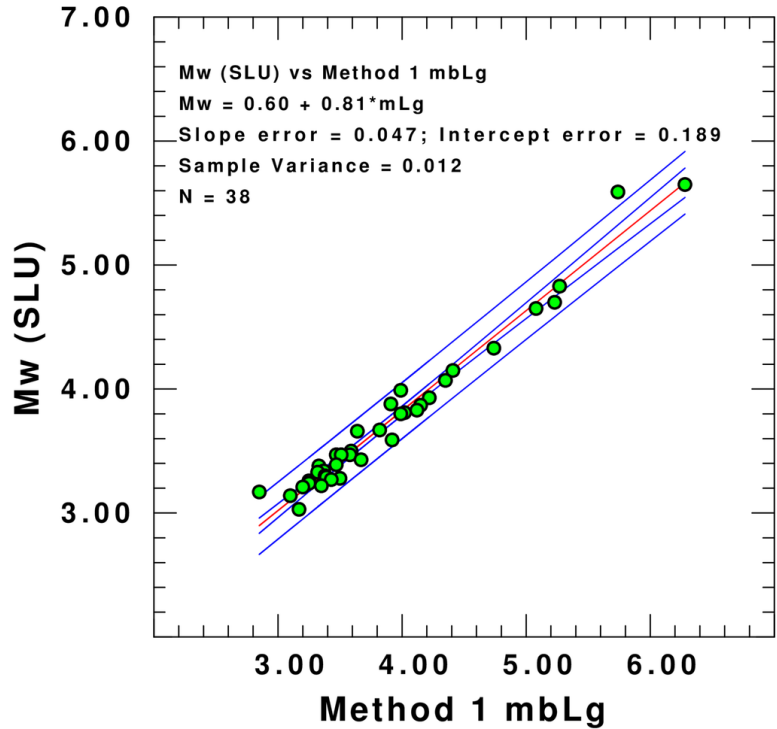


Figure 2.6. A comparison of the regression analyses for Method 1 m_{bLg} and the published data for the NEIC m_{bLg} .

than in the regression for the NEIC m_{bLg} .

The conclusion, then, is that Equation (2.3) is an accurate predictor of M_w (SLU) for a frequency-independent γ , even if, as subsequent sections show, a constant-valued γ is not strictly correct.

2.5 Method 1 $m_{Lg}(f)$ Results and Discussion

Figure 2.7 compares the M_w (SLU) versus Method 1 $m_{Lg}(f)$. The linear regression estimate of M_w (SLU) for a given Method 1 $m_{Lg}(f)$ is

$$M_w = 0.68 + 0.78m_{Lg}(f). \quad (2.5)$$

The slope error is 0.051, which is about 7% of the estimated slope from Equation (2.5), and the intercept error is 0.205, which is about 30% of the estimated intercept from Equation (2.5). The sample variance is 0.015, not practically different than Equations (2.3) and (2.4). The coefficient of determination r^2 is 0.96, indicating that 96% of the variation in the predicted M_w (SLU) is explained by a linear relationship between Method 1 $m_{Lg}(f)$ and M_w (SLU). The red line in Figure 2.7 is the regression equation. The inner blue lines represent the 95% confidence interval on the regression line, and the outer blue lines represent the 95% prediction interval for new data. The Method 1 m_{bLg} caveat about larger m_{bLg} also applies to the Method 1 $m_{Lg}(f)$.

Figure 2.8 compares the regression analysis of Method 1 $m_{Lg}(f)$ against the regression analysis for the published NEIC m_{bLg} . Even though Equations (2.4) and (2.5) are similar and have comparable coefficients of correlation, Method 1 $m_{Lg}(f)$ would be preferable to the NEIC m_{bLg} if the actual γ is frequency dependent.

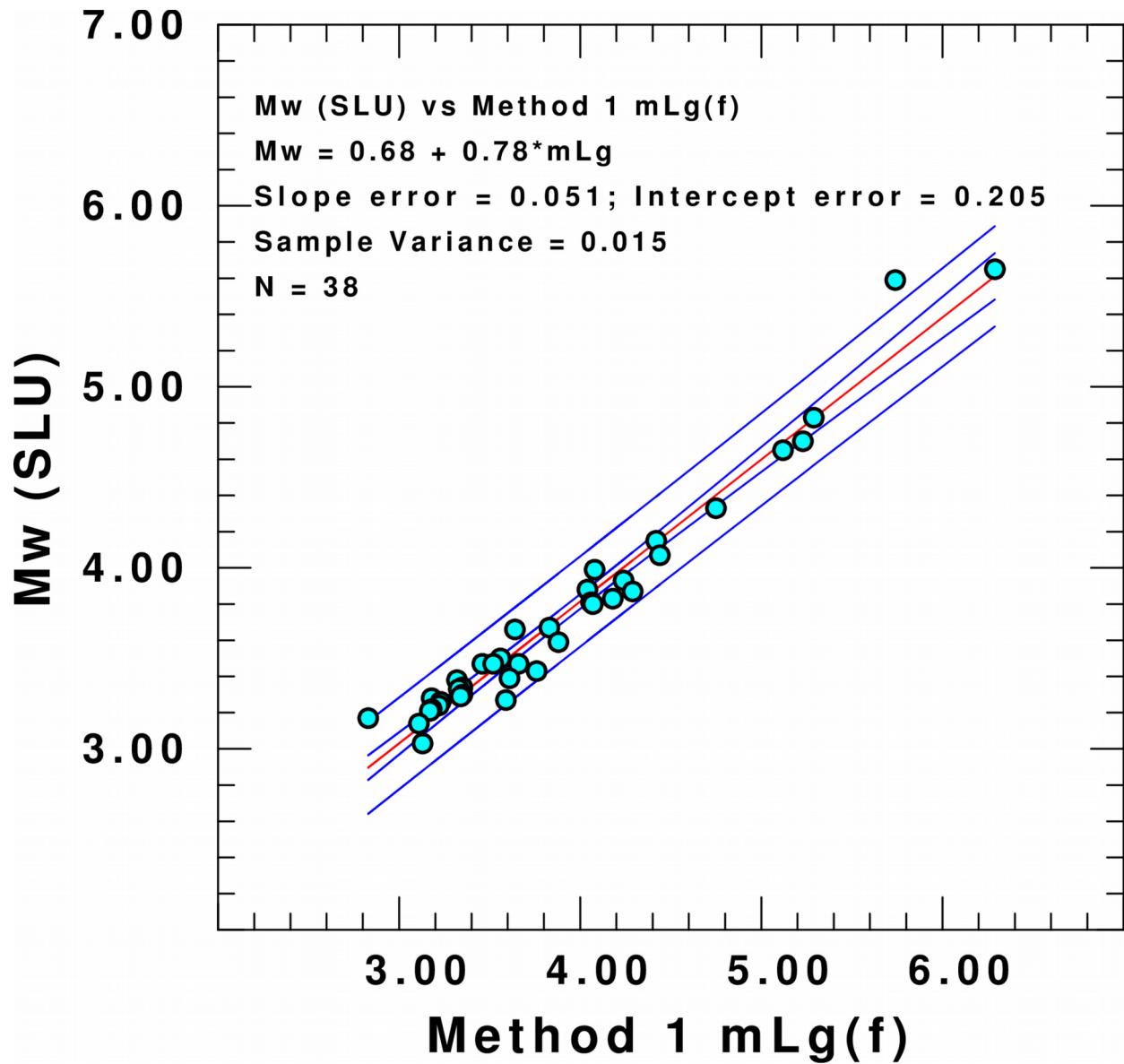


Figure 2.7. Regression analysis for Method 1 $mLg(f)$. The red line is the regression line, the inner blue lines are the confidence intervals, and the outer blue lines are the prediction intervals.

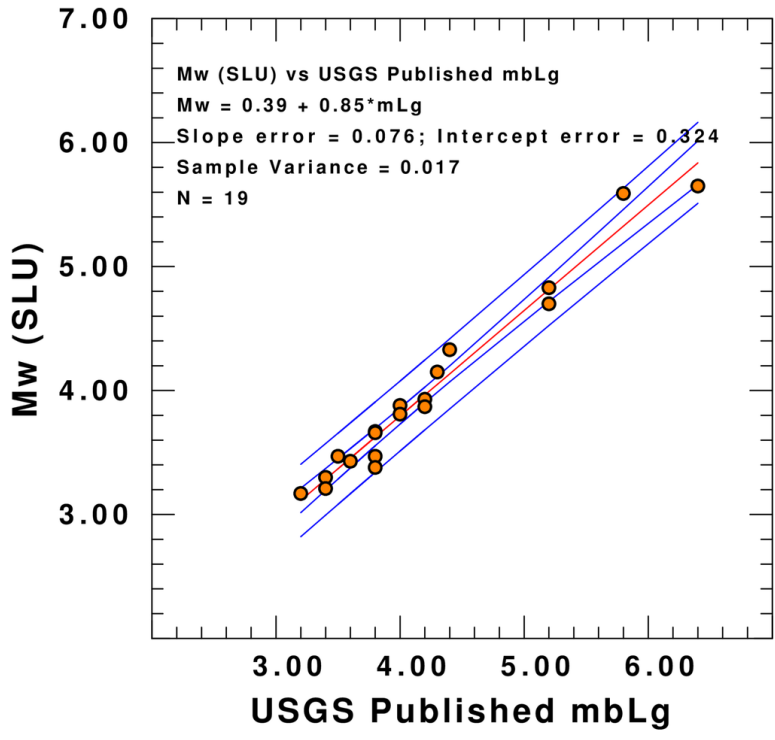
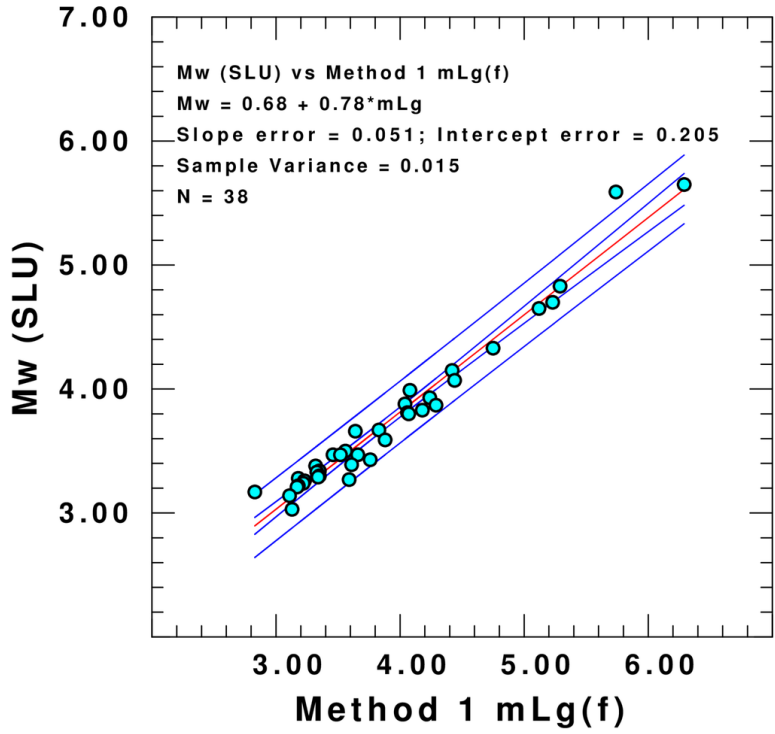


Figure 2.8. A comparison of the regression analyses for Method 1 $m_{Lg}(f)$ and the published data for the NEIC m_{bLg} .

Equations (2.3), (2.4), and (2.5) give M_w (SLU) predictions within a few tenths of a magnitude unit of one another, and all three equations have validity. Among the three equations, though, Equation (2.5) is still preferable because the frequency-dependent γ incorporates some physics of the wave propagation. Future work may adjust the $m_{Lg}(f)$ formula in order to have γ contribute substantially more to the final magnitude calculation.

2.6 Comparisons of Method 1 m_{bLg} , Method 1 $m_{Lg}(f)$, and published m_{bLg}

Figure 2.9 compares the Method 1 m_{bLg} versus the published NEIC m_{bLg} for the 19 common events. The line indicates a 1-to-1 relationship if the Method 1 m_{bLg} were equal to the published NEIC m_{bLg} . The goal of Figure 2.9 is to determine whether the Method 1 m_{bLg} methodology replicates the NEIC m_{bLg} methodology. For the most part, the Method 1 m_{bLg} methodology actually replicates the NEIC m_{bLg} methodology. For 16 of the 19 common events, the calculated Method 1 m_{bLg} and the NEIC m_{bLg} are similar, and the remaining three events are within 0.5 magnitude units of one another. One important difference in the calculation of Method 1 m_{bLg} compared to the NEIC m_{bLg} is the number of stations used in the magnitude calculation: for most events, Method 1 has more stations in its magnitude calculation than the NEIC calculation.

Figure 2.10 compares the Method 1 $m_{Lg}(f)$ versus the published NEIC m_{bLg} for the 19 common events. The reference line shows a 1-to-1 relationship. Figures 2.10 is virtually the same as Figure 2.9. One implication is that γ does not substantially affect the final magnitude computation for this dataset.

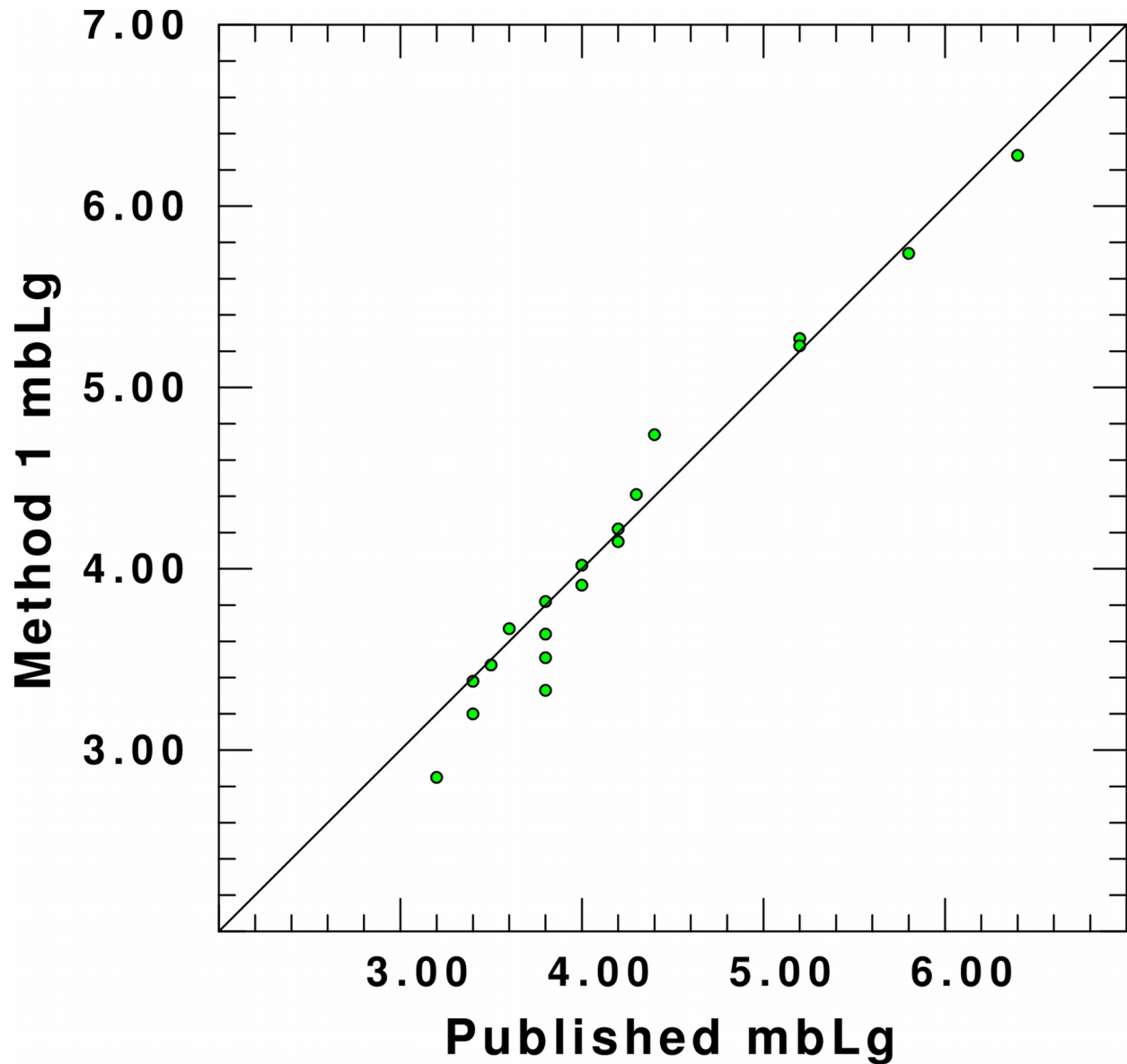


Figure 2.9. A plot of the Method 1 m_{bLg} versus the published NEIC m_{bLg} for the 19 earthquakes common to both groups. A 1-to-1 reference line is shown.

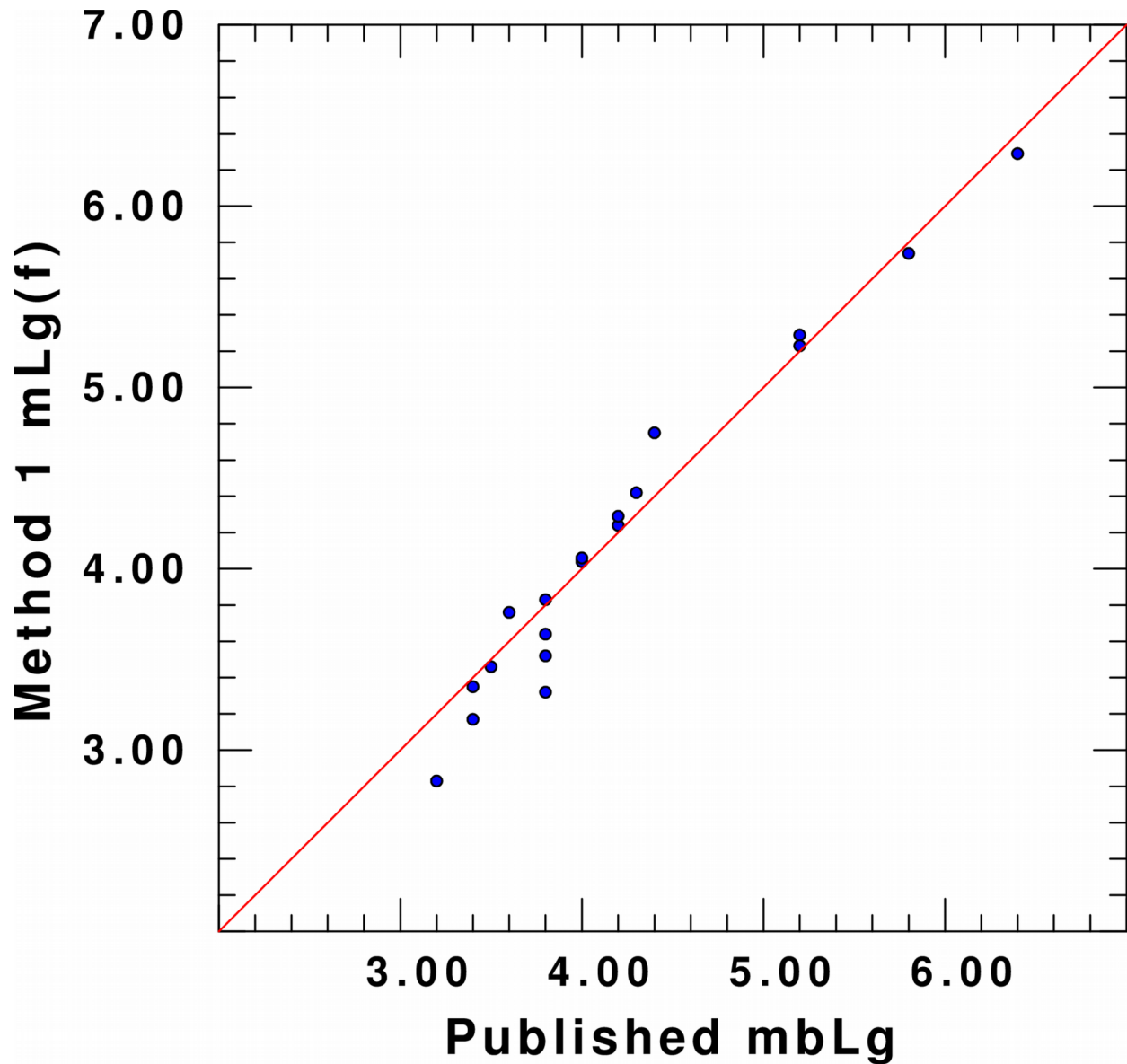


Figure 2.10. A plot of the Method 1 $m_{Lg}(f)$ versus the published NEIC m_{bLg} for the 19 earthquakes common to both groups. A 1-to-1 reference line is shown.

Figure 2.11 compares the Method 1 $m_{Lg}(f)$ versus the Method 1 m_{bLg} for all 38 earthquakes. The reference line shows a 1-to-1 relationship. It is seen that the Method 1 $m_{Lg}(f)$ is larger than the Method 1 m_{bLg} by 0.05 to 0.1 magnitude units for the same event and that there is a slight dependence on earthquake size. The offset in Figure 2.11 indicates that the Method 1 $m_{Lg}(f)$ is fundamentally different from the Method 1 m_{bLg} .

2.7 Adjustments to the Method 1 Lg magnitude relationships

Figure 2.12 shows an attempt to fit the M_w (SLU) as a function of m_{bLg} using a bilinear relationship. In fitting the data at smaller magnitudes, an expected slope of $2/3$, based on source-scaling relations, is used as a guide in selecting the magnitude range. The slope used for larger magnitudes is compatible with the data and not well constrained by the modeling of Chapter 4. The equations are

$$M_w = 1.10 + 0.67m_{bLg} \quad \text{for } 2.0 < m_{bLg} < 4.5 \quad (2.6)$$

$$M_w = -0.15 + 0.95m_{bLg} \quad \text{for } 4.5 < m_{bLg} < 7.0 \quad (2.7)$$

where the breakpoint $m_{bLg} = 4.5$ was chosen based on modeling (Chapter 4) and empirical iterations of a regression program.

Figure 2.13 shows an attempt to fit the M_w (SLU) as a function of $m_{Lg}(f)$ using a bilinear relationship. No expected slope or intercept is used as a guide for the regression equations; the data determine both. The equations are

$$M_w = 1.11 + 0.66m_{Lg}(f) \quad \text{for } 2.0 < m_{Lg}(f) < 4.5 \quad (2.8)$$

$$M_w = -0.20 + 0.95m_{Lg}(f) \quad \text{for } 4.5 < m_{Lg}(f) < 7.0 \quad (2.9)$$

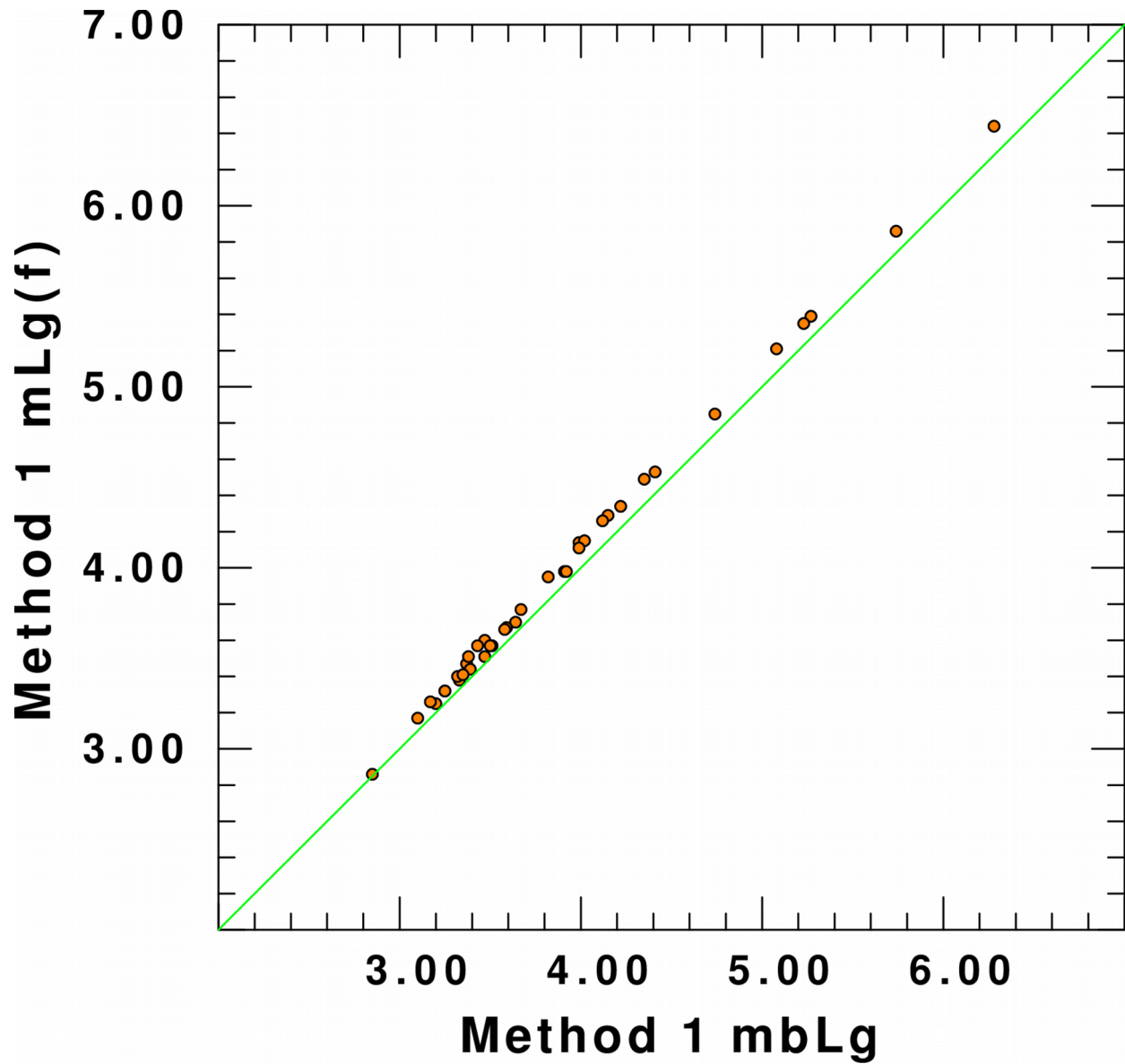


Figure 2.11. A plot of the Method 1 m_{bLg} versus the Method 1 $m_{Lg}(f)$ for all 38 earthquakes used in Method 1. A 1-to-1 reference line is shown.

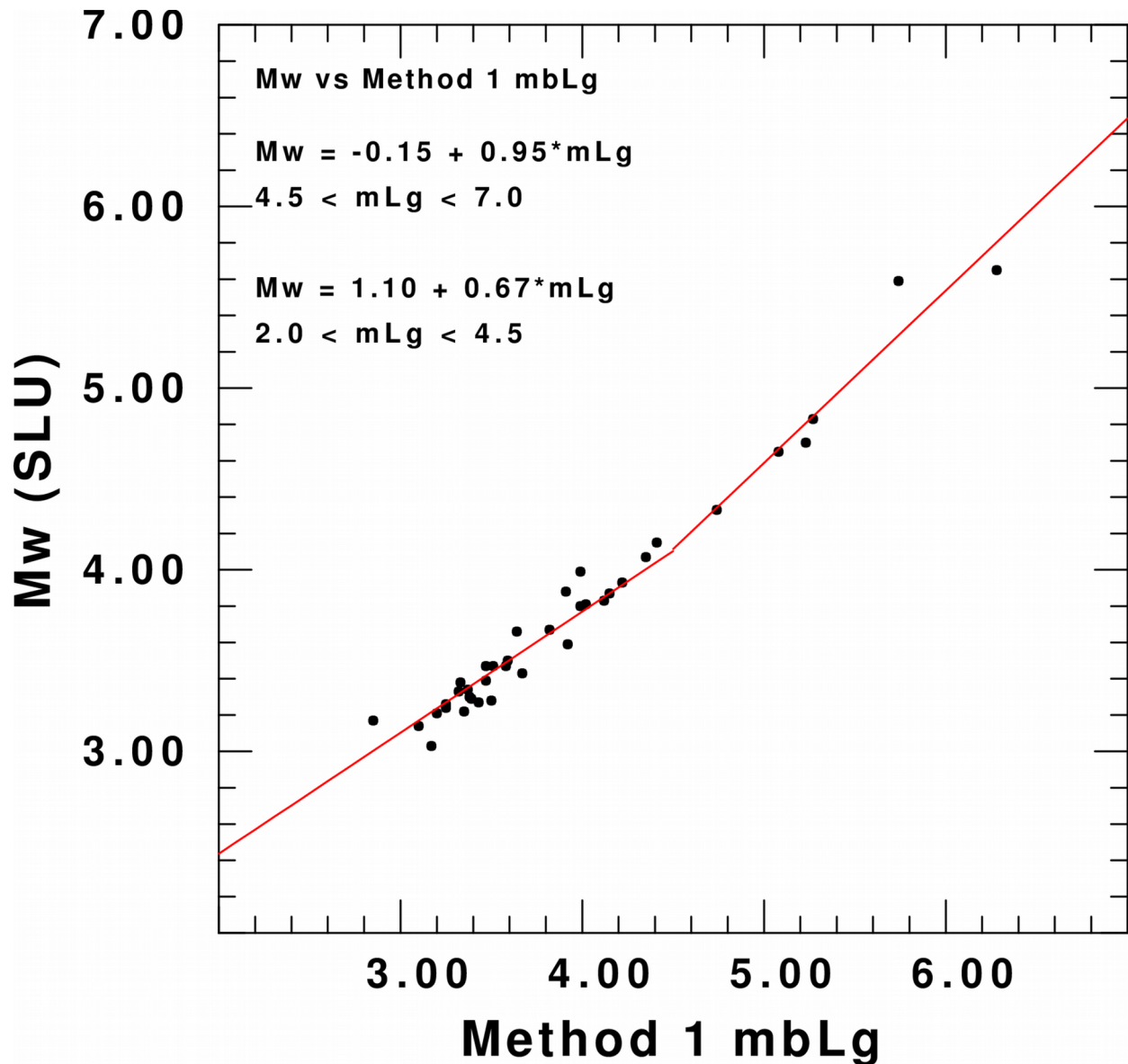


Figure 2.12. A regression graph of the M_w (SLU) versus the Method 1 m_{bLg} based on a bilinear division. Modeling, described in Chapter 4, and empirical iterations of a regression program suggest that the regression line slope change at around $m_{bLg} = 4.5$. For the regression line for smaller magnitudes, the slope is fixed at $2/3$. For the regression line for larger magnitudes, the slope is determined by the data.

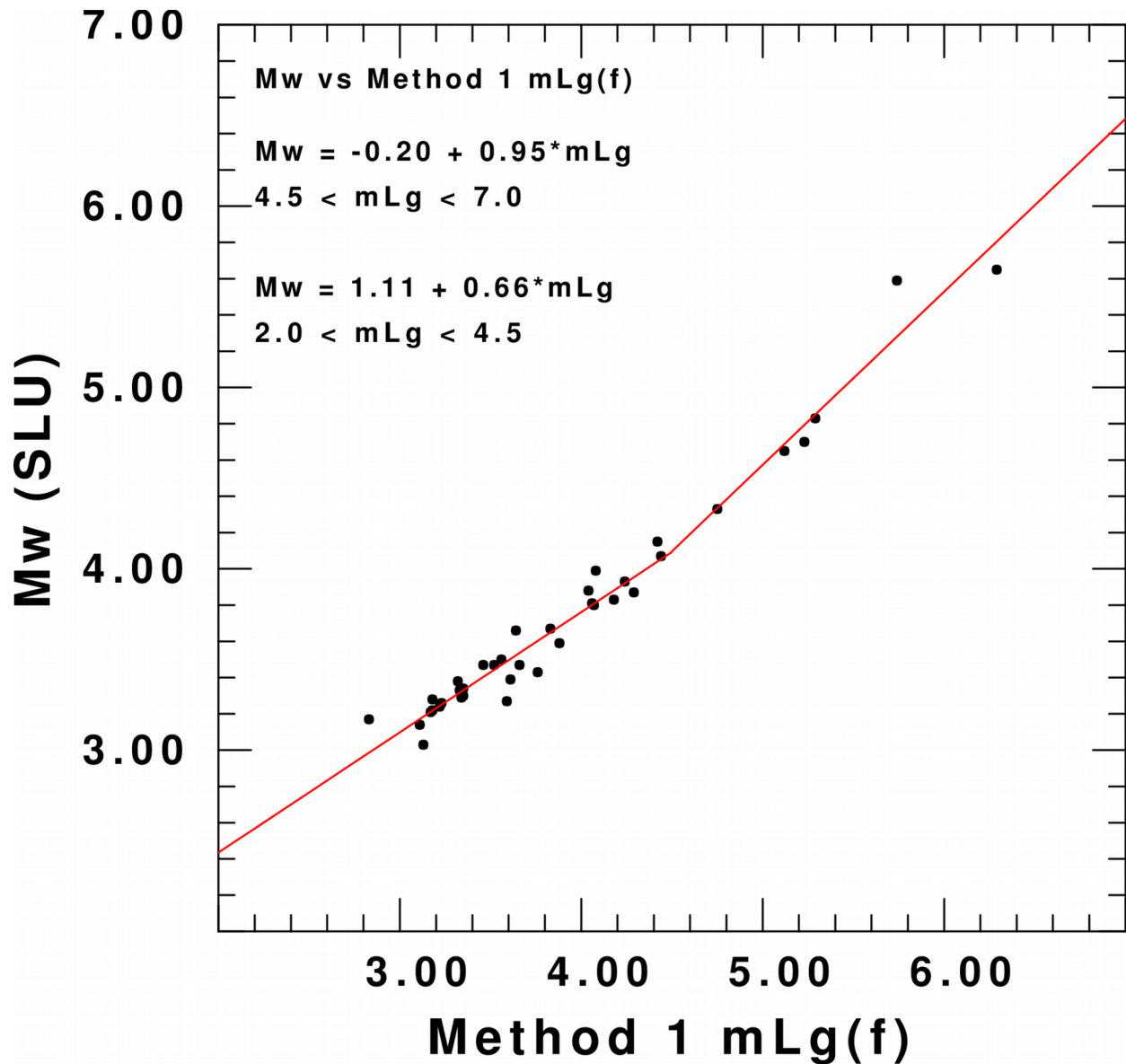


Figure 2.13. A regression graph of the the M_w (SLU) versus the Method 1 $m_{Lg}(f)$ based on a bilinear division. Modeling, described in Chapter 4, and empirical iterations of a regression program suggest that the regression line slope change at around $m_{Lg}(f) = 4.5$.

where the breakpoint $m_{Lg}(f) = 4.5$ was chosen based on modeling (Chapter 4) and empirical iterations of a regression program.

Figures 2.14 and 2.15 show the Method 1 m_{bLg} and $m_{Lg}(f)$, respectively, using half the maximum peak-to-peak amplitude rather than half the third-largest peak-to-peak amplitude. One reason for creating Figures 2.14 and 2.15 is that determining the maximum peak-to-peak amplitude is easier than determining the third-largest peak-to-peak amplitude. In addition, using the maximum peak-to-peak amplitude permits the use of random vibration theory in Chapter 4 to simulate the magnitude scaling with seismic moment and a direct comparison between the modeling relationships and Figures 2.14 and 2.15.

Because the Method 1 m_{bLg} and $m_{Lg}(f)$ using half the maximum peak-to-peak amplitude are equal to or greater than the Method 1 m_{bLg} and $m_{Lg}(f)$ using half the third-largest peak-to-peak amplitude, respectively, relating the corresponding magnitudes to one another is important. The equations are

$$(m_{bLg})_{max} = (m_{bLg})_{3^{rd}} + 0.11 \quad (2.10)$$

$$(m_{Lg}(f))_{max} = (m_{Lg}(f))_{3^{rd}} + 0.20 \quad (2.11)$$

where the constant offsets are averages of the residuals. We will use the offsets in the Chapter 4 modeling.

2.8 Residuals for Method 1 m_{bLg} and $m_{Lg}(f)$

Figure 2.16 plots the magnitude residuals as a function of distance from each individual earthquake for both Method 1 m_{bLg} and $m_{Lg}(f)$. The m_{bLg} residual plot is based

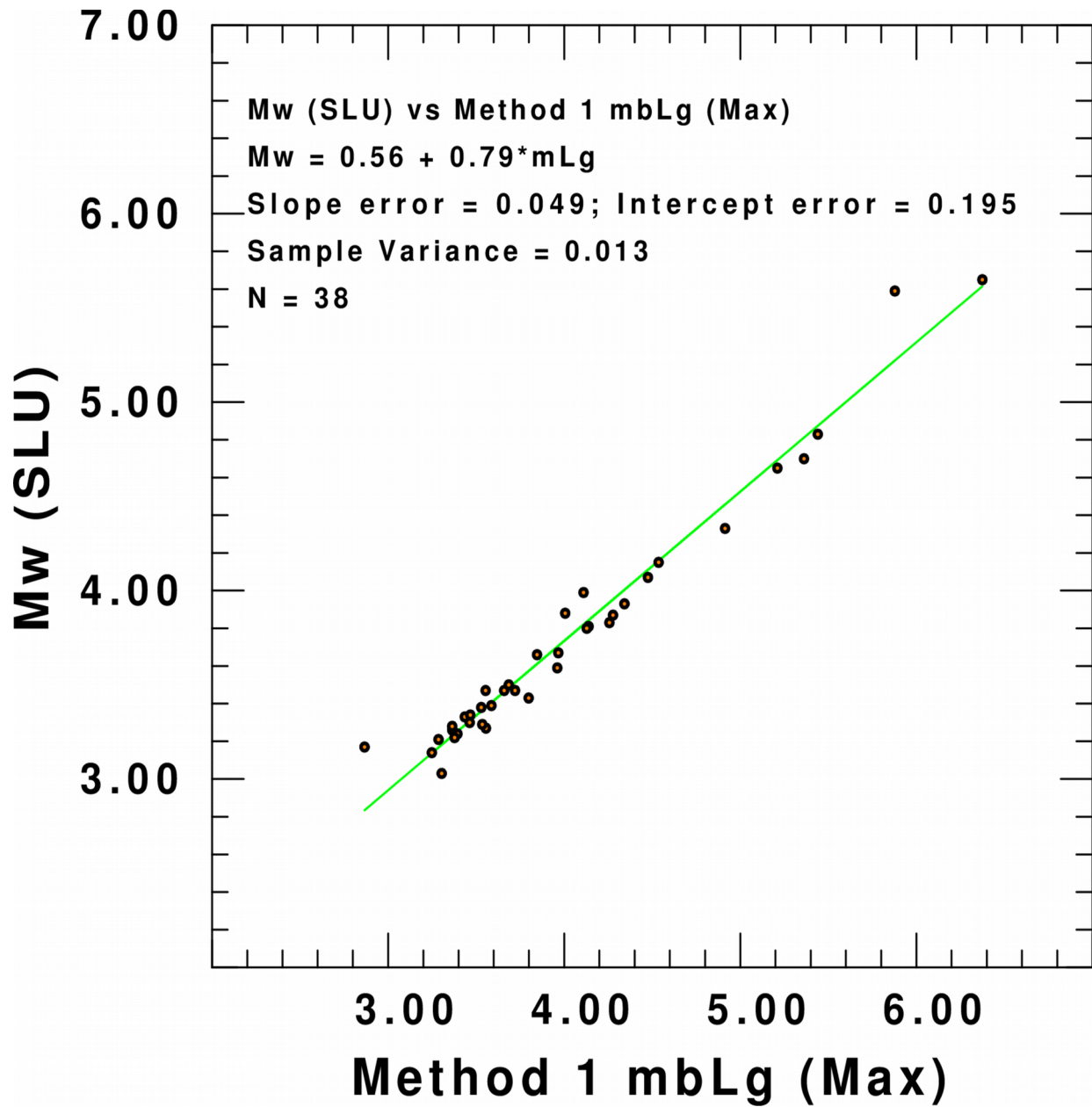


Figure 2.14. A regression analysis of Method 1 m_{bLg} in which the maximum peak-to-peak amplitude, rather than the third-largest peak-to-peak amplitude, is used in the calculation of m_{bLg} .

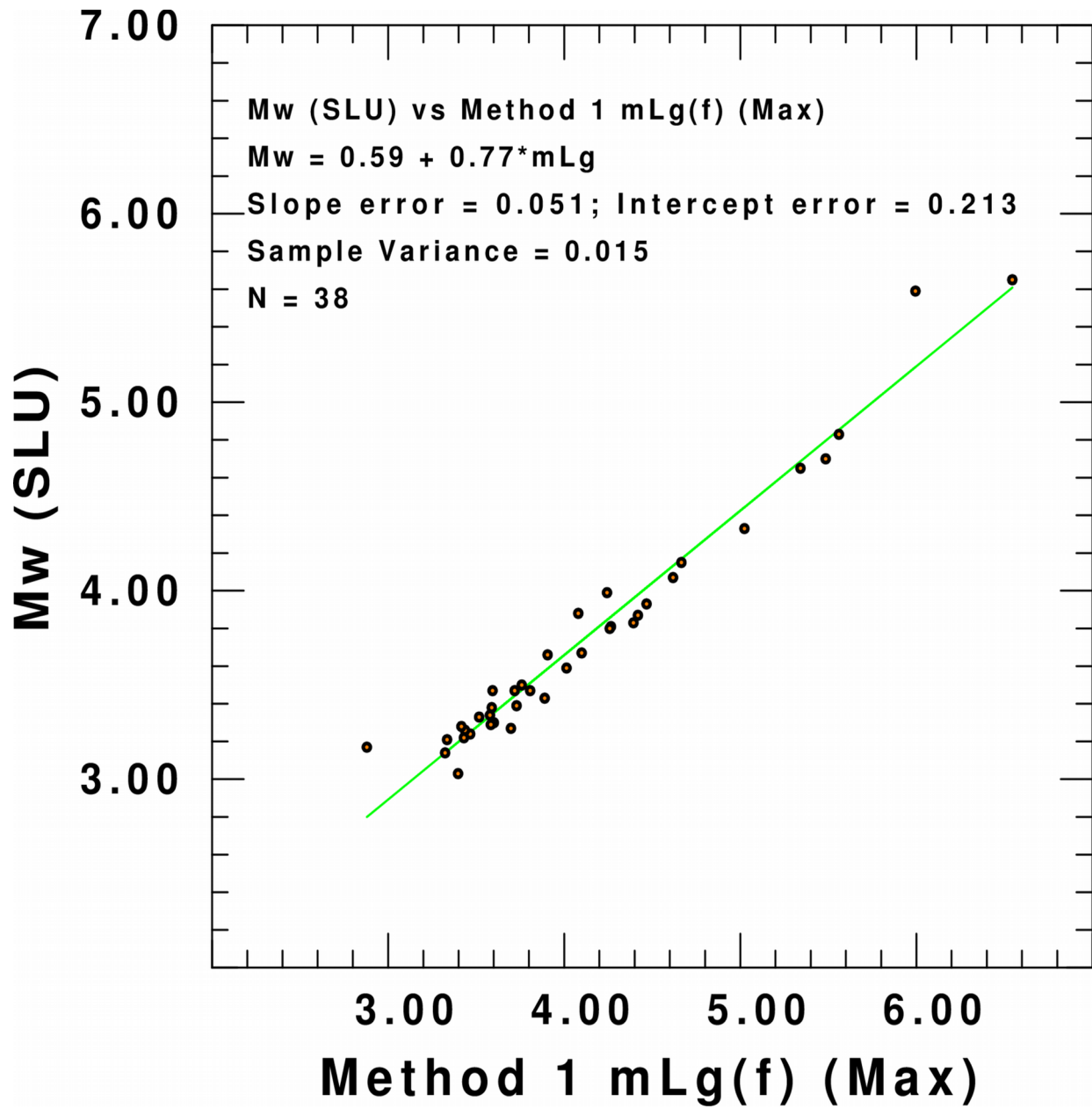


Figure 2.15. A regression analysis of Method 1 $m_{Lg}(f)$ in which the maximum peak-to-peak amplitude, rather than the third-largest peak-to-peak amplitude, is used in the calculation of $m_{Lg}(f)$.

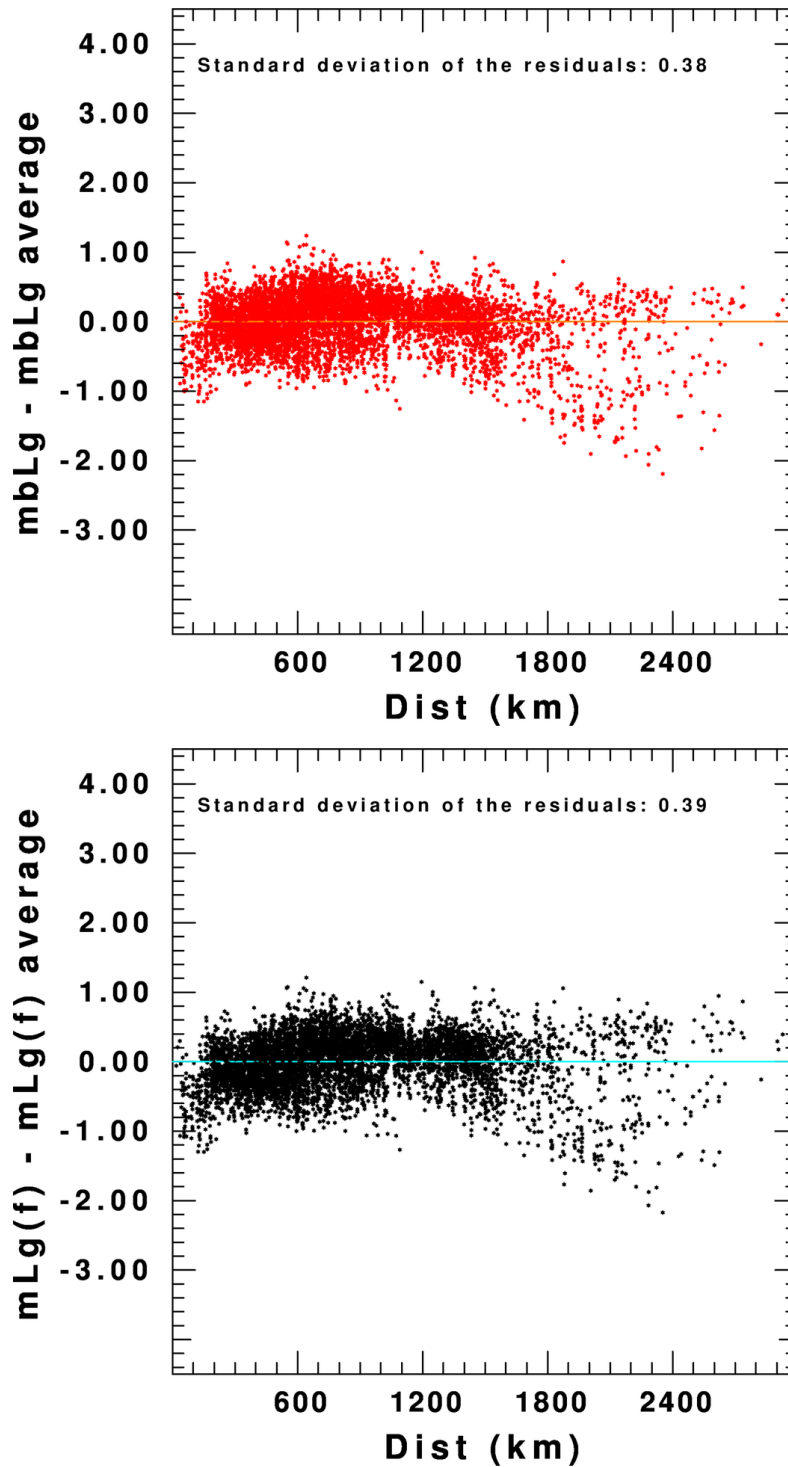


Figure 2.16. The Method 1 m_{bLg} residuals for each individual earthquake are overlaid (*top*), and the standard deviation of those residuals is given. The Method 1 $m_{Lg}(f)$ residuals for each individual earthquake are overlaid (*bottom*), and the the standard deviation of those residuals is given.

on γ fixed at 0.00063 km^{-1} , and the $m_{Lg}(f)$ plot is based on $\gamma = 0.001f^{0.7}$ for each station. The purposes of Figure 2.16 are to discern whether the magnitudes are empirically consistent within the magnitude's definition and to determine whether one magnitude is more reliable than the other. For the $m_{Lg}(f)$ residuals plot, even though γ and f is neither constant across earthquakes nor within a single earthquake, the definition of $m_{Lg}(f)$ accounts for the frequency of the observed wave and allows a meaningful comparison of residuals.

Figure 2.16 shows that the residuals are relatively symmetric about the zero line from 150 km to around 1300 km, suggesting that 150 km is the lower epicentral distance limit and that 1300 km is the upper epicentral distance limit for which the Method 1 m_{bLg} and $m_{Lg}(f)$ should be calculated for these paths in North America.

In addition to Figures 2.5, 2.7, and 2.11, Figure 2.16 implies that there is no empirical preference for either the Method 1 m_{bLg} or $m_{Lg}(f)$. Equations (2.3) and (2.5) both valuably estimate M_w (SLU), and Equations (2.6) and (2.8) are particularly useful for Method 1 m_{bLg} or $m_{Lg}(f)$, respectively, less than or equal to 4.5.

CHAPTER 3: Method 2 Calculation of m_{bLg} and $m_{Lg}(f)$

3.1 Empirical Data Set

The initial dataset is comprised of 42 United States earthquakes from the years 2010 and 2011 with $3.01 \leq M_w \leq 5.65$, with M_w determined at Saint Louis University from regional moment tensor inversion (Herrmann *et al.*, 2011). The majority of earthquakes occurred in Oklahoma and Arkansas. The Virginia $M_w = 5.65$ on August 23, 2011, and the Oklahoma $M_w = 5.59$ on June 6, 2011, both included in the dataset, are the largest recorded earthquakes in the eastern United States. The number of m_{Lg} magnitude estimates vary from 4 to 661 for the earthquakes in the dataset.

After an initial check on the signal-to-noise ratio for all earthquakes, 7 earthquakes were excluded for an insufficient number of acceptable observations with which to calculate the appropriate magnitudes. Thus, 35 earthquakes met the threshold criteria in order to calculate m_{bLg} and $m_{Lg}(f)$ (Figure 3.1). For 19 of the 35 earthquakes, the USGS published m_{Lg} magnitudes, which are used to compare with those determined with our dataset.

3.2 Method 2 Calculation of m_{bLg} for Central and Eastern US Earthquakes

The goal of Method 2 is to estimate the NEIC m_{bLg} without explicitly finding the third-largest peak-to-peak amplitude. The following procedure describes the magnitude-calculation steps for each earthquake from its associated stations. To begin Method 1, ground velocity from each station, derived by deconvolving the original instrument

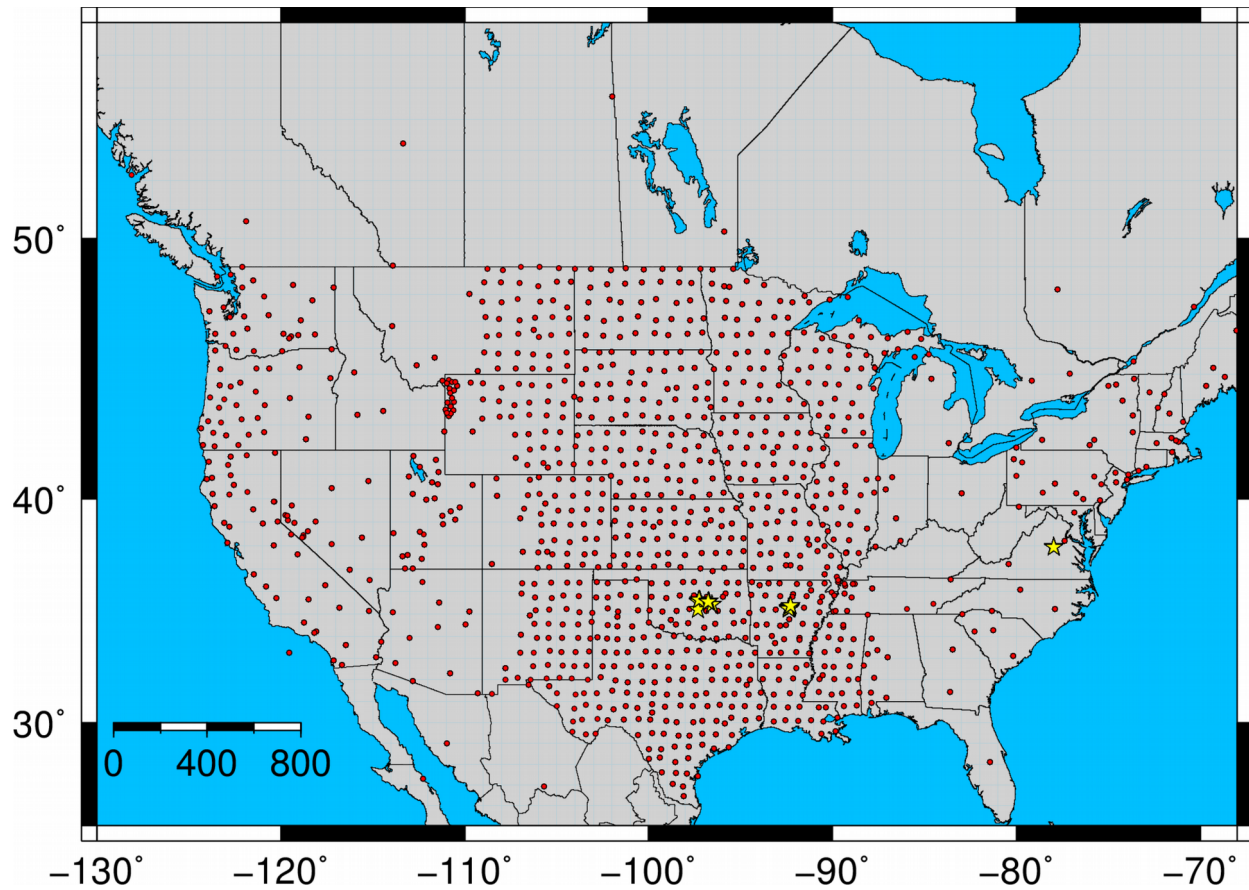


Figure 3.1. A map of the locations of the epicenters (yellow stars) of the 35 earthquakes for which magnitudes were calculated. The stations (red dots) include every station that recorded motion from any of the earthquakes. The Method 2 calculation of magnitudes eliminated many seismograms, and thus only a subset of stations was used for any given earthquake.

response, is convolved with the velocity response of the WWSSN short-period instrument in order to form the seismogram. Table 3.1 lists the parameters of the WWSSN short-period velocity response, and Figure 3.2 plots the velocity response.

For each waveform, a signal-to-noise test eliminates those stations with insufficiently distinguishable signals. Frequencies between 0.12 and 0.25 Hz are rejected in order to eliminate microseisms. The last 100 seconds of the seismogram are cut and labeled as noise. The part of the seismogram in the group velocity window between 3.2 and 3.6 km/s is labeled as signal. The positive peak amplitudes for both the noise and the signal are found. A trace is rejected if the peak signal amplitude is less than 3 times the peak noise amplitude.

For those seismograms that are selected, the peak positive amplitude and the peak negative amplitude are found. An estimate of half the maximum peak-to-peak amplitude is

$$A_{z-p} = \frac{|A_p| + |A_n|}{2} \quad (3.1)$$

where A_p is the maximum peak and A_n is the lowest trough. There is no requirement that the A_p and A_n be measured from the same signal cycle. Since the calculation of the NEIC m_{bLg} requires half the instrument-corrected third-largest peak-to-peak amplitude, a factor reduces A_{z-p} for the estimation. The factor was determined by empirically ascertaining an approximate ratio between A_{z-p} and A :

$$A = 0.7 A_{z-p} \quad (3.2)$$

where A is an estimate of half the third-largest instrument-corrected peak-to-peak amplitude.

Table 3.1. The table lists the parameters for the WWSSN short-period velocity response.

CONSTANT	532.1425
ZEROS	
0.000	0.000
0.000	0.000
POLES	
-3.725	6.220
-3.725	-6.220
-5.612	0.000
-13.240	0.000
-21.080	0.000

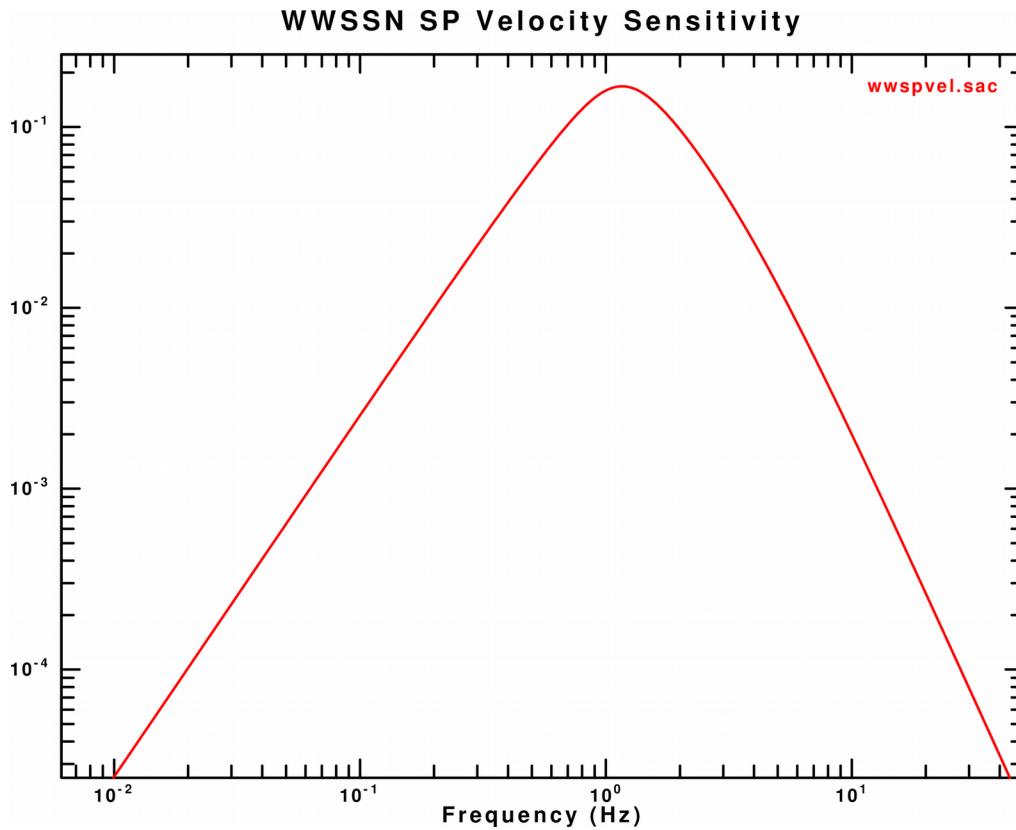


Figure 3.2. The velocity response of the WWSSN short-period instrument.

An estimate of the frequency is the frequency of zero crossings from spectral moments, described in Chapter 4. If the frequency of zero crossings is between 0.77 and 1.43 Hz, the seismogram proceeds; otherwise, the seismogram is rejected from further processing. For those seismograms containing an A in the appropriate frequency range, the m_{bLg} is then calculated for each station from

$$m_{bLg} = 2.96 + 0.8333\log_{10}\left(\frac{r}{10}\right) + .4343\gamma r + \log_{10}A \quad \text{for } 50 \text{ km} \leq r \leq 1110 \text{ km} \quad (3.3)$$

where γ is set at 0.00063 km^{-1} . A 25% trimmed mean is employed in order to determine a single magnitude for an earthquake. In the 25% trimmed mean method, magnitude estimates are sorted in increasing order, and the top 25% and the bottom 25% of values are cut. The remaining values each have equal weighting in the average. See figure 3.3 for a flowchart of the procedure for Method 2.

3.3 Method 2 Calculation of $m_{Lg}(f)$

The procedure for calculating $m_{Lg}(f)$ using Method 2 is the same as the procedure for calculating m_{bLg} using Method 2 except for one difference: the frequency f is used to derive the coefficient of anelastic attenuation γ . The following formula is used, as determined appropriate for the central United States by Herrmann and Kijko (1983a),

$$\gamma = 0.001f^{0.7}. \quad (3.4)$$

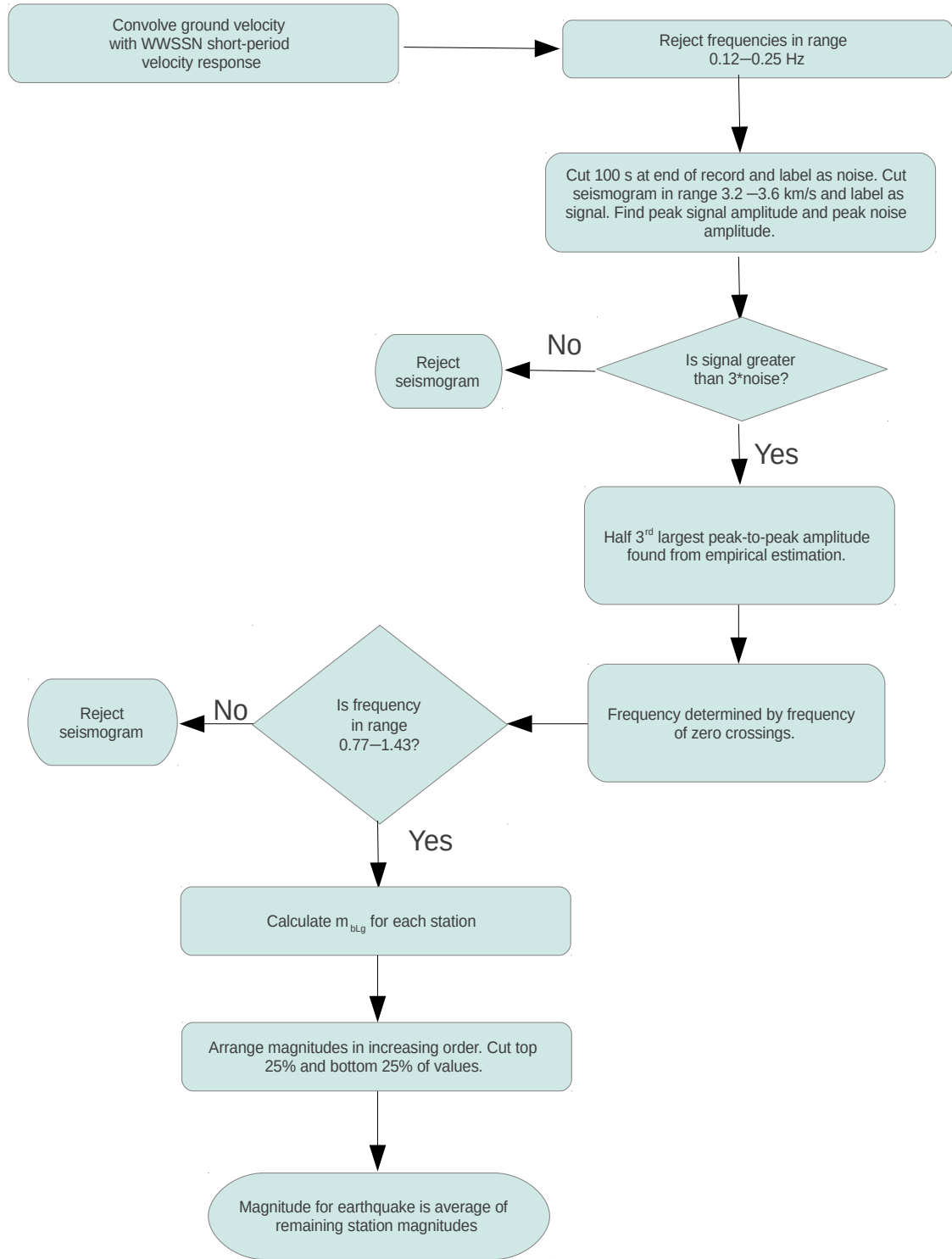


Figure 3.3. Flowchart for Method 2 calculation of m_{bLg} .

3.4 Method 2 m_{bLg} Results and Discussion

Figure 3.4 compares the regression analysis for M_w (SLU) versus Method 2 m_{bLg} to the regression analysis for M_w (SLU) versus Method 1 m_{bLg} . Rather than compare Method 2 to the published NEIC data, a comparison between Method 2 and Method 1 is more pertinent because Method 1, as Figure 2.9 shows, adequately replicates the NEIC procedure. In addition, the datasets of Methods 1 and 2 have more earthquakes in common than the datasets of Method 2 and the NEIC. The linear regression estimate of M_w (SLU) for a given Method 2 m_{bLg} is

$$M_w = 0.31 + 0.86m_{bLg}. \quad (3.5)$$

The slope error is 0.067, which is about 8% of the estimated slope from Equation (3.5), and the intercept error is 0.279, which is about 90% of the estimated intercept from Equation (3.5). The sample variance is 0.02. The coefficient of determination r^2 is 0.95, indicating that 95% of the variation in the predicted M_w (SLU) is explained by a linear relationship between Method 2 m_{bLg} and M_w (SLU). The red line in Figure 3.4 is the regression equation. The inner blue lines represent the 95% confidence interval on the regression line, and the outer blue lines represent the 95% prediction interval for new observations.

The errors in the Method 2 m_{bLg} regression analysis are larger than the errors in the Method 1 m_{bLg} regression. However, Equation (3.5) produces M_w (SLU) predictions that are within 0.1 magnitude units of Equation (2.3) for lower m_{bLg} and within .05 magnitudes units at the larger m_{bLg} . As an example, for $M_w = 4$ Equation (2.3) requires $m_{bLg} = 4.20$ and Equation (3.5) requires $m_{bLg} = 4.29$. Because data are sparse at larger

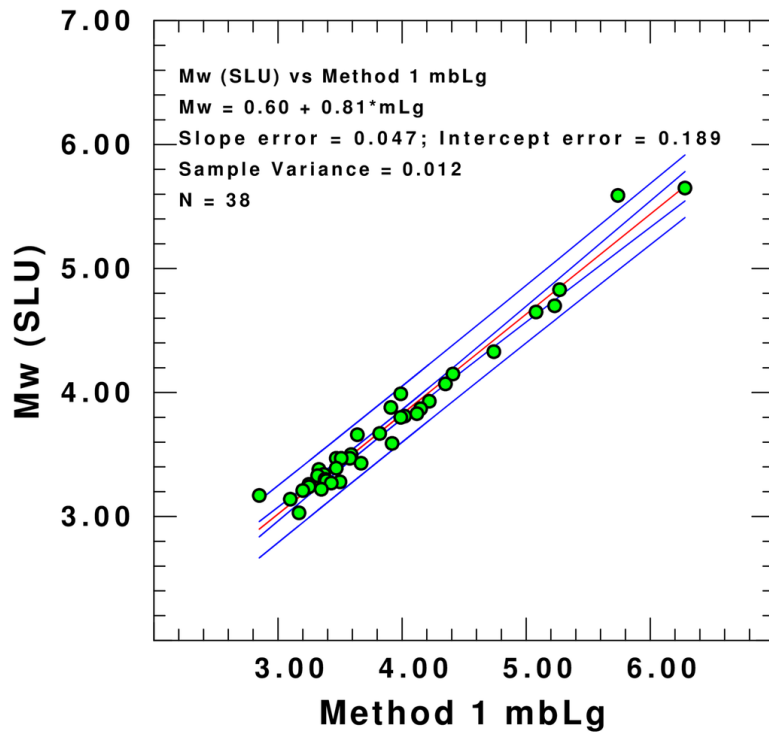
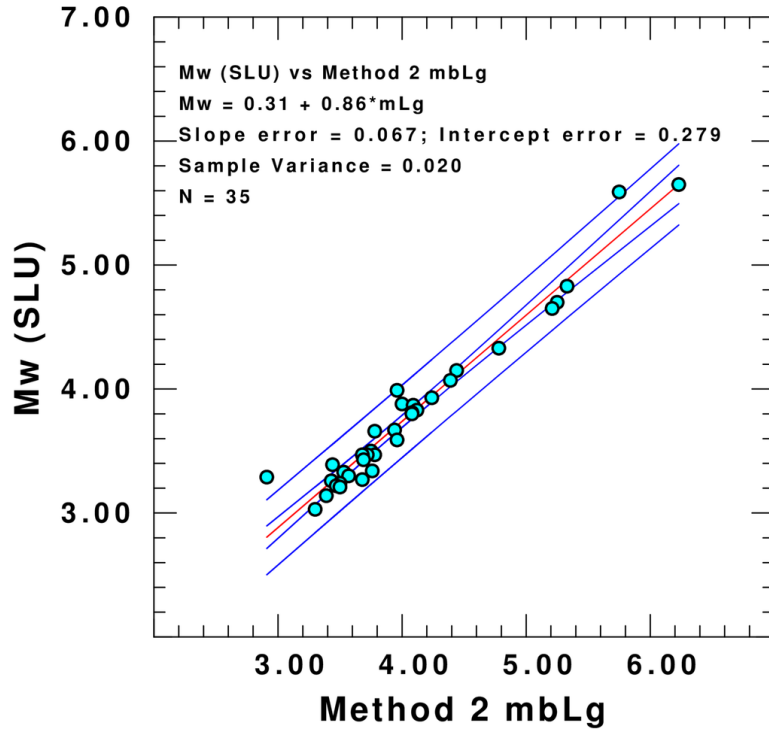


Figure 3.4. Regression analysis for the Method 2 m_{bLg} compared against the regression analysis for the Method 1 m_{bLg} . The red line is the regression line, the inner blue lines are the confidence intervals, and the outer blue lines are the prediction intervals.

magnitudes, little weight should be placed on the predictive ability of Method 2 m_{bLg} at those magnitudes. Thus, at the lower magnitudes, in the range in which the m_{bLg} versus M_w (SLU) relation is the most important, Equation (2.3) is superior to Equation (3.5).

3.5 Method 2 $m_{Lg}(f)$ Results and Discussion

Figure 3.5 compares the regression analysis for M_w (SLU) versus Method 2 $m_{Lg}(f)$ against the regression analysis for M_w (SLU) versus Method 1 m_{bLg} . The linear regression estimate of M_w (SLU) for a given Method 2 $m_{Lg}(f)$ is

$$M_w = 0.31 + 0.83m_{bLg}. \quad (3.6)$$

The slope error is 0.073, which is about 9% of the estimated slope from Equation (3.6), and the intercept error is 0.311, which is about 100% of the estimated intercept from Equation (3.6). The sample variance is 0.025. The coefficient of determination r^2 is 0.94, indicating that 94% of the variation in the predicted M_w (SLU) is explained by a linear relationship between Method 2 $m_{Lg}(f)$ and M_w (SLU). The red line in Figure 3.5 is the regression equation. The inner blue lines represent the 95% confidence interval on the regression line, and the outer blue lines represent the 95% prediction interval for new data.

Compared to Equation (2.5), Equation (3.6) is inferior in predicting M_w (SLU) at the lower end magnitudes. One advantage of Method 2 $m_{Lg}(f)$ over Method 1 $m_{Lg}(f)$ might be the computation time, since Method 2 does not use the WWSSN short-period displacement response to ascertain the third-largest peak-to-peak amplitude. However, computing the frequency of zero crossings requires additional time, and the total

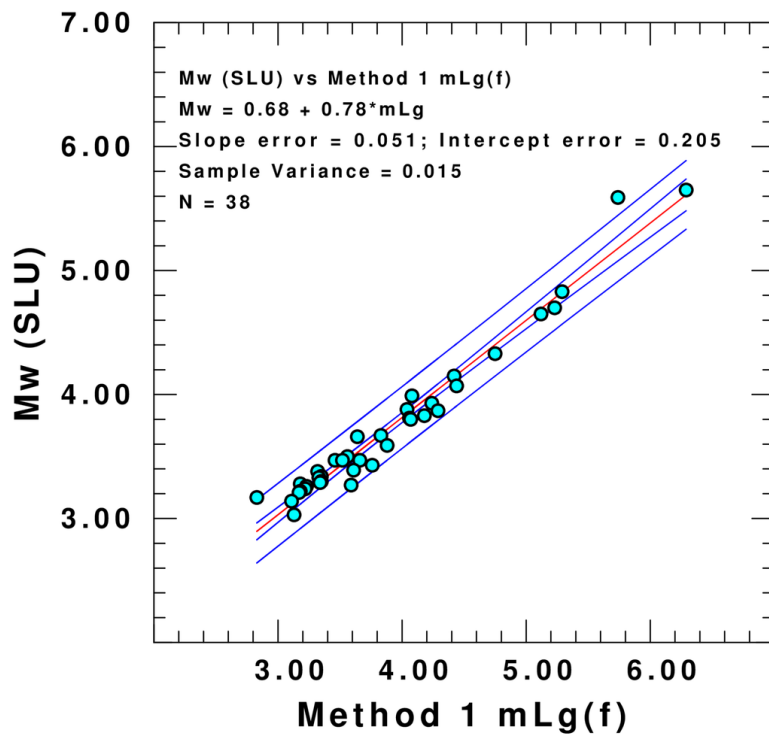
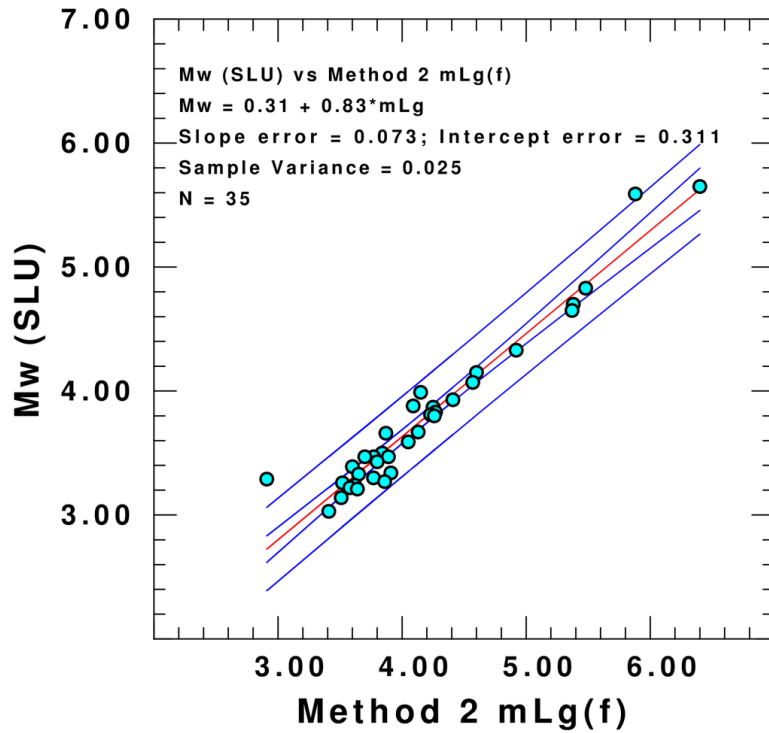


Figure 3.5. Regression analysis for Method 2 $m_{Lg}(f)$ compared against the regression analysis for Method 1 $m_{Lg}(f)$. The red line is the regression line, the inner blue lines are the confidence intervals, and the outer blue lines are the prediction intervals.

computation time for both Methods 1 and 2 is similar. Thus, Method 2 $m_{Lg}(f)$ should not be used if Method 1 $m_{Lg}(f)$ is feasible.

3.6 Comparisons of Method 1 m_{bLg} , Method 1 $m_{Lg}(f)$, Method 2 m_{bLg} , and Method 2 $m_{Lg}(f)$

Figure 3.6 compares the Method 2 m_{bLg} versus the Method 1 m_{bLg} for the 35 common events. The reference line shows a 1-to-1 relationship. Figure 3.6 confirms that the Method 2 m_{bLg} is at least 0.1 magnitude units larger than the Method 1 m_{bLg} for the smaller magnitudes and also shows a dependence on magnitude. The relationship provides further support for the use of the Method 1 m_{bLg} over the simplified Method 2 m_{bLg} for smaller magnitudes.

Figures 3.7 compares the Method 2 $m_{Lg}(f)$ versus the Method 1 $m_{Lg}(f)$ for the 35 common events. The reference line shows a 1-to-1 relationship. Figure 3.7 shows that nearly every Method 2 $m_{Lg}(f)$ is larger than the corresponding Method 1 $m_{Lg}(f)$. This noticeable disparity corroborates the use of Method 1 $m_{Lg}(f)$ over Method 2 $m_{Lg}(f)$.

3.7 Adjustments to the Method 2 Lg magnitude relationships

Figure 3.8 shows an attempt to fit the M_w (SLU) as a function of the Method 2 m_{bLg} using a bilinear relationship. In fitting the data at smaller magnitudes, an expected slope of 2/3 is used as a guide in selecting the magnitude range. The slope used for larger magnitudes is compatible with the data. The equations are

$$M_w = 1.02 + 0.67m_{bLg} \quad \text{for } 2.0 < m_{bLg} < 4.3 \quad (3.7)$$

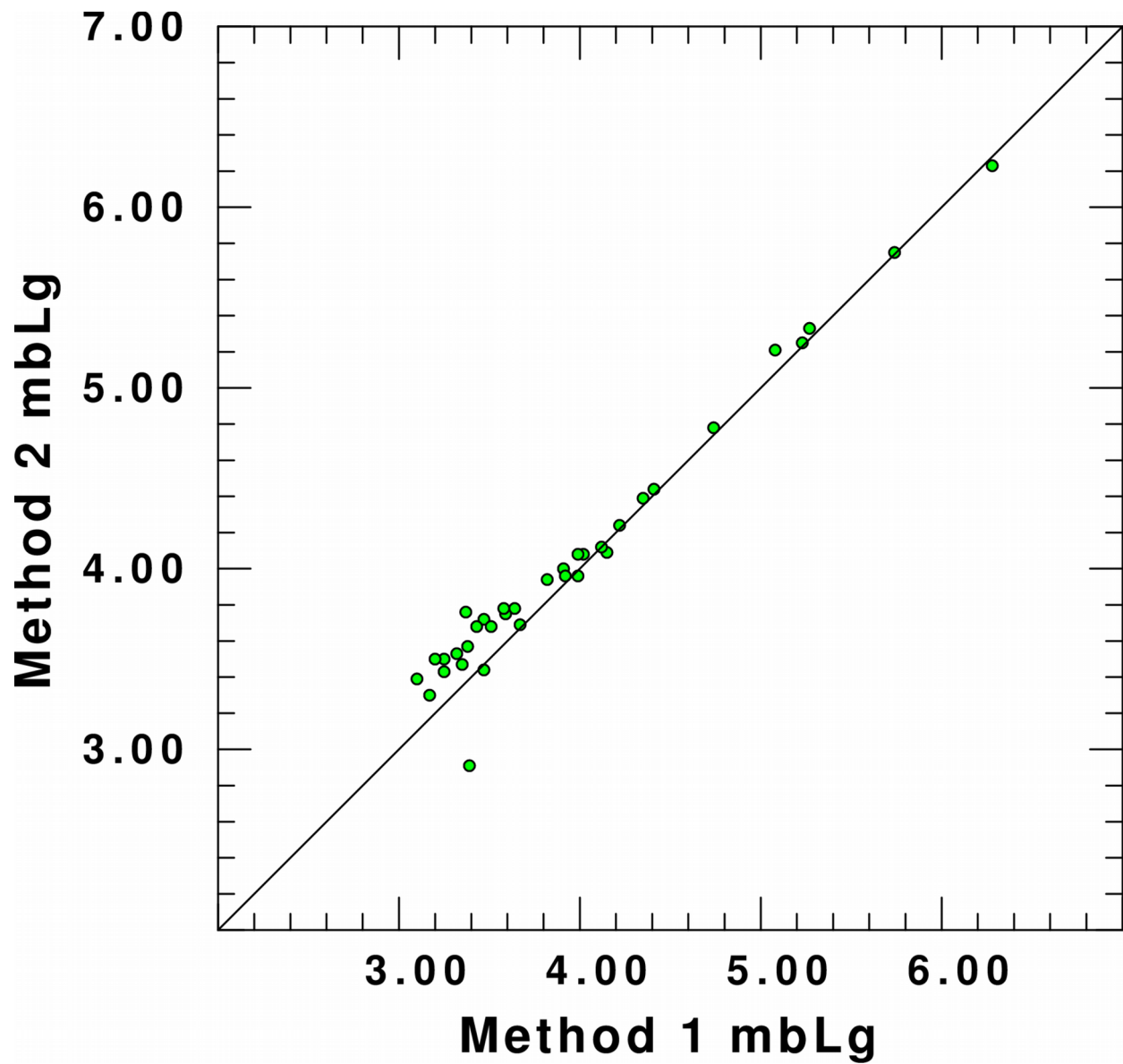


Figure 3.6. A plot of the Method 2 m_{bLg} versus the Method 1 m_{bLg} for the 35 earthquakes common to both groups.

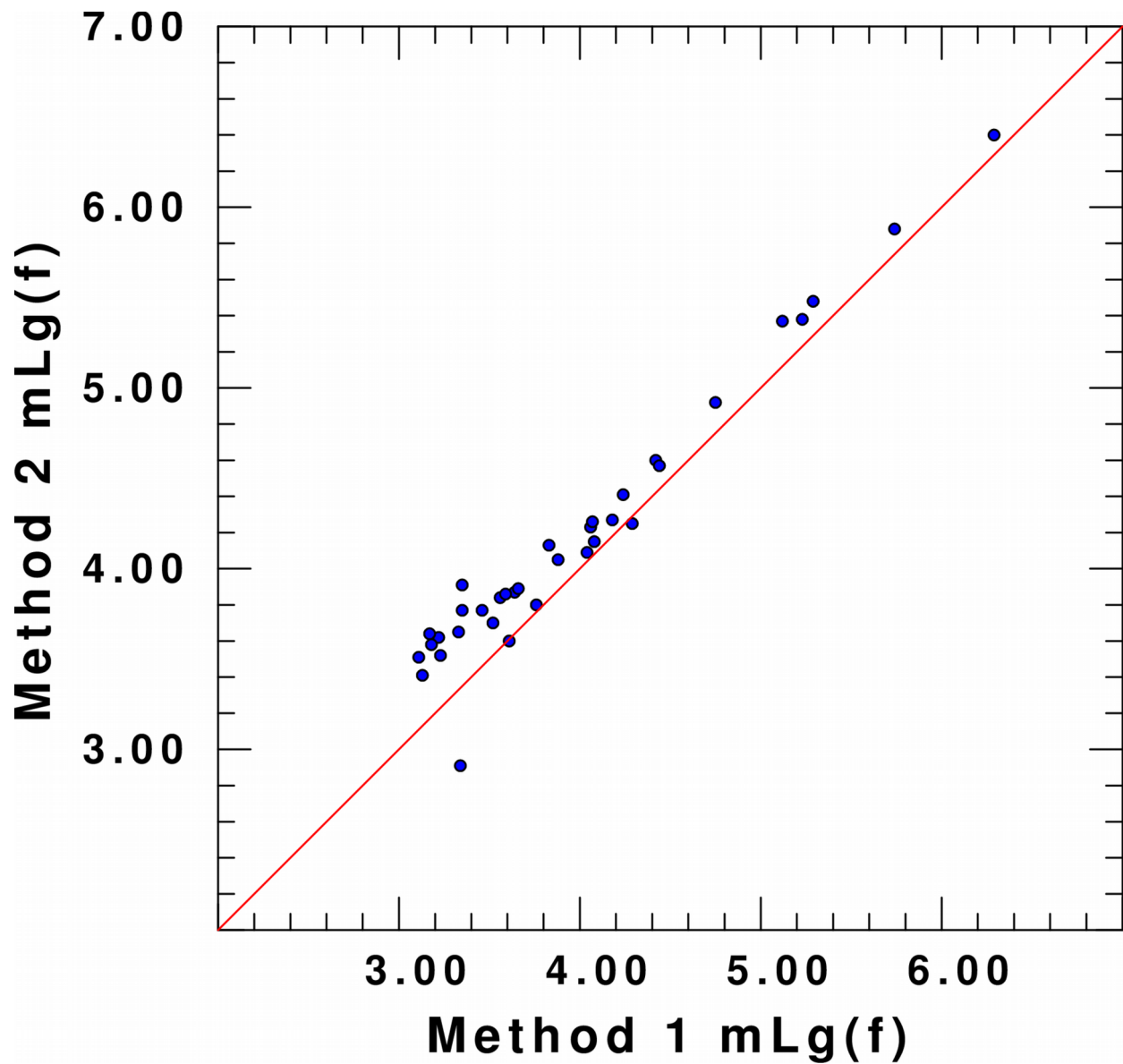


Figure 3.7. A plot of the Method 2 $m_{Lg}(f)$ versus the Method 1 $m_{Lg}(f)$ for the 35 earthquakes common to both groups.

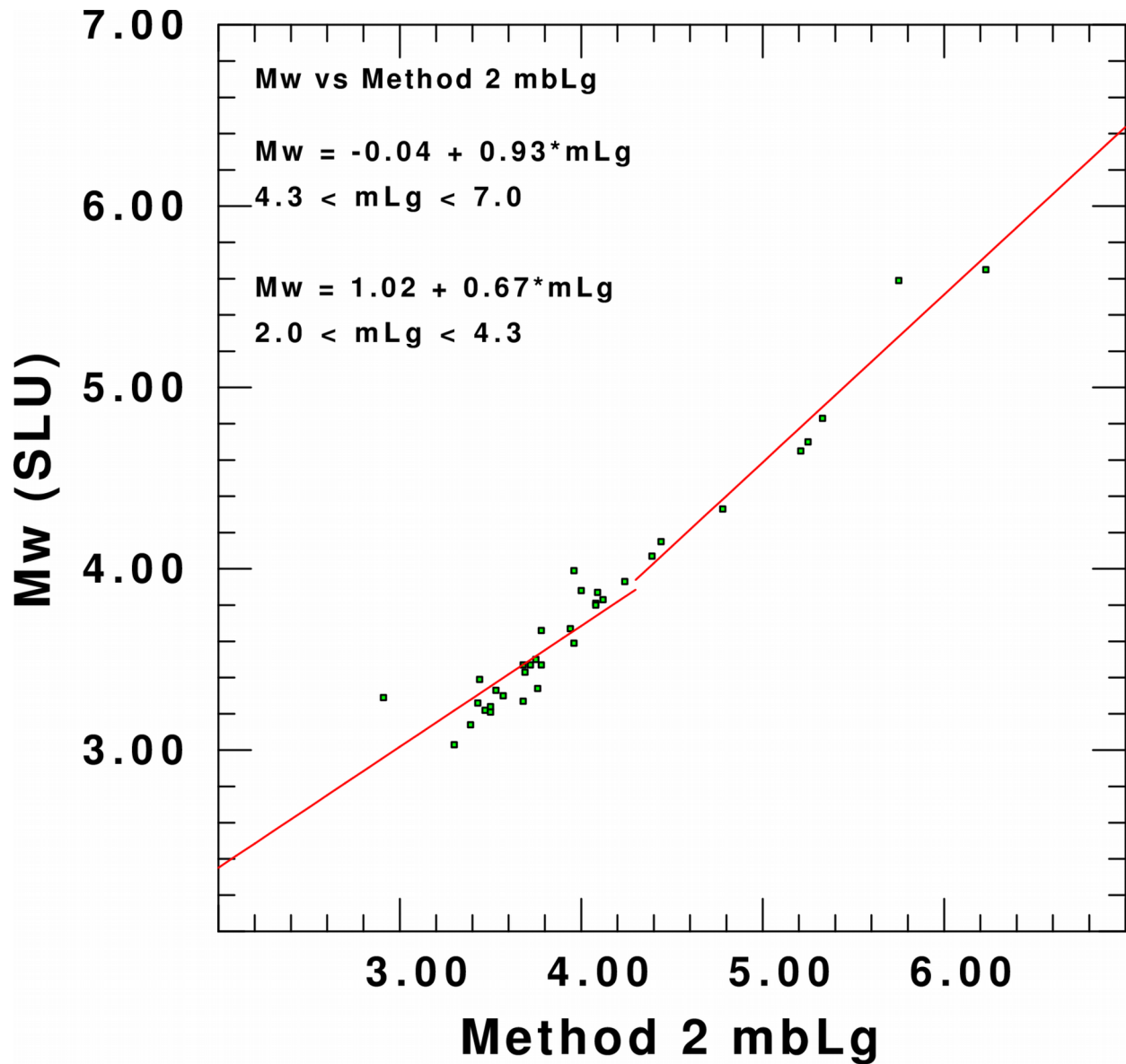


Figure 3.8. A regression graph of the M_w (SLU) versus the Method 2 m_{bLg} based on a bilinear division. Modeling, described in Chapter 4, and empirical iterations of a regression program suggest that the regression line slope change at around $m_{bLg} = 4.3$. For the regression line for smaller magnitudes, the slope is fixed at $2/3$. For the regression line for larger magnitudes, the slope is determined by the data.

$$M_w = -0.04 + 0.93m_{bLg} \text{ for } 4.3 < m_{bLg} < 7.0 \quad (3.8)$$

where the breakpoint $m_{bLg} = 4.3$ was chosen based on modeling (Chapter 4) and empirical iterations of a regression program.

Figure 3.9 shows an attempt to fit the M_w (SLU) as a function of $m_{Lg}(f)$ using a bilinear relationship. No expected slope or intercept is used as a guide for the regression equations; the data determine both. The equations are

$$M_w = 0.90 + 0.68m_{Lg}(f) \text{ for } 2.0 < m_{Lg}(f) < 5.0 \quad (3.9)$$

$$M_w = -0.16 + 0.92m_{Lg}(f) \text{ for } 5.0 < m_{Lg}(f) < 7.0 \quad (3.10)$$

where the breakpoint $m_{Lg}(f) = 5.0$ was chosen based on modeling (Chapter 4) and empirical iterations of a regression program.

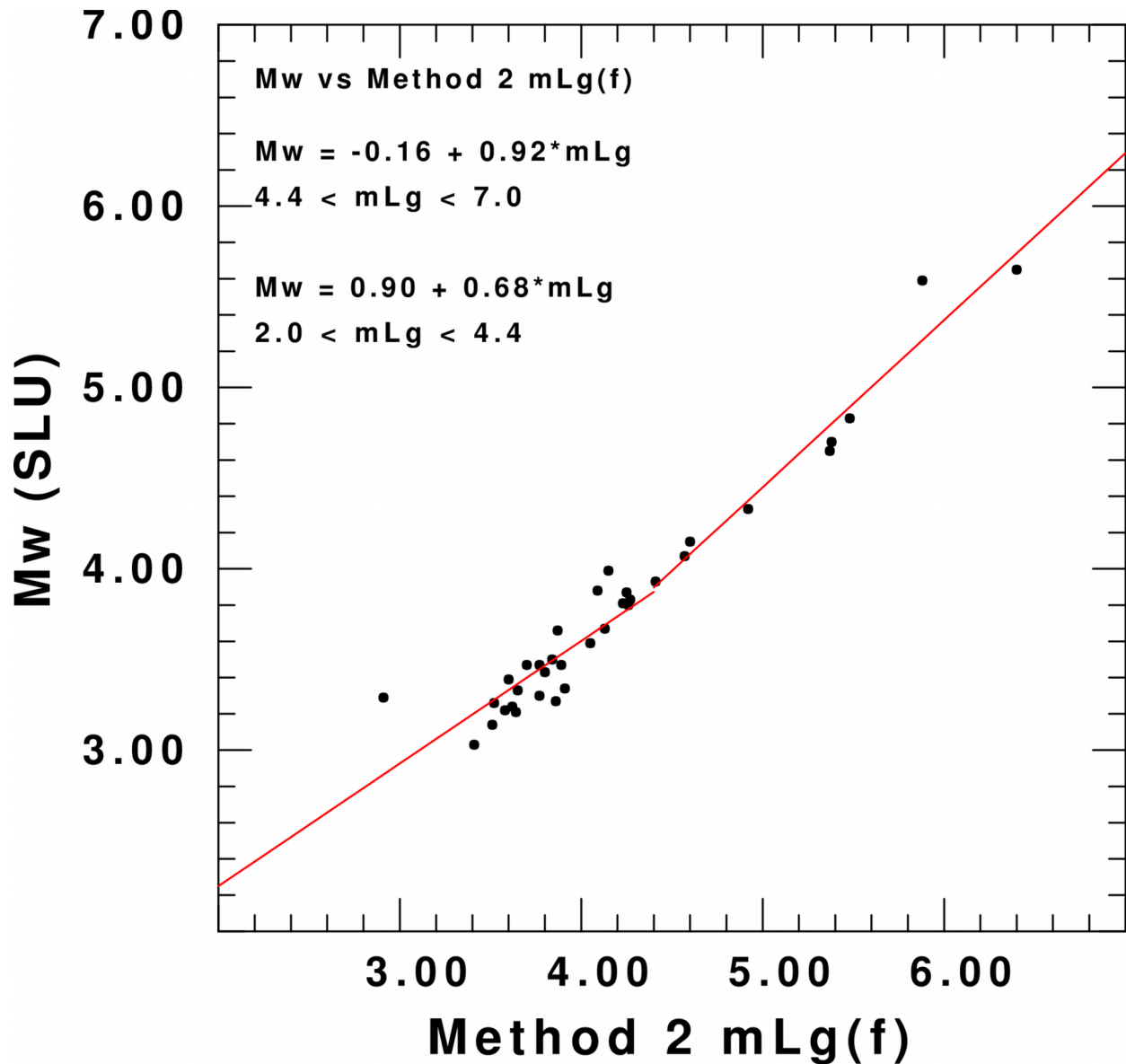


Figure 3.9. A regression graph of the M_w (SLU) versus the Method 2 $m_{Lg}(f)$ based on a bilinear division. Modeling, described in Chapter 4, and empirical iterations of a regression program suggest that the regression line slope change at around $m_{Lg}(f) = 4.4$.

CHAPTER 4: Modeling

Boore (1983) developed the primary components of the stochastic method for estimating peak earthquake ground motion parameters, and Boore (2003) improved the method to make the method compatible with other implementations. The description of the stochastic method and random vibration theory equations used in this thesis follow the development in Boore (2003).

4.1 Stochastic Method

The spectrum of ground motion can be represented as

$$A(M_0, r, f) = E(M_0, f)P(r, f)G(f), \text{ where} \quad (4.1)$$

$E(M_0, f)$ is the source spectrum,
 $P(r, f)$ describes the propagation effects,
 $G(f)$ is a local site modification which can be separated into an amplification term and a frequency-dependent attenuation term of the form $(1 + (f / f_{\max})^{\theta})^{-1/2}$ or $e^{-\pi f \tau}$,
 M_0 is the seismic moment in dyne-cm,
 r is the epicentral distance in km, and
 f is the frequency in Hz.

The source spectrum $E(M_0, f)$ can be represented as

$$E(M_0, f) = CM_0 S(M_0, f), \text{ where} \quad (4.2)$$

$$C = \frac{\langle R_{\theta\phi} \rangle VF}{4\pi\rho_s\beta_s^3 R_0}$$

$S(M_0, f)$ is the displacement source spectrum,
 $\langle R_{\theta\phi} \rangle$ is the average radiation pattern,
 V accounts for the partition of amplitude onto the horizontal components,
 F is the free surface effect, typically 2,
 ρ_s is the density at the source in kg/km^3 ,
 β_s is the S-wave velocity at the source in km/s , and
 R_0 is a reference distance, usually 1 km.

The path effect $P(r, f)$ can be represented as

$$P(r, f) = Z(r)e^{\frac{-\pi fr}{Q(f)c_Q}}, \text{ where} \quad (4.3)$$

$Z(r)$ is a geometrical spreading function,
 $Q(f)$ is the quality factor $Q(f) = Q_0 f^n$, and
 c_Q is the group velocity of the phase.

The site modification $G(f)$ is a factor that accounts for both amplification and attenuation due to the shallow structure beneath the observation point. Even though $P(r, f)$ might possibly incorporate the local site effects, having a separate term $G(f)$ allows modifications for particularly disparate conditions, such as loose sediments or a specific rock suite.

If passed through an instrument, the spectrum of the recorded motion

$$A(M_0, r, f) = Y(f)I(f), \text{ where} \quad (4.4)$$

$Y(f)$ accounts for the source spectrum and the site and propagation effects and $I(f)$ is a filter function.

The filter function $I(f)$ can be used for generic ground motion or as the representation of a particular instrument. If used for ground motion parameters,

$$I(f) = (2\pi fi)^n, \text{ where} \quad (4.5)$$

$n = 0, 1,$ and 2 are used for ground displacement, velocity or acceleration, respectively.

In this study, $I(f)$ is the frequency representation of the WWSSN short-period instrument.

4.2 Random Vibration Theory

Random vibration theory is the study of non-periodic, stochastic functions in order to predict peak motions, without having or requiring the ability to determine a

specific measurement at a specific time. Random vibration theory assumes a stationary process, and although seismic waves are nonstationary, random vibration theory satisfactorily predicts peak motions; thus, seismic waves can be modeled as stationary processes.

Given the spectrum of the observed signal and the duration, the following equations (Cartwright and Longuet-Higgins, 1956) are used to predict the peak motion of interest. The ratio of the peak motion to the root-mean-square is a function of the spectrum and duration:

$$\frac{a_{max}}{a_{rms}} = \int_{-\infty}^{\infty} \{1 - [1 - \xi e^{-z^2}]^{N_e}\} dz, \quad \text{where} \quad (4.6)$$

N_z is the number of zero crossings during the studied time frame,
 N_e is the number of extrema during the same interval, and

$$\xi = \frac{N_z}{N_e}.$$

For sinusoidal motion $N_z = N_e$, but otherwise $N_e > N_z$.

$$N_{z,e} = 2f_{z,e}T \quad (4.7)$$

The two frequencies $f_{z,e}$ are predominant frequencies given by the two equations:

$$f_z = \frac{1}{2\pi}(m_2/m_0)^{1/2} \quad \text{and} \quad (4.8)$$

$$f_e = \frac{1}{2\pi}(m_4/m_2)^{1/2} . \quad (4.9)$$

The root-mean-square is given by

$$a_{rms} = (m_0/T)^{1/2} . \quad (4.10)$$

The m_k in the above equations are various statistical moments calculated from the spectrum $A(f)$

$$m_k = \int_{-\infty}^{\infty} (2\pi f)^k |A^2(f)| df \quad . \quad (4.11)$$

Note that the estimations of the Lg frequency used in the Method 2 m_{bLg} and $m_{Lg}(f)$ computations of Chapter 3 were determined from Equation (4.8).

4.3 Models

For the stochastic method simulations and random vibration theory estimates, 3 models were employed. Two of the models come from Frankel (1996) and the other model is from Atkinson and Boore (1995). Tables 4.1–4.3 give summaries of the models. The biggest differences among the models occur in the distance-dependent duration, site response, and number of corner frequencies. The model in Table 4.3 has five distance-dependent duration terms, and the models in Tables 4.1 and 4.2 only have two. The model from Table 4.1 has seven site response terms, and the other two models have a maximum of two. Finally, the model in Table 4.3 assumes two corner frequencies for an earthquake waveform.

Tables 4.1 and 4.2 include a stress drop $\Delta\sigma$ that is related to the corner frequency of the acceleration spectrum by

$$f_c = 4.9(10^6)\beta_s(\Delta\sigma/M_0)^{1/3} \quad \text{where} \quad (4.12)$$

β_s is the shear-wave velocity near the source in km/s,
 $\Delta\sigma$ is the stress drop in bars, and
 M_0 is the seismic moment in dyne-cm.

The geometrical spreading function $Z(r)$ in Tables 4.1–4.3 is

$$Z(r) = \begin{cases} r^{-1} & 1 \leq r < 70 \text{ km} \\ r^0 & 70 \leq r < 130 \text{ km} \\ r^1 & 130 \text{ km} \leq r \end{cases} \quad \text{where} \quad (4.13)$$

r is the epicentral distance in km.

The ground-motion duration represented by the models in Tables 4.1 and 4.2 is the sum of $1/f_c$ and a distance-dependent function based on a linear interpolation of the three segments shown in Tables 4.1 and 4.2. The ground-motion duration represented by the model in Table 4.3 is the sum of $0.5/f_c$ and a distance-dependent function based on a linear interpolation of the five segments shown in Table 4.3.

The source spectra for Tables 4.1–4.3 include the displacement source spectra $S(M_0, f)$. For the models represented by Tables 4.1 and 4.2,

$$S(M_0, f) = \frac{1}{1 + (f/f_c)^2} \quad (4.14)$$

For the model represented by Table 4.3,

$$S(M_0, f) = \frac{1-\epsilon}{1 + (f/f_a)^2} + \frac{\epsilon}{1 + (f/f_b)^2} \quad \text{where} \quad (4.15)$$

ϵ is a dimensionless parameter,
 f_a is one corner frequency in Hz, and
 f_b is another corner frequency in Hz.

4.4 Modeling m_{bLg} versus M_w

Figures 4.1–4.3 compare the Method 1 m_{bLg} data points to the simulated m_{bLg} versus M_w relationship for the models described in Tables 4.1–4.3. The colored curves in Figures 4.1–4.3 define the relationships among the magnitudes at three different distances. In order to derive the relationships between m_{bLg} and M_w , the models use the instrument-corrected maximum zero-to-peak amplitude in the magnitude computations, while the Method 1 m_{bLg} points use half the instrument-corrected third-largest peak-to-peak amplitude. The adjustment given in (2.10) is not applied to the simulated m_{bLg} .

Table 4.1. Frankel *et al.* hard-rock model parameters.

κ (s^{-1})	0.006
Q_0 and η	680 0.36
c_0 (km/s)	3.6
β_s Source shear velocity (km/s)	3.6
ρ_s Source density (gm/cm ³)	2.8
Distance-dependent duration	
Distance (km)	Duration (s)
0.000	0.000
1000.00	50.000
Geometrical Spreading	
Distance (km)	Power
1.000	-1.000
70.000	0.000
130.000	-0.500
Site Response	
Frequency (Hz)	Amplification
0.1000	1.000
0.4079	1.074
0.8524	1.120
1.6300	1.154
3.5600	1.177
7.0250	1.187
13.9500	1.193
f_{max} (Hz)	100.0
V, Partition of amplitude onto horizontal components	0.71
F, Free surface effect	2.00
$\langle R_{\theta\phi} \rangle$, Radiation	0.55
$\Delta\sigma$, Stress drop (bars)	150

Table 4.2. Frankel *et al.* modified hard-rock model parameters. The modified hard-rock model contains a different site effect term.

κ (s^{-1})	0.006
Q_0 and η	680 0.36
c_Q (km/s)	3.6
β_s , Source shear velocity (km/s)	3.6
ρ_s , Source density (gm/cm^3)	2.8
Distance-dependent duration	
Distance (km)	Duration (s)
0.000	0.000
1000.00	50.000
Geometrical Spreading	
Distance (km)	Power
1.000	-1.000
70.000	0.000
130.000	-0.500
Site Response	
Frequency (Hz)	Amplification
100.0	1.0
f_{max} (Hz)	100.0
V, Partition of amplitude onto horizontal components	0.71
F, Free surface effect	2.00
$\langle R_{\theta\phi} \rangle$, Radiation	0.55
$\Delta\sigma$, Stress drop (bars)	150

Table 4.3. Atkinson and Boore model parameters.

κ (s^{-1})	0.000		
Q_0 and η	680	0.36	
c_Q (km/s)	3.8		
β_s , Source shear velocity (km/s)	3.8		
ρ_s , Source density (gm/cm^3)	2.8		
Distance-dependent duration			
Distance (km)	Duration (s)		
0.000	0.000		
10.00	0.000		
70.00	9.600		
130.00	7.800		
1000.0	42.60		
Geometrical Spreading			
Distance (km)	Power		
1.000	-1.000		
70.000	0.000		
130.000	-0.500		
Site Response			
Frequency (Hz)	Amplification		
0.010	1.000		
100.000	1.000		
f_{max} (Hz)	100.0		
V, partition of amplitude onto horizontal components	0.71		
F, free surface effect	2.00		
$\langle R_{\theta\phi} \rangle$, radiation	0.55		
<hr/>			
M_w Range	$\log f_a$	$\log f_b$	$\log \epsilon$
$M_w \geq 4$	$2.41 - 0.533M_w$	$1.43 - 0.188M_w$	$2.52 - 0.637M_w$
$M_w < 4$	$2.678 - 0.5M_w$	$2.678 - 0.5M_w$	0.0

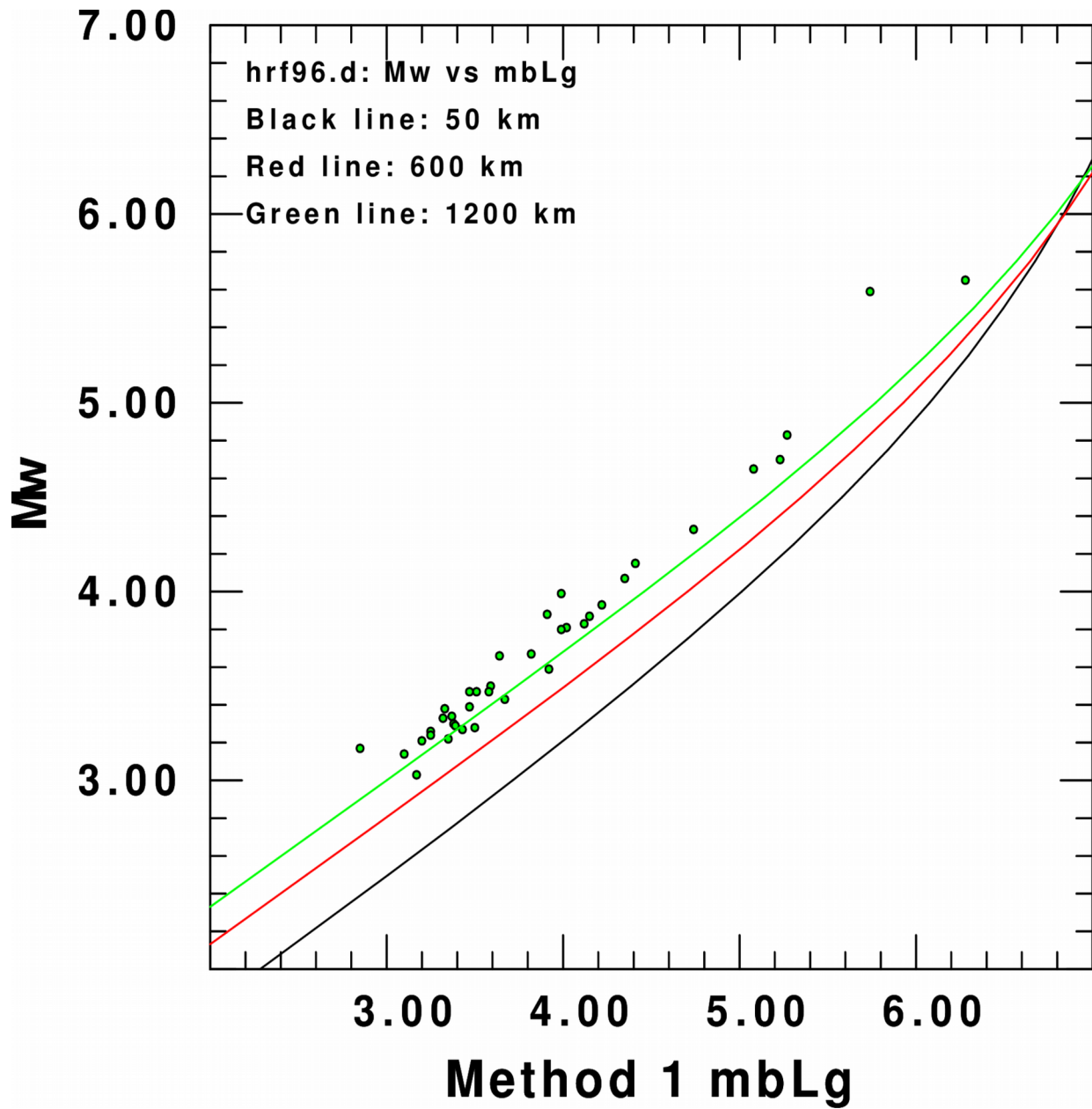


Figure 4.1. The Method 1 m_{bLg} data points lie over the m_{bLg} versus M_w relationship derived from the Frankel hard-rock model. The green, red, and black curves give the relationships between m_{bLg} and M_w for different constant epicentral distances. The model uses the instrument-corrected maximum zero-to-peak amplitude, while the Method 1 m_{bLg} points use half the instrument-corrected third-largest peak-to-peak amplitude.

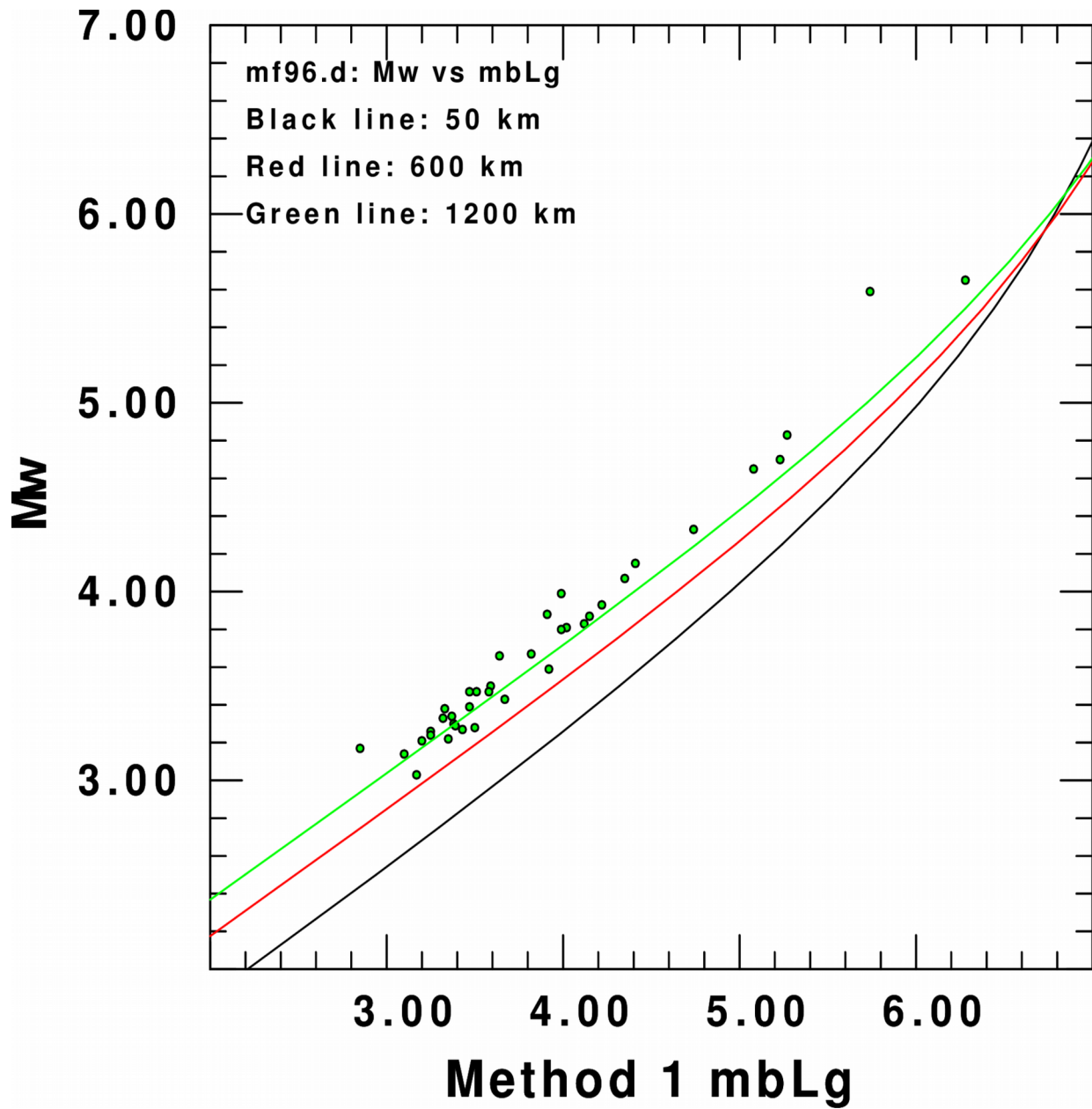


Figure 4.2. The Method 1 m_{bLg} data points lie over the m_{bLg} versus M_w relationship derived from the Frankel modified hard-rock model. The green, red, and black curves give the relationships between m_{bLg} and M_w for different constant epicentral distances. The model uses the instrument-corrected maximum zero-to-peak amplitude, while the Method 1 m_{bLg} points use half the instrument-corrected third-largest peak-to-peak amplitude.

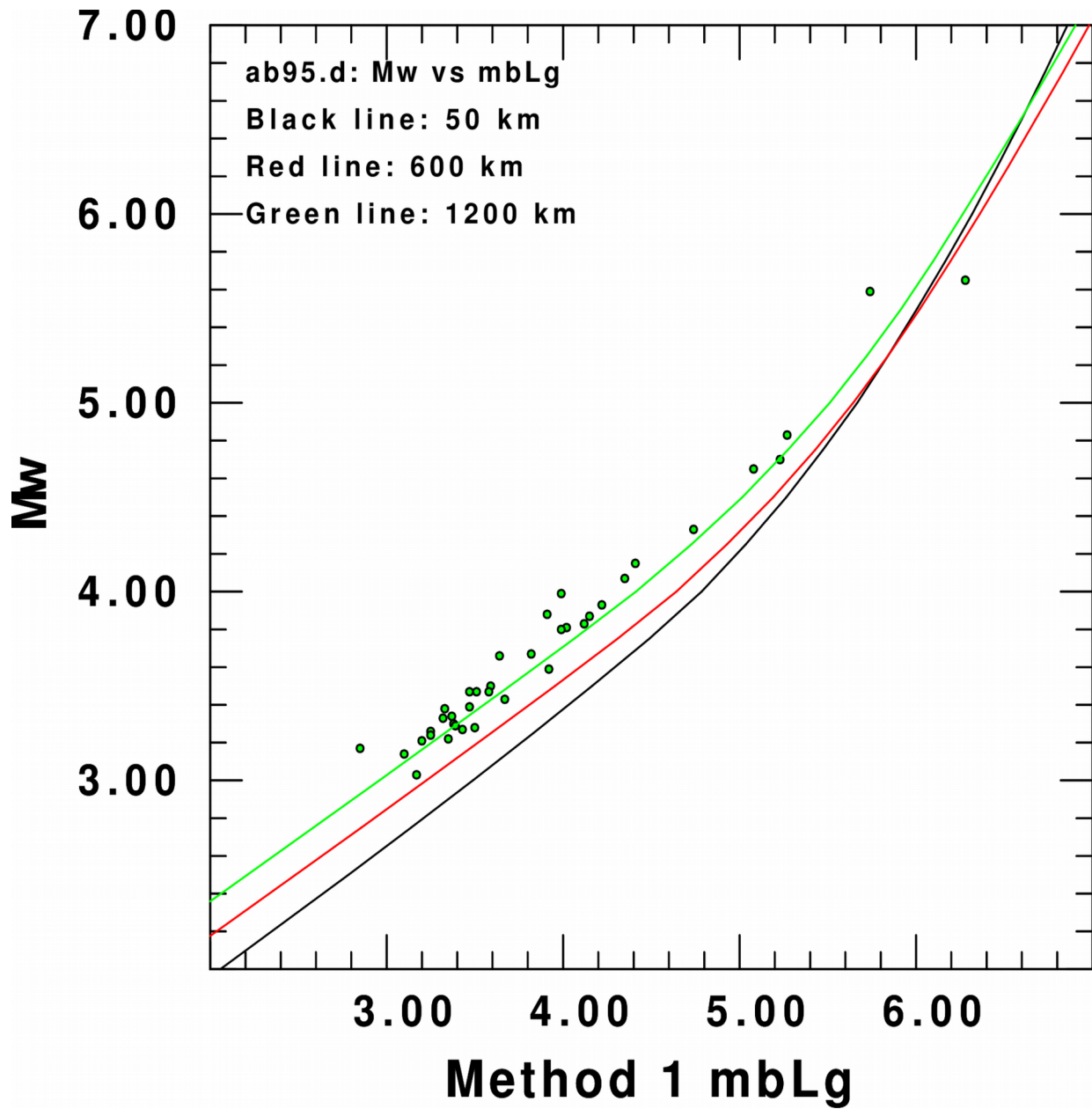


Figure 4.3. The Method 1 m_{bLg} data points lie over the m_{bLg} versus M_w relationship derived from the Atkinson-Boore model. The green, red, and black curves give the relationships between m_{bLg} and M_w for different constant epicentral distances. The model uses the instrument-corrected maximum zero-to-peak amplitude, while the Method 1 m_{bLg} points use half the instrument-corrected third-largest peak-to-peak amplitude.

A conspicuous feature of Figures 4.1–4.3 is the effect of distance on the relationship between m_{bLg} and M_w . For the primary m_{bLg} range of interest, m_{bLg} less than 5.0, an M_w prediction can vary by up 0.5 magnitude units depending upon the distance curve. In addition, the general trend is that an m_{bLg} observed at 50 km produces a smaller M_w prediction than the same m_{bLg} observed at 1200 km. The distance effect on the relationship between m_{bLg} and M_w suggests that computing a composite m_{bLg} based on a 25% trimmed mean may be problematic to model. A possible solution to this problem is binning m_{bLg} by distance and then computing an average for each bin; however, for the solution to be feasible, sufficient station coverage at several epicentral distances is necessary. The distinguishing feature of the three ground motion models, which are based on measured ground motion, is that $\gamma = \pi f/c_q Q(f)$ is not independent of frequency.

4.5 Modeling $m_{Lg}(f)$ versus M_w

Figures 4.4–4.6 compare the observed Method 1 $m_{Lg}(f)$ data points to the simulated $m_{Lg}(f)$ versus M_w relationship for the different models described in Tables 4.1–4.3. The colored curves in Figures 4.4–4.6 define the relationships among the magnitudes for three different distances. In order to derive the relationships between $m_{Lg}(f)$ and M_w , the models use the instrument-corrected maximum zero-to-peak amplitude in the magnitude computations, while the Method 1 m_{bLg} points use half the instrument-corrected third-largest peak-to-peak amplitude.

There are two conspicuous features of Figures 4.4–4.6, especially compared to

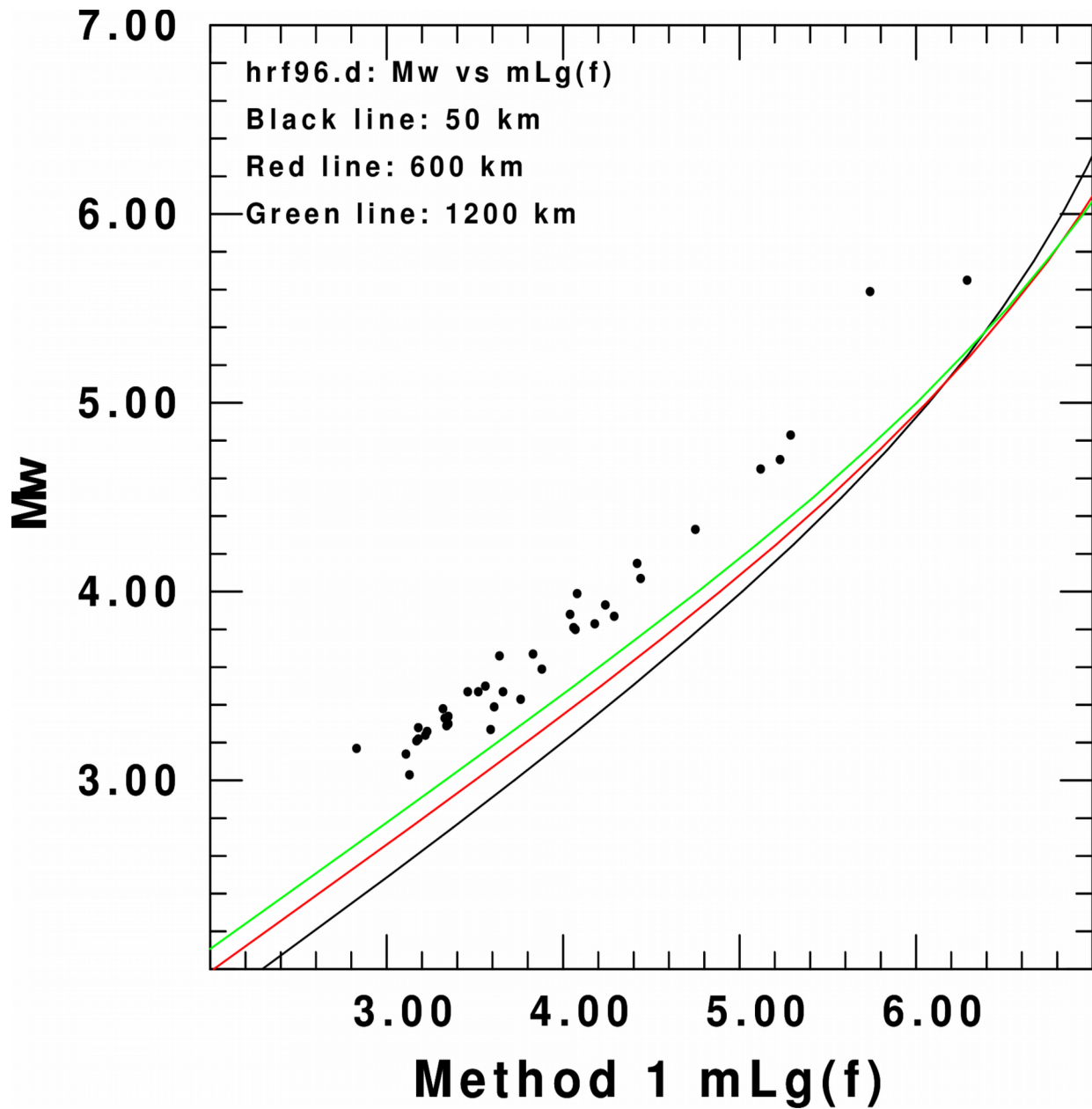


Figure 4.4. The Method 1 $m_{Lg}(f)$ data points lie over the $m_{Lg}(f)$ versus M_w relationship derived from the Frankel hard-rock model. The green, red, and black curves give the relationship between $m_{Lg}(f)$ and M_w for different constant epicentral distances. The model uses the instrument-corrected maximum zero-to-peak amplitude, while the Method 1 $m_{Lg}(f)$ points use half the instrument-corrected third-largest peak-to-peak amplitude.

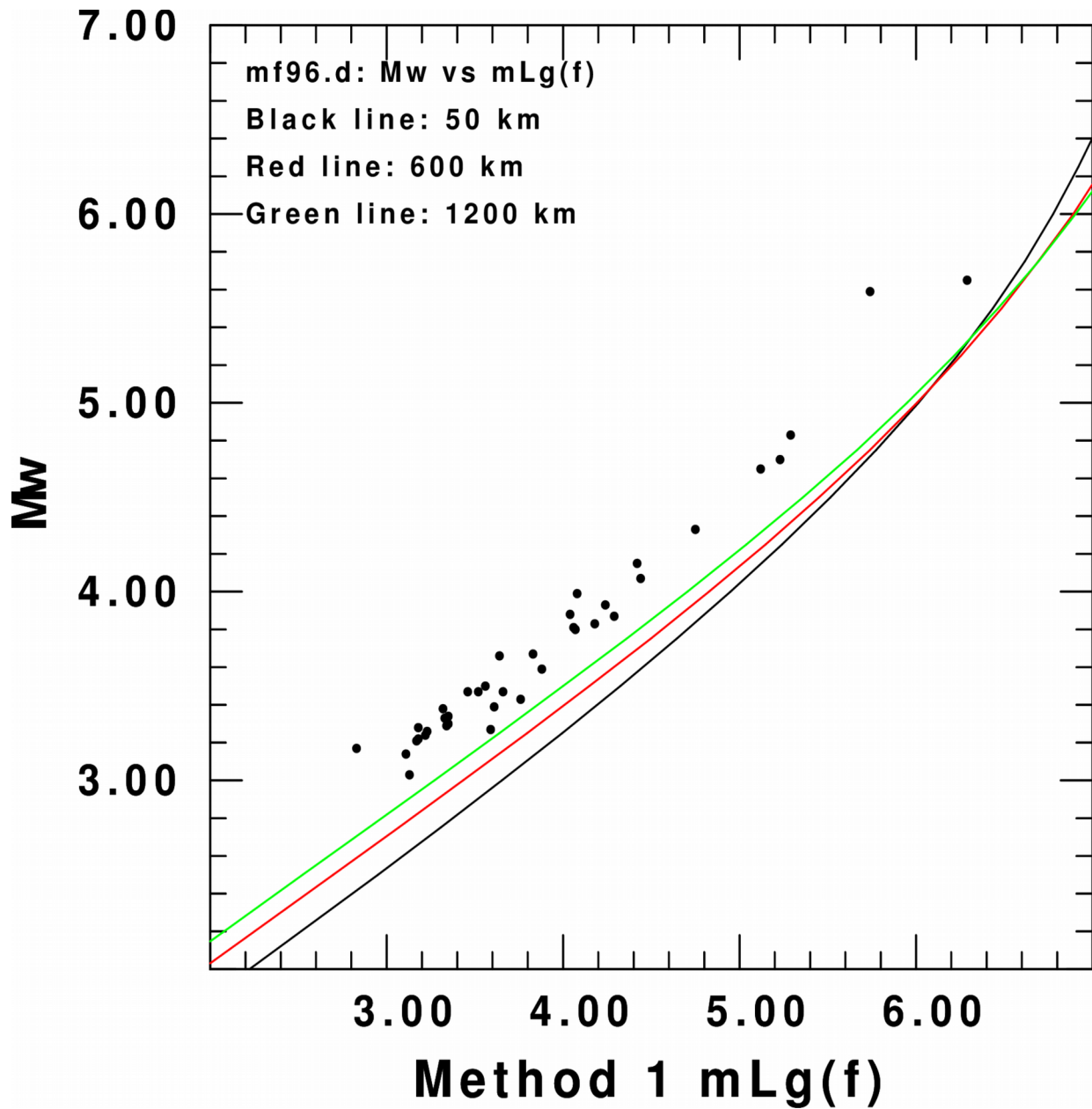


Figure 4.5. The Method 1 $m_{Lg}(f)$ data points lie over the $m_{Lg}(f)$ versus M_w relationship derived from the modified Frankel hard-rock model. The green, red, and black curves give the relationship between $m_{Lg}(f)$ and M_w for different constant epicentral distances. The model uses the instrument-corrected maximum zero-to-peak amplitude, while the Method 1 $m_{Lg}(f)$ points use half the instrument-corrected third-largest peak-to-peak amplitude.

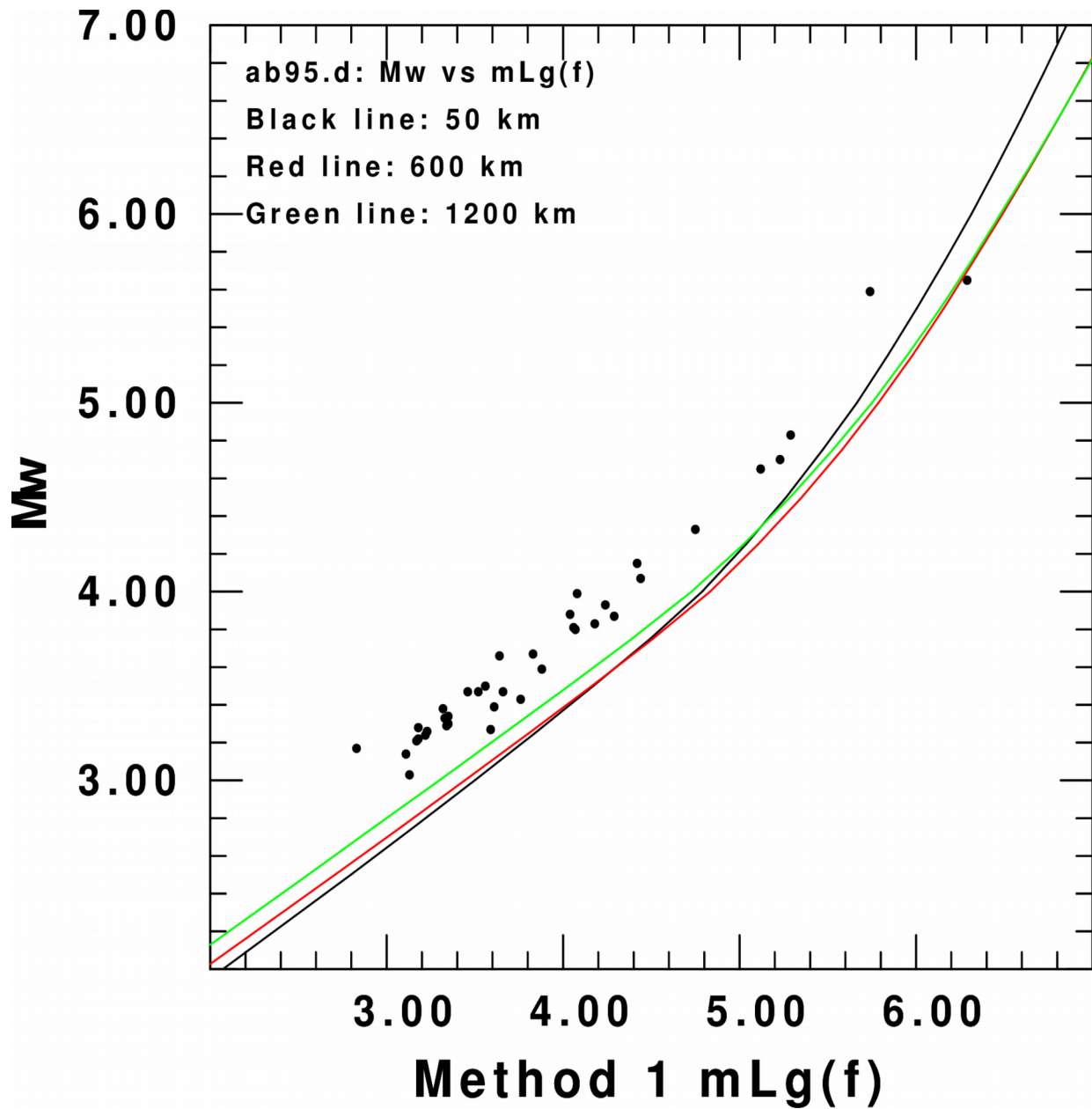


Figure 4.6. The Method 1 $m_{Lg}(f)$ data points lie over the $m_{Lg}(f)$ versus M_w relationship derived from the Atkinson-Boore model. The green, red, and black curves give the relationships between $m_{Lg}(f)$ and M_w for different constant epicentral distances. The model uses the instrument-corrected maximum zero-to-peak amplitude, while the Method 1 $m_{Lg}(f)$ points use half the instrument-corrected third-largest peak-to-peak amplitude.

Figures 4.1–4.3. First, the distance effect is less for smaller magnitudes; the difference in magnitude can be up to 0.2 magnitudes units depending on the $m_{Lg}(f)$ observed at a distance, which is compatible with the empirical offset given in Equation (2.11). Second, there is an $m_{Lg}(f)$, between about 5.0 and 6.0, at which an $m_{Lg}(f)$ observed at 50 km predicts a larger M_w than the same $m_{Lg}(f)$ observed at 1200 km.

These two features suggest that computing a composite $m_{Lg}(f)$ using observations at various distances for smaller events is not as problematic as for m_{bLg} . A further implication is that predicting an M_w for larger $m_{Lg}(f)$ is more prone to error, because a small error in $m_{Lg}(f)$ corresponds to a large error in M_w . Finally, other than the obvious bias between predicted and observed $m_{Lg}(f)$, this exercise shows a great stability in the relation to M_w : for small magnitudes, $M_w \sim (2/3)m_{Lg}(f)$ and for larger magnitudes $M_w \sim (3/2)m_{Lg}(f)$

4.6 Modeling a modified m_{bLg} versus M_w

Figures 4.7–4.9 are similar to Figures 4.1–4.3 except that the Method 1 m_{bLg} data points in Figures 4.7–4.9 use half the instrument-corrected maximum peak-to-peak amplitude rather than the instrument-corrected third-largest peak-to-peak amplitude. The modified Method 1 $(m_{bLg})_{peak}$ is in better agreement with the models than the regular Method 1 m_{bLg} . The better agreement suggests that m_{bLg} can be simulated using random vibration theory if a correction factor is applied to convert from instrument-corrected maximum zero-to-peak amplitude to half the instrument-corrected third-largest peak-to-peak amplitude. Thus, the simulations can be used to learn more about the expected

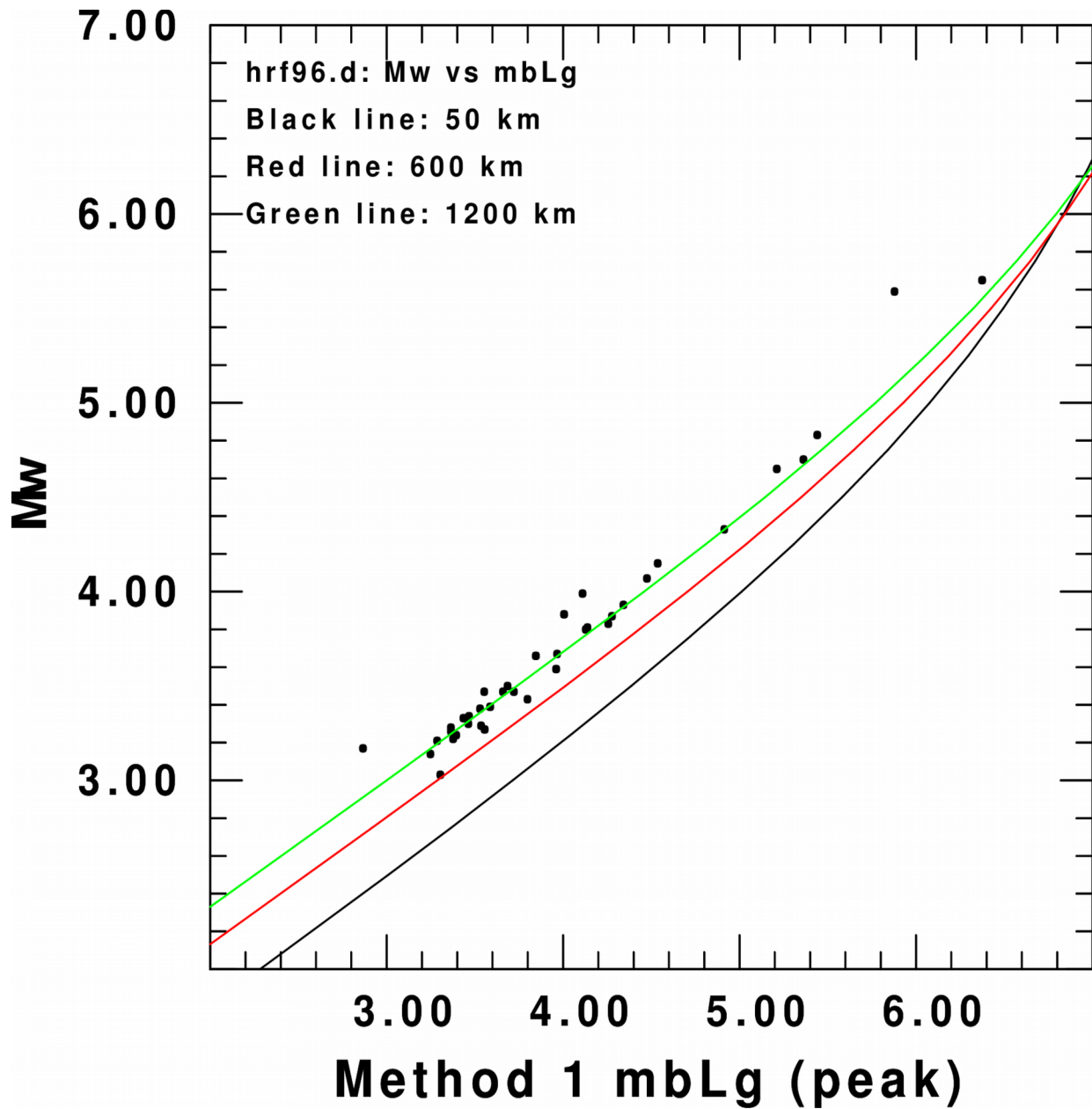


Figure 4.7. The Method 1 m_{bLg} data points lie over the m_{bLg} versus M_w relationship derived from the Frankel hard-rock model. The green, red, and black curves give the relationships between m_{bLg} and M_w for different constant epicentral distances. The model uses the instrument-corrected maximum zero-to-peak amplitude, while the Method 1 m_{bLg} points use half the instrument-corrected maximum peak-to-peak amplitude.

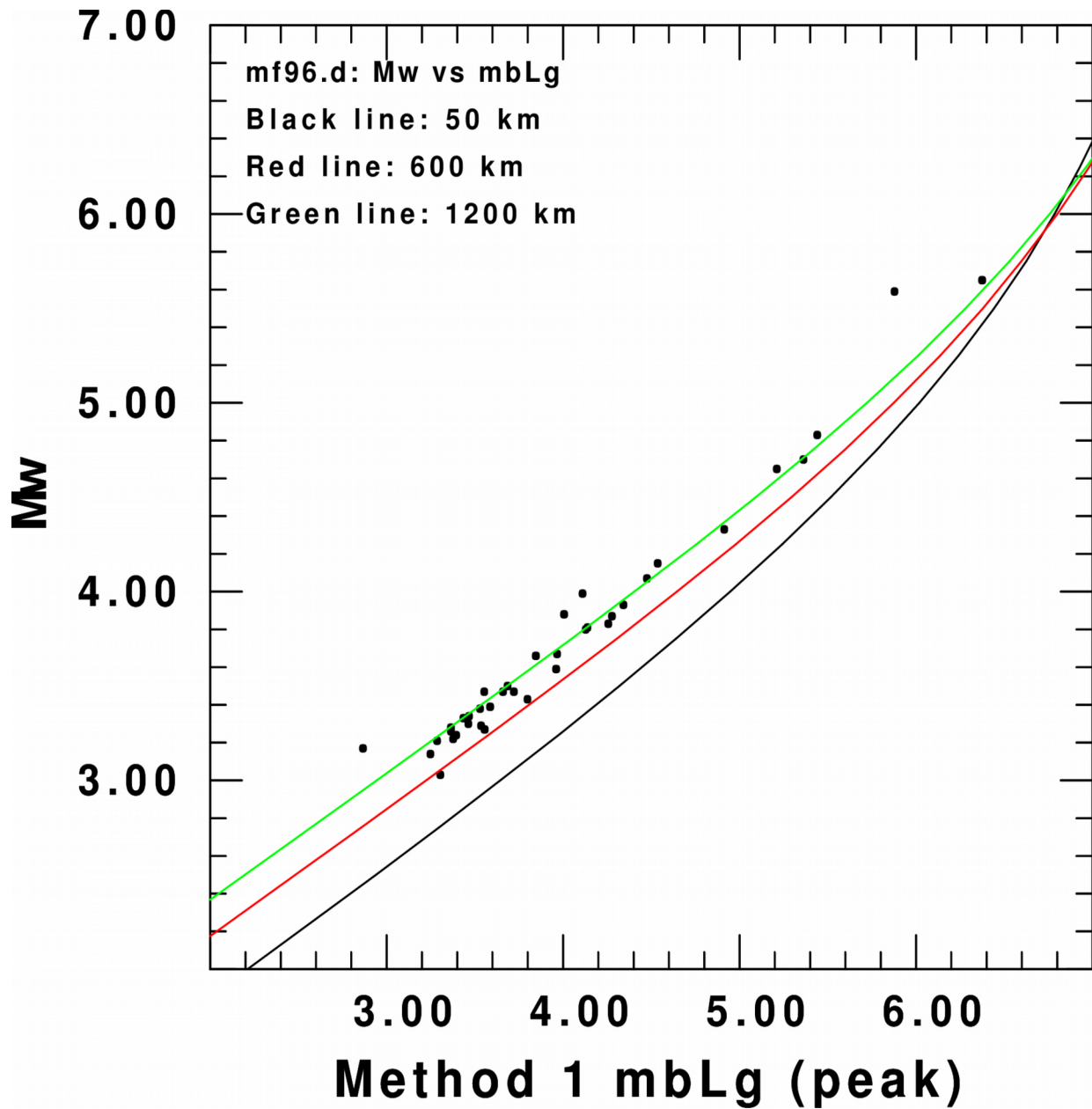


Figure 4.8. The Method 1 m_{bLg} data points lie over the m_{bLg} versus M_w relationship derived from the modified Frankel hard-rock model. The green, red, and black curves give the relationships between m_{bLg} and M_w for different constant epicentral distances. The model uses the instrument-corrected maximum peak-to-peak amplitude, while the Method 1 m_{bLg} points use half the instrument-corrected maximum peak-to-peak amplitude.

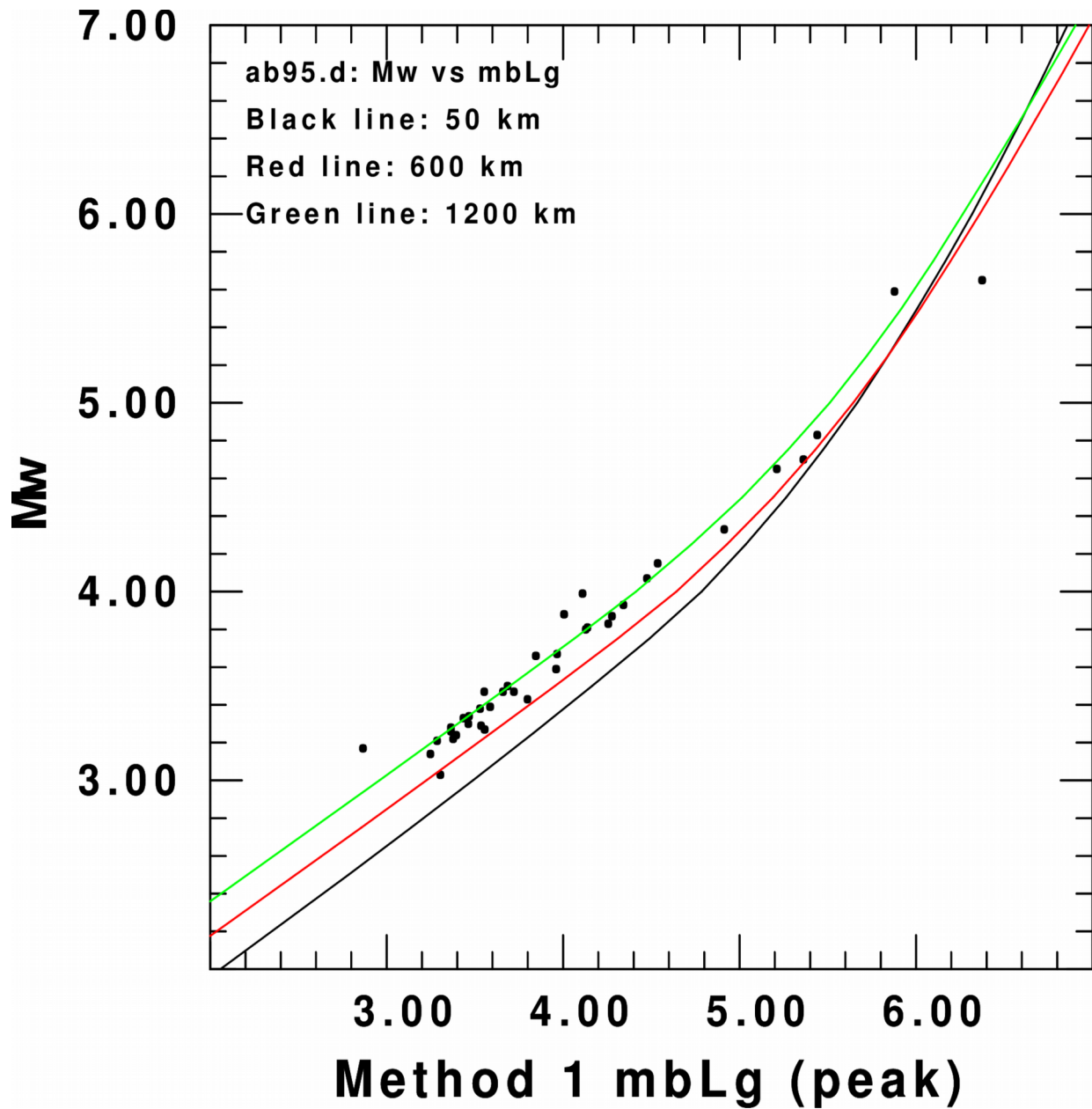


Figure 4.9. The Method 1 m_{bLg} data points lie over the m_{bLg} versus M_w relationship derived from the Atkinson-Boore model. The green, red, and black curves give the relationships between m_{bLg} and M_w for different constant epicentral distances. The model uses the instrument-corrected maximum zero-to-peak amplitude, while the Method 1 m_{bLg} points use half the instrument-corrected maximum peak-to-peak amplitude.

relation between M_w and m_{bLg} , which was used to constrain the regressions leading to Equations (2.6), (2.7), (2.8), and (2.9).

4.7 Modeling a modified $m_{Lg}(f)$ versus M_w

Figures 4.10–4.12 are similar to Figures 4.4–4.6 except that the Method 1 $m_{Lg}(f)$ data points in Figures 4.10–4.12 use half the instrument-corrected maximum peak-to-peak amplitude. The modified Method 1 $m_{Lg}(f)$ is in better agreement with the models than the regular Method 1 $m_{Lg}(f)$. The better agreement suggests that $m_{Lg}(f)$ can be simulated using random vibration theory if a correction factor is applied to convert from instrument-corrected maximum zero-to-peak amplitude to half the instrument-corrected third-largest peak-to-peak amplitude.

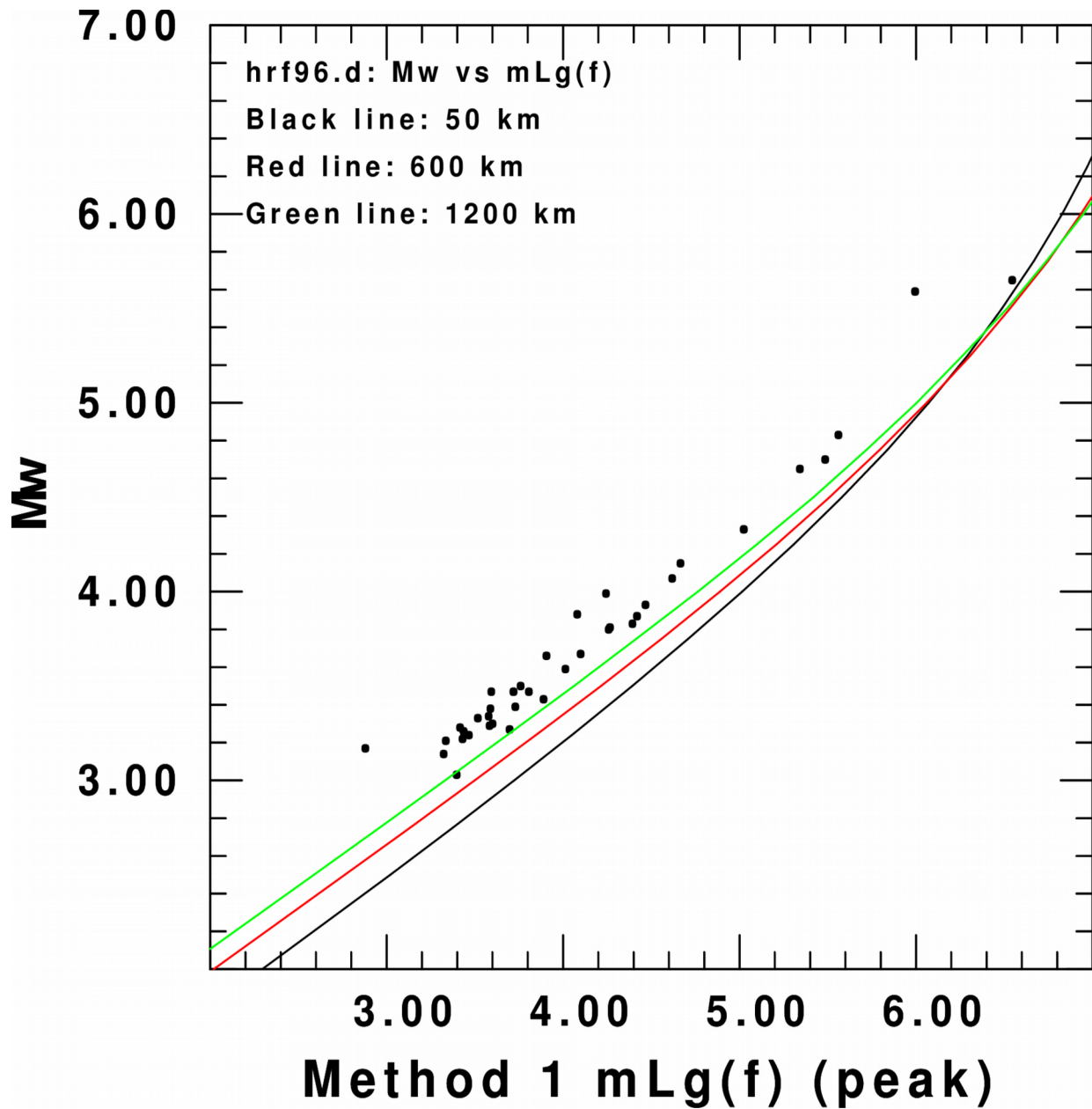


Figure 4.10. The Method 1 $m_{Lg}(f)$ data points lie over the $m_{Lg}(f)$ versus M_w relationship derived from the modified Frankel hard-rock model. The green, red, and black curves give the relationships between $m_{Lg}(f)$ and M_w for different constant epicentral distances. The model uses the instrument-corrected maximum zero-to-peak amplitude, while the Method 1 $m_{Lg}(f)$ points use half the instrument-corrected maximum peak-to-peak amplitude.

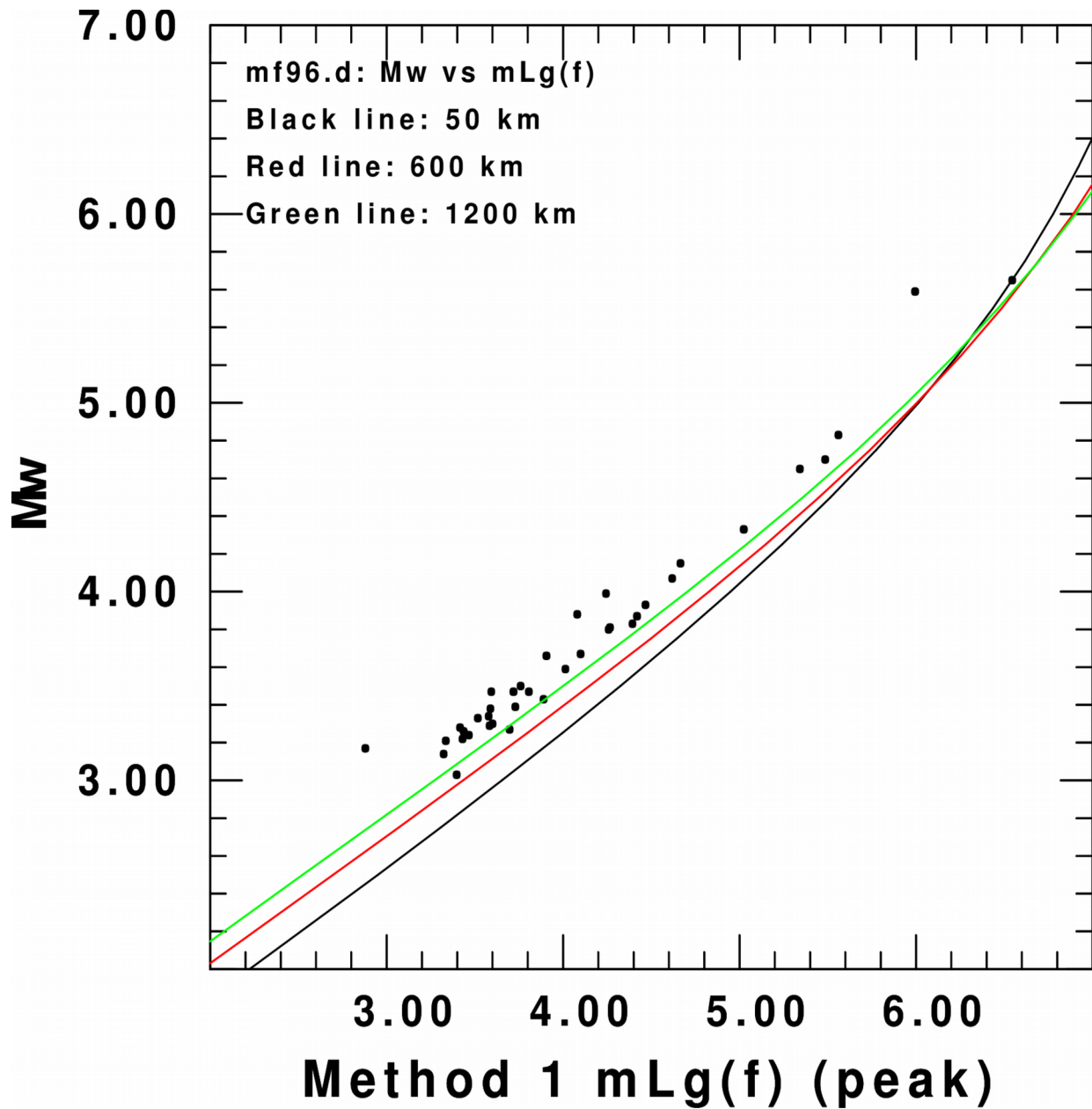


Figure 4.11. The Method 1 $m_{Lg}(f)$ data points lie over the $m_{Lg}(f)$ versus M_w relationship derived from the Frankel hard-rock model. The green, red, and black curves give the relationships between $m_{Lg}(f)$ and M_w for different constant epicentral distances. The model uses the instrument-corrected maximum zero-to-peak amplitude, and the Method 1 $m_{Lg}(f)$ points use half the instrument-corrected maximum peak-to-peak amplitude.

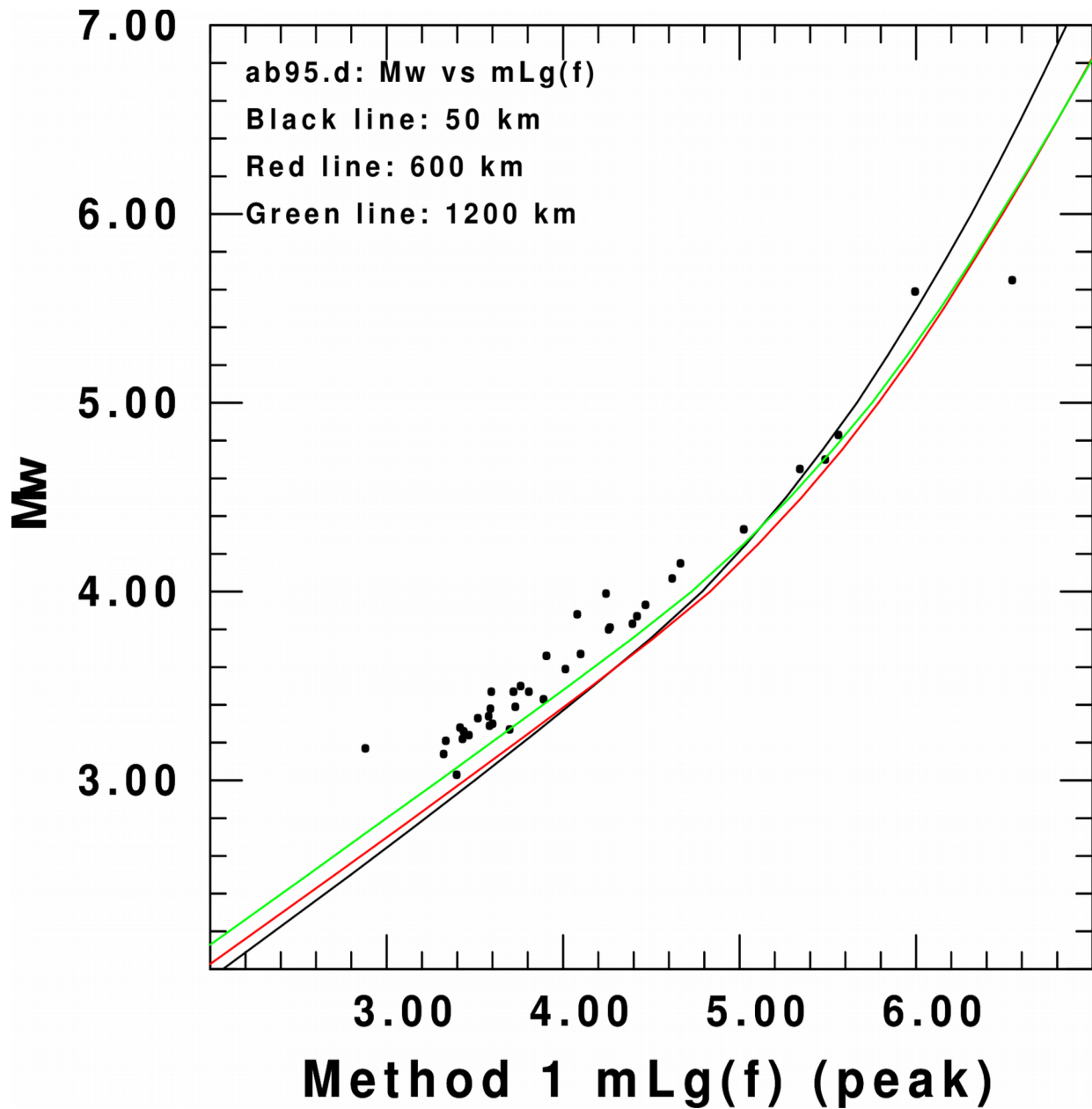


Figure 4.12. The Method 1 $m_{Lg}(f)$ data points lie over the $m_{Lg}(f)$ versus M_w relationship derived from the Atkinson-Boore model. The green, red, and black curves give the relationships between $m_{Lg}(f)$ and M_w for different constant epicentral distances. The model uses the instrument-corrected maximum zero-to-peak amplitude, while the Method 1 $m_{Lg}(f)$ points use half the instrument-corrected maximum peak-to-peak amplitude.

CHAPTER 5: An Examination of γ

5.1 Model for Ground Motion

For a spherical Earth with a point source, the peak amplitudes of Lg waves for the Airy phase can be modeled as

$$A(\Delta) = C_1 \Delta^{-1/3} (\sin \Delta)^{-1/2} e^{-\gamma \Delta}, \text{ where} \quad (5.1)$$

C_1 is a constant, Δ is the distance in degrees, and γ is the coefficient of anelastic attenuation (Ewing *et al.*, 1957). The relation between γ and the quality factor Q is

$$\gamma = \frac{\pi f}{c_Q Q(f)}, \text{ where} \quad (5.2)$$

f is the frequency in Hz and c_Q is the group velocity used to determine Q in km/s (Nuttli, 1973).

When the Earth can be modeled as being flat, as is appropriate for regional distances, the model for peak amplitudes simplifies. The simplified model for peak vertical ground amplitude on a short-period instrument as a function of epicentral distance at regional distances is

$$A(r) = C_2 r^{-\zeta} e^{-\gamma r}, \text{ where} \quad (5.3)$$

A is peak ground displacement, C_2 is a constant related to the source, r is epicentral distance in km, ζ is the geometrical spreading factor, and γ is the coefficient of anelastic attenuation in km^{-1} (Yang, 2002). For the Airy phase, an appropriate value for ζ is 5/6, and the model uses that value. Because m_{bLg} and $m_{Lg}(f)$ use half the third-largest peak-to-peak amplitude, those are the values that are modeled.

Linear least-squares regression derives values of γ for the 10 earthquakes with the most observations. For those 10 earthquakes, the Method 1 amplitudes that passed the earlier signal-to-noise test are used in the regression. In order to linearize the model, the natural logarithm of each side is taken and the terms are rearranged.

The resulting form is

$$Y' = B + (-\gamma)r, \text{ where} \quad (5.4)$$

$$Y' = \ln(A) + 0.8333\ln(r) \text{ and} \\ B = \ln(C_1).$$

5.2 Results and Discussion

Table 5.1 gives the M_w , Method 1 m_{bLg} , Method 1 $m_{Lg}(f)$, and the associated γ values for the 10 earthquakes with the most observations. Two different γ values are computed for each earthquake, one based on data from distances between 50 and 1200 km and the other based on data from all distances.

Table 5.1 shows that half of the listed earthquakes have negative γ values between 50 and 1200 km. Because the linear least-squares regression cannot simultaneously determine the best fits for geometrical spreading and γ , an assumed geometrical spreading value is required for the γ determination. Thus, one interpretation of a negative γ value is that the assumed geometrical spreading in the model is too large, because amplitudes typically decrease with distance and both geometrical spreading and anelastic attenuation usually contribute to the observed decrease.

Another interpretation of a negative γ is that over the given distance range the

Table 5.1. Earthquake dates, M_w , Method 1 m_{bLg} , Method 1 $m_{Lg}(f)$, and associated coefficients of anelastic attenuation. The last 2 columns gives coefficients of anelastic attenuation for different distance ranges.

Date	M_w	m_{bLg}	$m_{Lg}(f)$	γ (km^{-1}) 50-1200 km	γ (km^{-1}) All distances
15 January 2010	3.81	4.02	4.06	-0.00061	0.00008
27 February 2010	4.15	4.41	4.42	0.00023	0.00085
13 October 2010	4.33	4.74	4.75	0.00026	0.00099
20 November 2010	3.87	4.15	4.29	0.00030	0.00057
24 November 2010	3.93	4.22	4.24	-0.00020	0.00040
18 February 2011	4.07	4.35	4.44	-0.00014	0.00009
28 February 2011	4.65	5.08	5.12	-0.00010	0.00084
5 November 2011	4.70	5.23	5.23	0.00007	0.00130
6 November 2011	5.59	5.74	5.74	0.00031	0.00150
8 November 2011	4.83	5.27	5.29	-0.00042	0.00118

anelastic attenuation term in the amplitude model in fact contributes to an increase in amplitude rather than a decrease. For these 5 earthquakes, there are reasons to believe that the assumed geometrical spreading is sufficient and that the apparent negative γ values are correct. Since the earthquakes occurred in Oklahoma and Arkansas, stations located along southern propagational paths near the Gulf Coast may have higher amplitudes because of amplification through the increasing thickness of sediments. The γ values in Table 5.1 are averages of all appropriate amplitudes from all propagational paths, so there is the possibility that stations in southern propagational paths contribute to negative γ values while propagational paths in all other directions exhibit the usual decrease in amplitude with distance and thus contribute to positive γ values.

Table 5.1 also indicates that, when all appropriate amplitudes at all distances are used, the γ values are positive. Even after accounting for all distances, though, the γ values range from 0.0008 to 0.00150 km⁻¹. The calculated values for γ for 50 to 1200 km and for all distances suggest that a single-valued γ for the central and eastern United States may not be appropriate.

Figures 5.1–5.10 show the regression analyses for the 10 earthquakes with the most observations. One prominent feature of several of the figures is the bifurcation of the dependent variable as distance increases. Figure 5.3 may show a bifurcation of $\ln(A) + (5/6)\ln(r)$ beyond 1600 km. While the possible upper branch rises slowly with distance relative to the regression line, the possible lower branch decreases rapidly with distance relative to the regression line. The propagational paths of the waves, especially

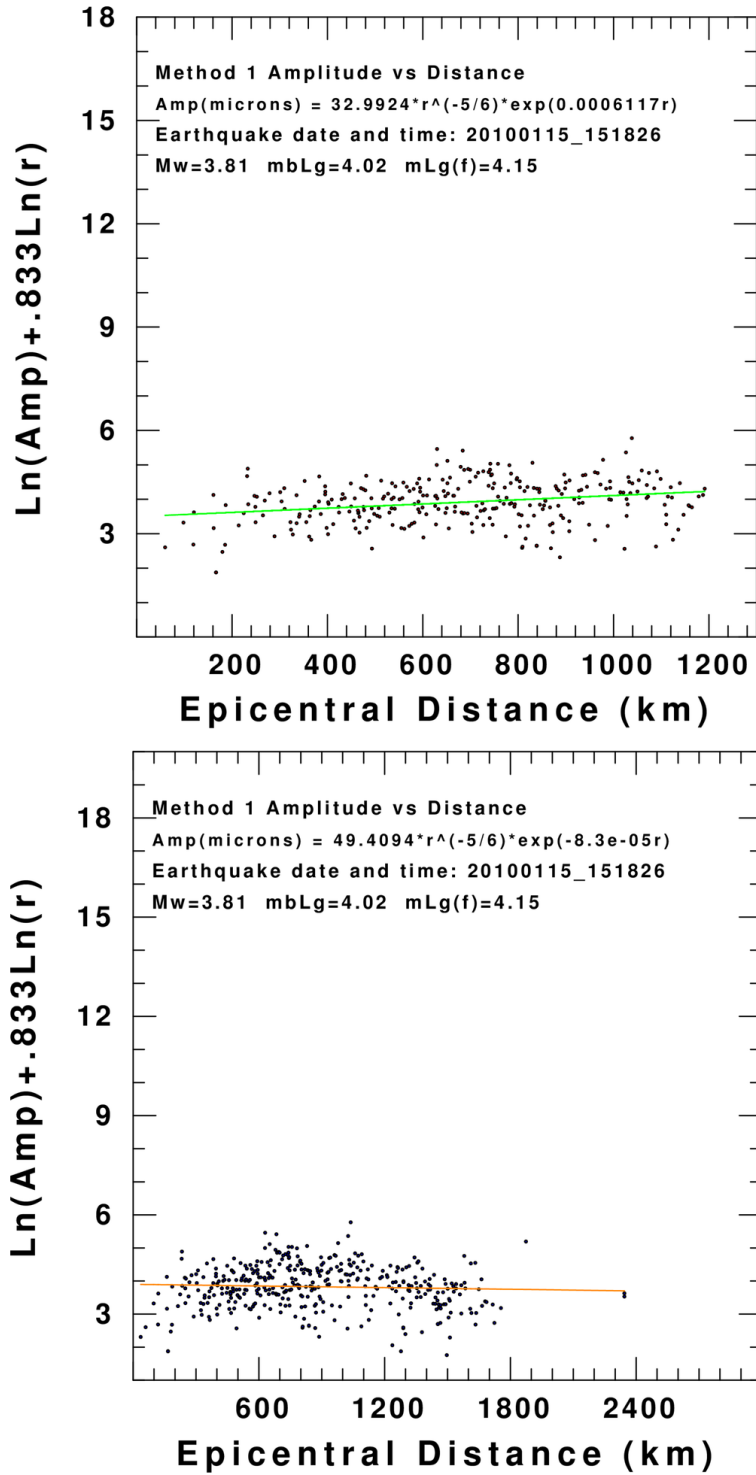


Figure 5.1. The linear least-squares regression analysis is shown for the 15 January 2010 earthquake. Two distance ranges, 50-1200 km (*top*) and all distances (*bottom*), are illustrated, and the accompanying M_w , Method 1 m_{bLg} , and Method 1 $m_{Lg}(f)$ are given.

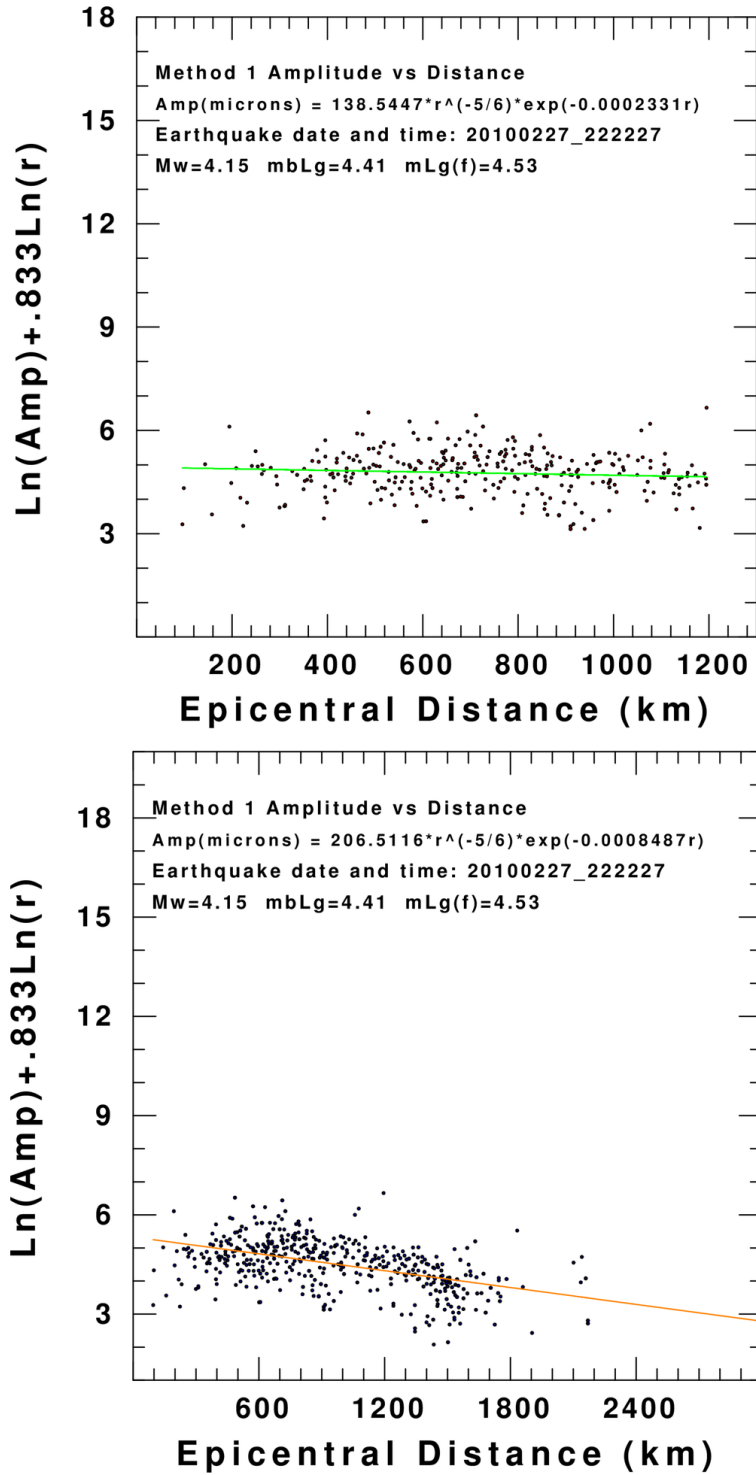


Figure 5.2. The linear least-squares regression analysis is shown for the 27 February 2010 earthquake. Two distance ranges, 50-1200 km (*top*) and all distances (*bottom*), are illustrated, and the accompanying M_w , Method 1 m_{bLg} , and Method 1 $m_{Lg}(f)$ are given.

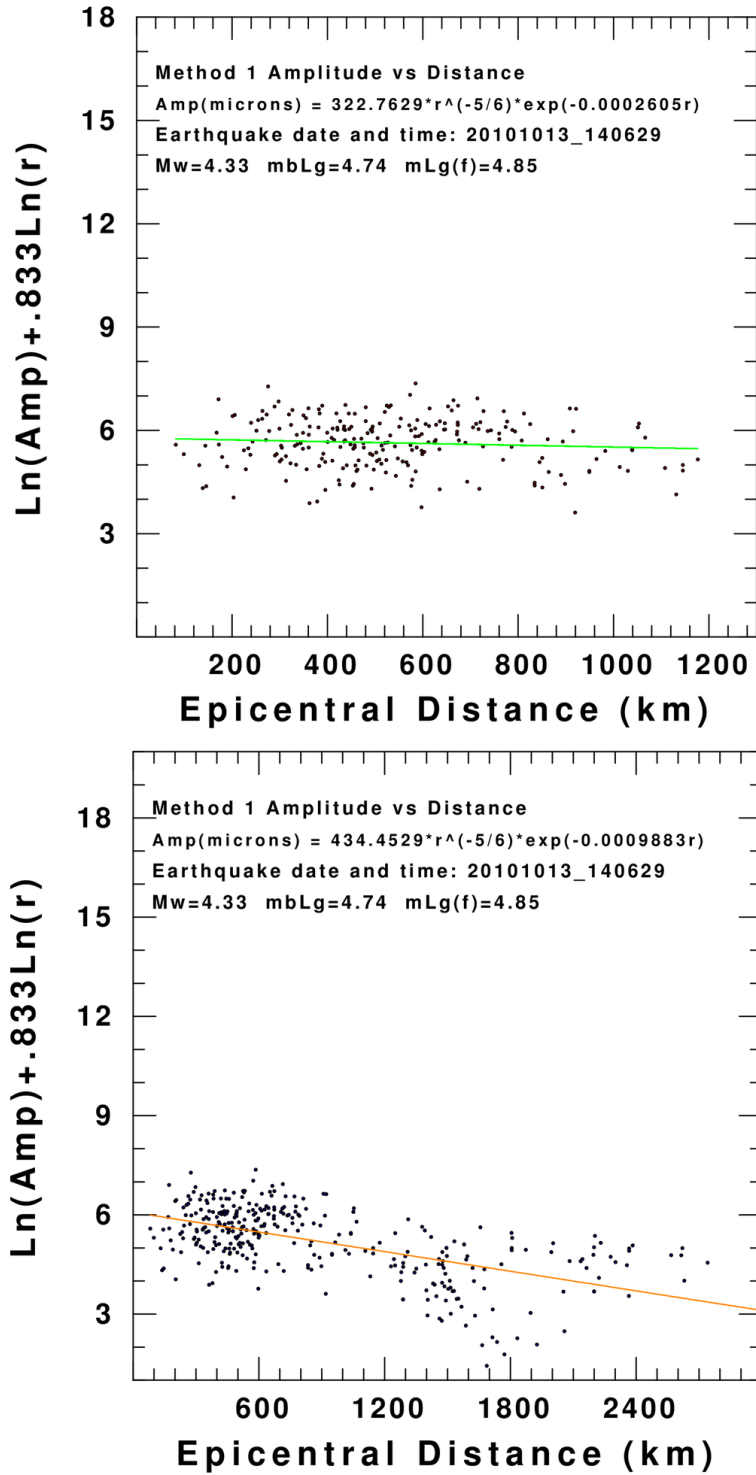


Figure 5.3. The linear least-squares regression analysis is shown for the 13 October 2010 earthquake. Two distance ranges, 50-1200 km (*top*) and all distances (*bottom*), are illustrated, and the accompanying M_w , Method 1 m_{bLg} , and Method 1 $m_{Lg}(f)$ are given.

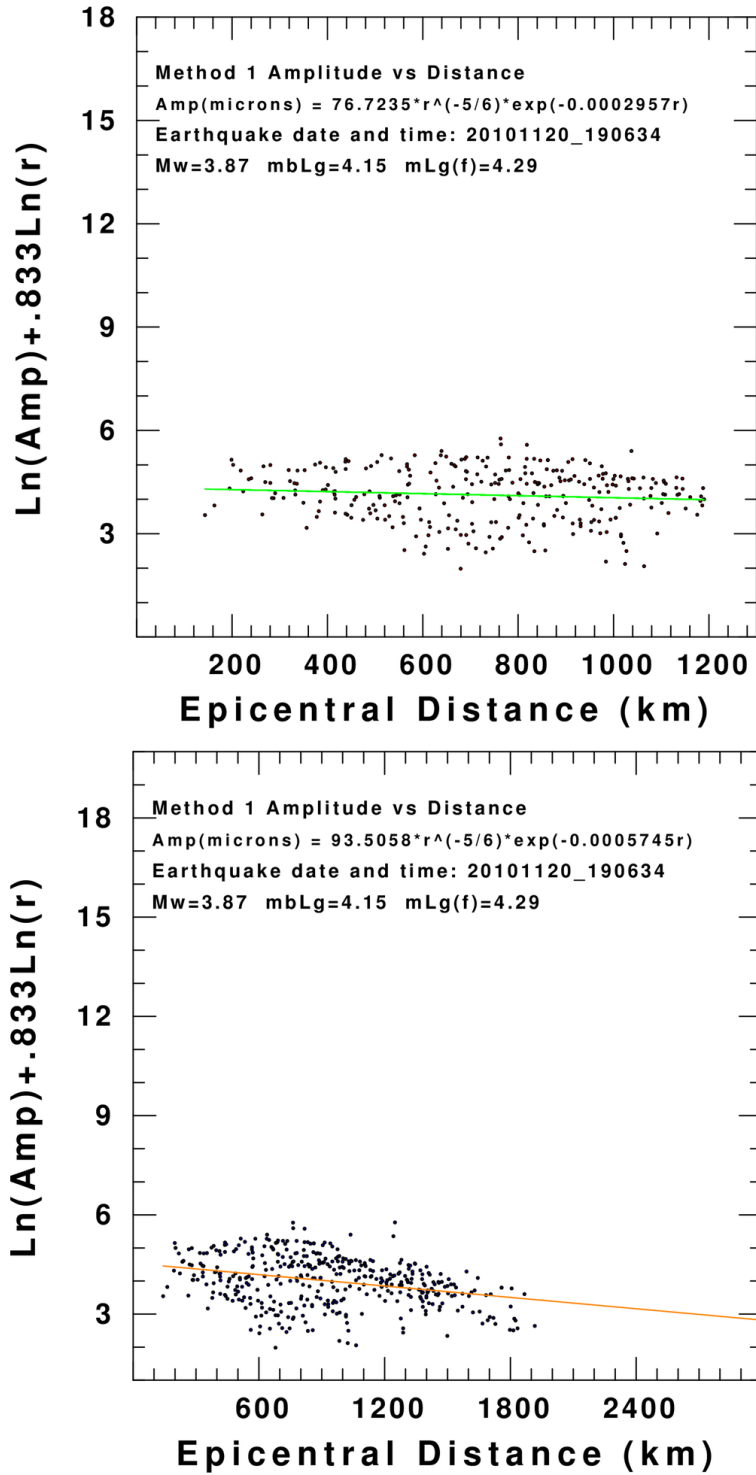


Figure 5.4. The linear least-squares regression analysis is shown for the 20 November 2010 earthquake. Two distance ranges, 50-1200 km (*top*) and all distances (*bottom*), are illustrated, and the accompanying M_w , Method 1 m_{bLg} , and Method 1 $m_{Lg}(f)$ are given.

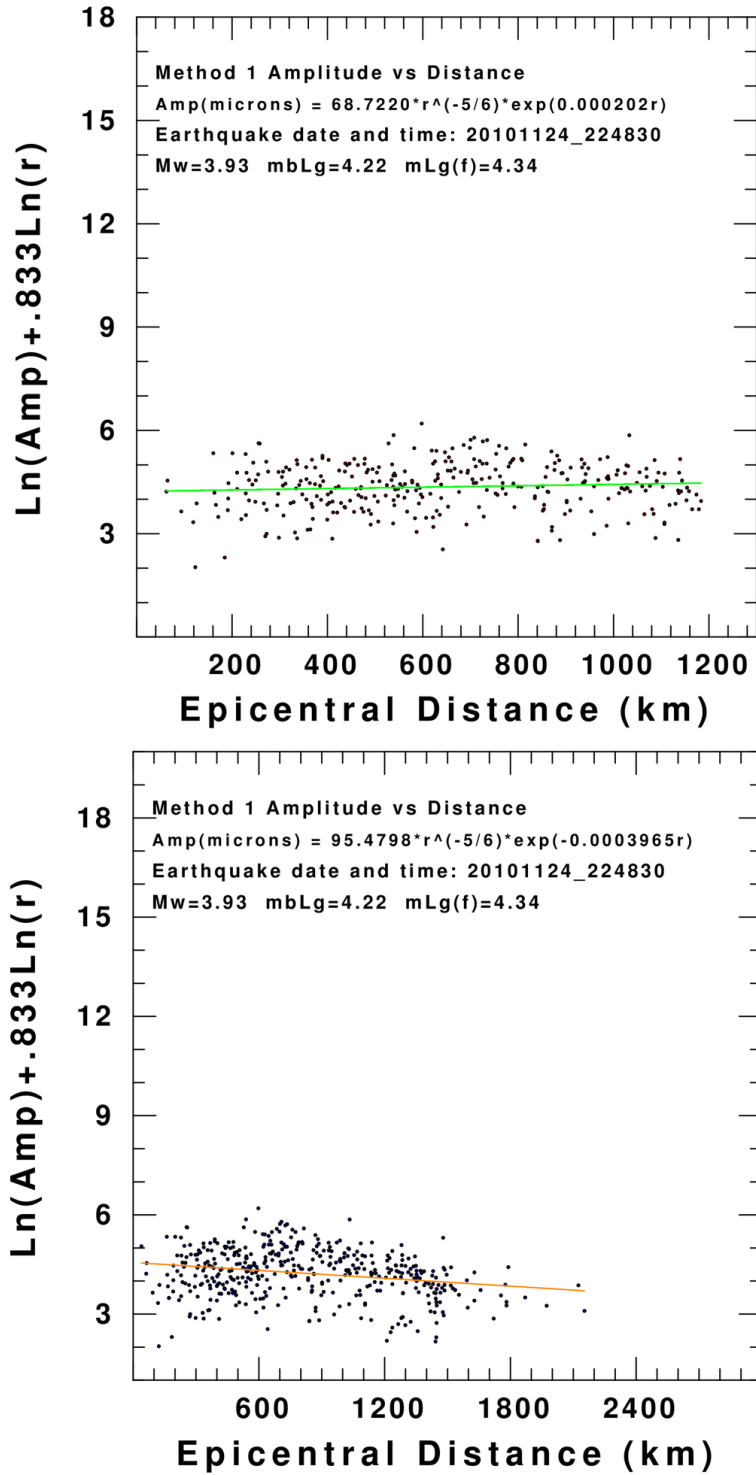


Figure 5.5. The linear least-squares regression analysis is shown for the 24 November 2010 earthquake. Two distance ranges, 50-1200 km (*top*) and all distances (*bottom*), are illustrated, and the accompanying M_w , Method 1 m_{bL_g} , and Method 1 $m_{L_g}(f)$ are given.

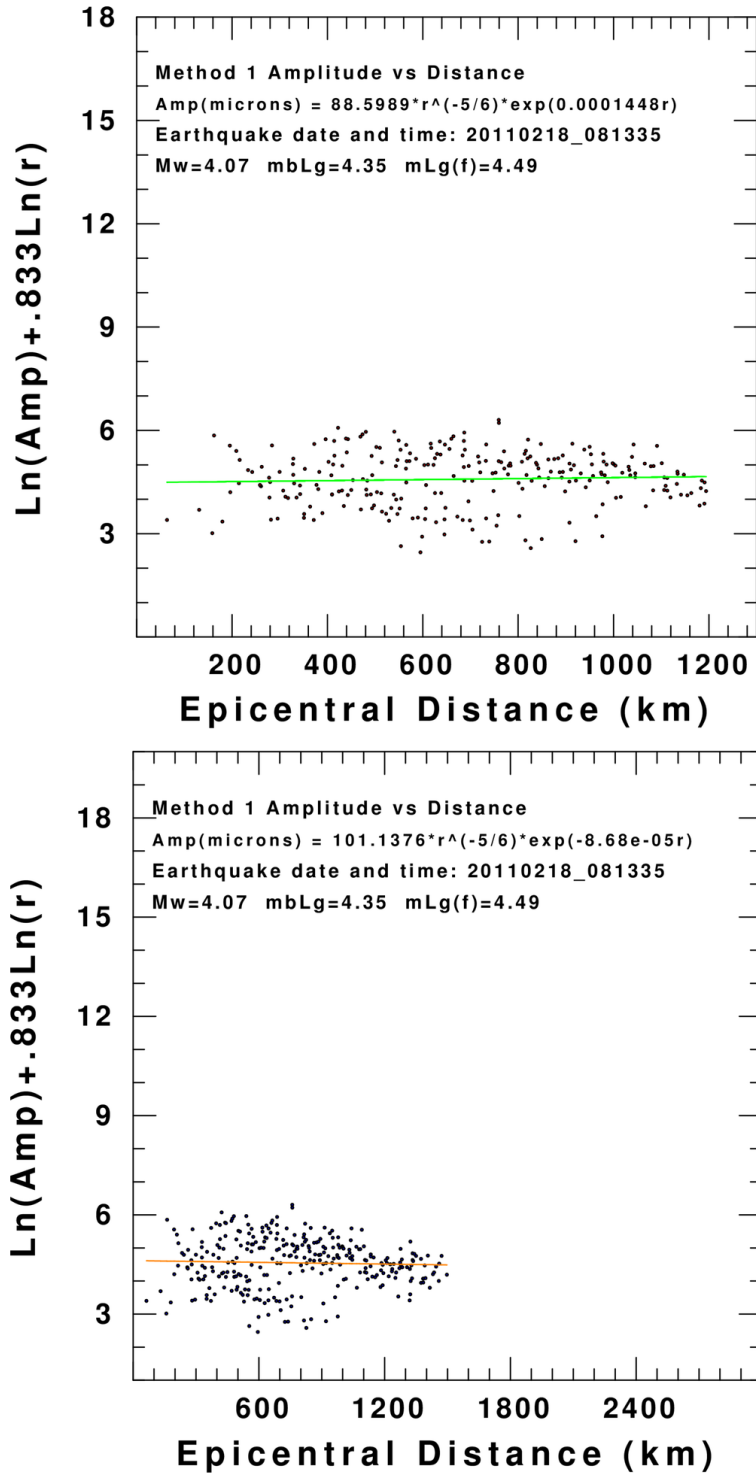


Figure 5.6. The linear least-squares regression analysis is shown for the 18 February 2011 earthquake. Two distance ranges, 50-1200 km (*top*) and all distances (*bottom*), are illustrated, and the accompanying M_w , Method 1 m_{bLg} , and Method 1 $m_{Lg}(f)$ are given.

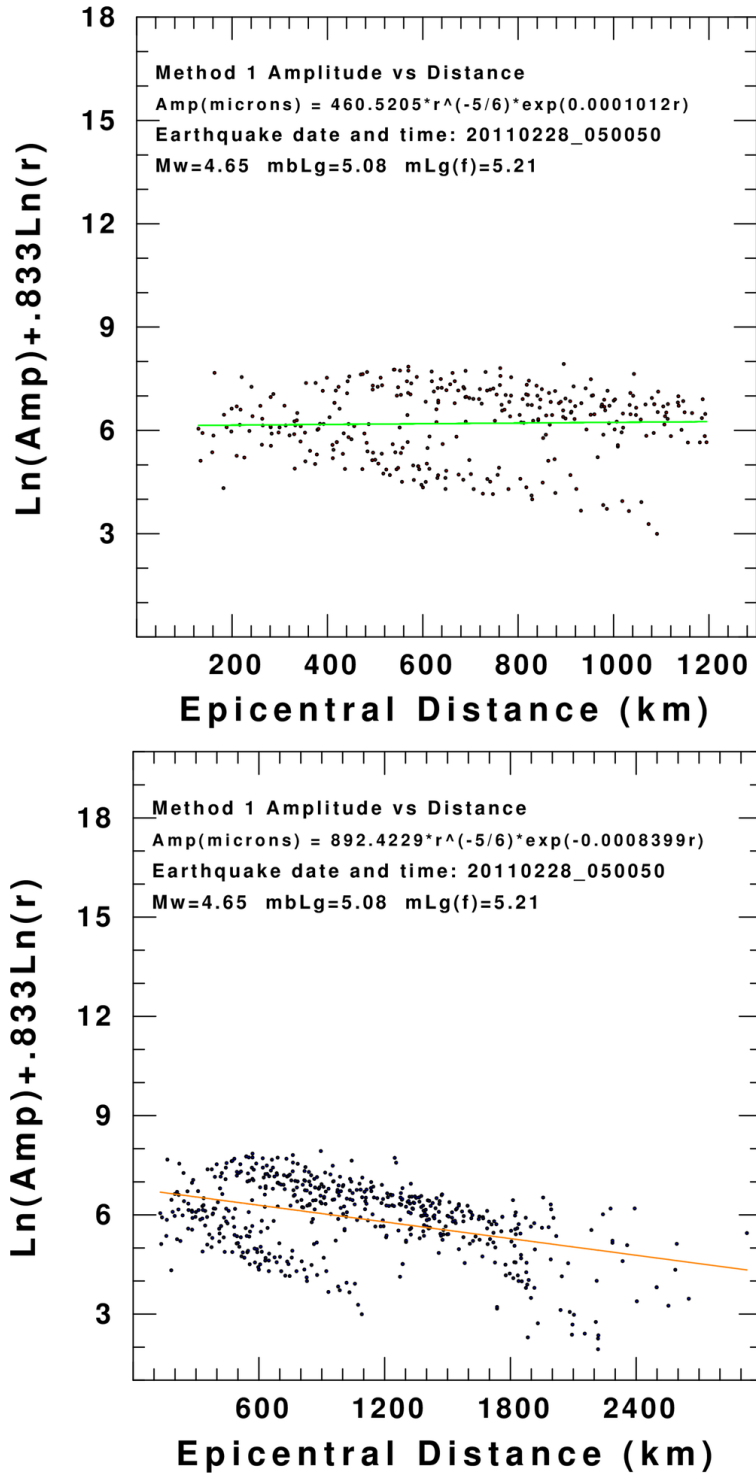


Figure 5.7. The linear least-squares regression analysis is shown for the 28 February 2011 earthquake. Two distance ranges, 50-1200 km (*top*) and all distances (*bottom*), are illustrated, and the accompanying M_w , Method 1 m_{bLg} , and Method 1 $m_{Lg}(f)$ are given.

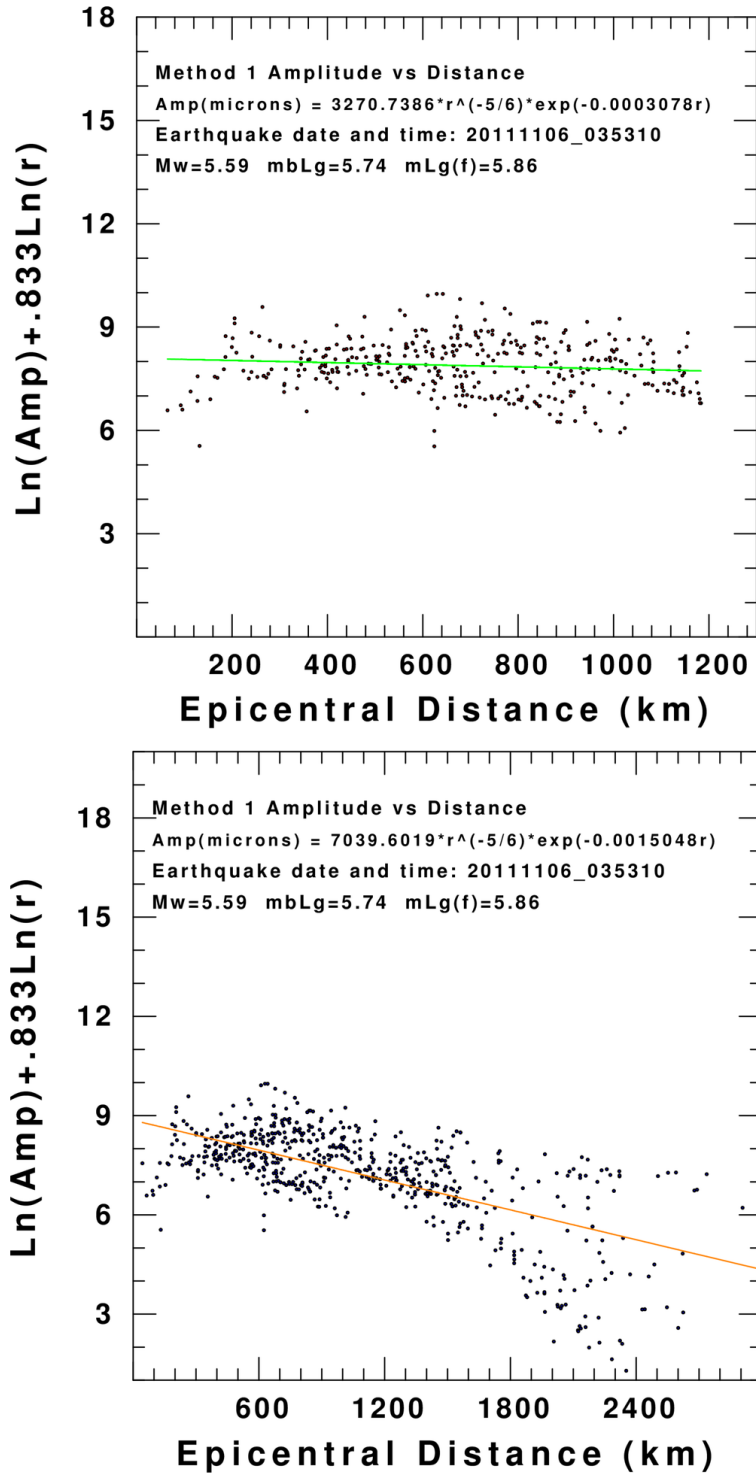


Figure 5.8. The linear least-squares regression analysis is shown for the 6 November 2011 earthquake. Two distance ranges, 50-1200 km (*top*) and all distances (*bottom*), are illustrated, and the accompanying M_w , Method 1 m_{bLg} , and Method 1 $m_{Lg}(f)$ are given.

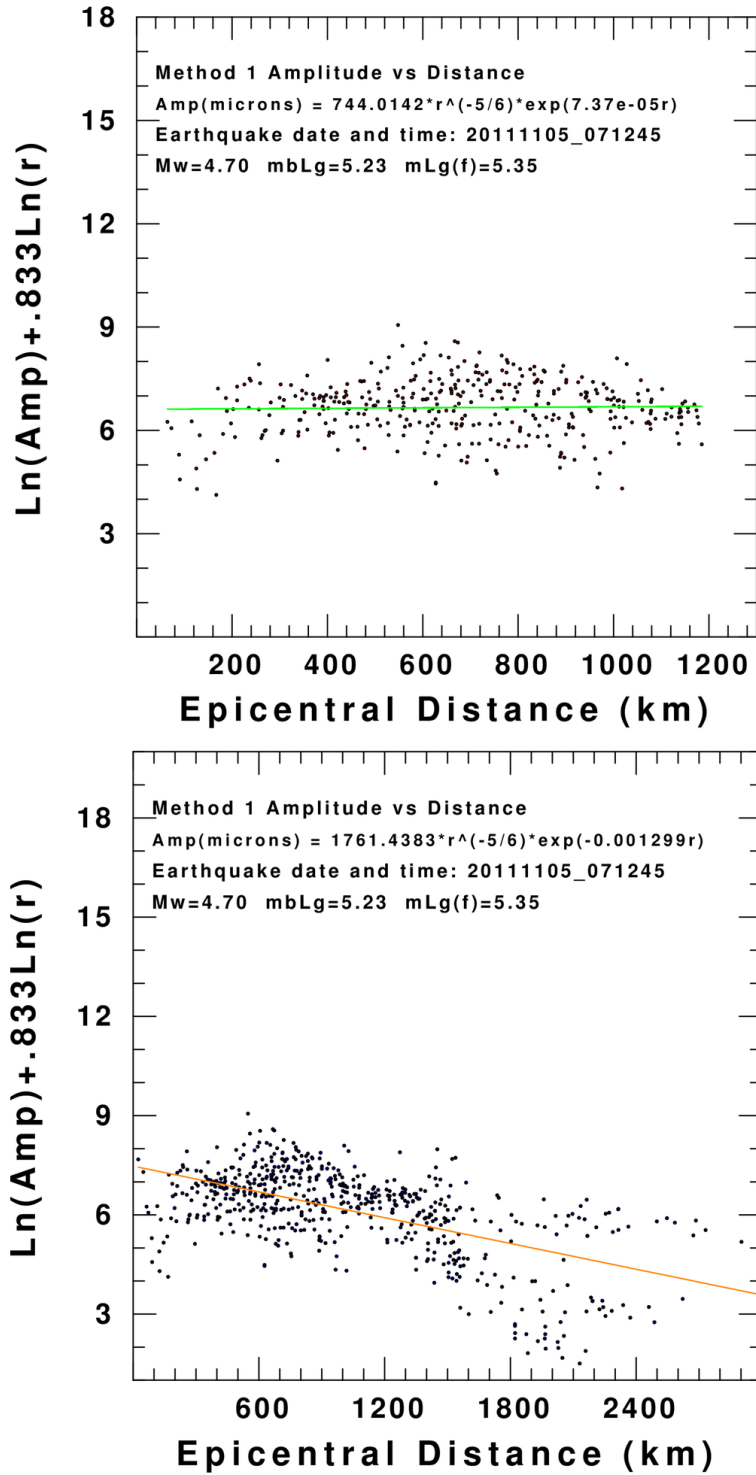


Figure 5.9. The linear least-squares regression analysis is shown for the 5 November 2011 earthquake. Two distance ranges, 50-1200 km (*top*) and all distances (*bottom*), are illustrated, and the accompanying M_w , Method 1 m_{bLg} , and Method 1 $m_{Lg}(f)$ are given.

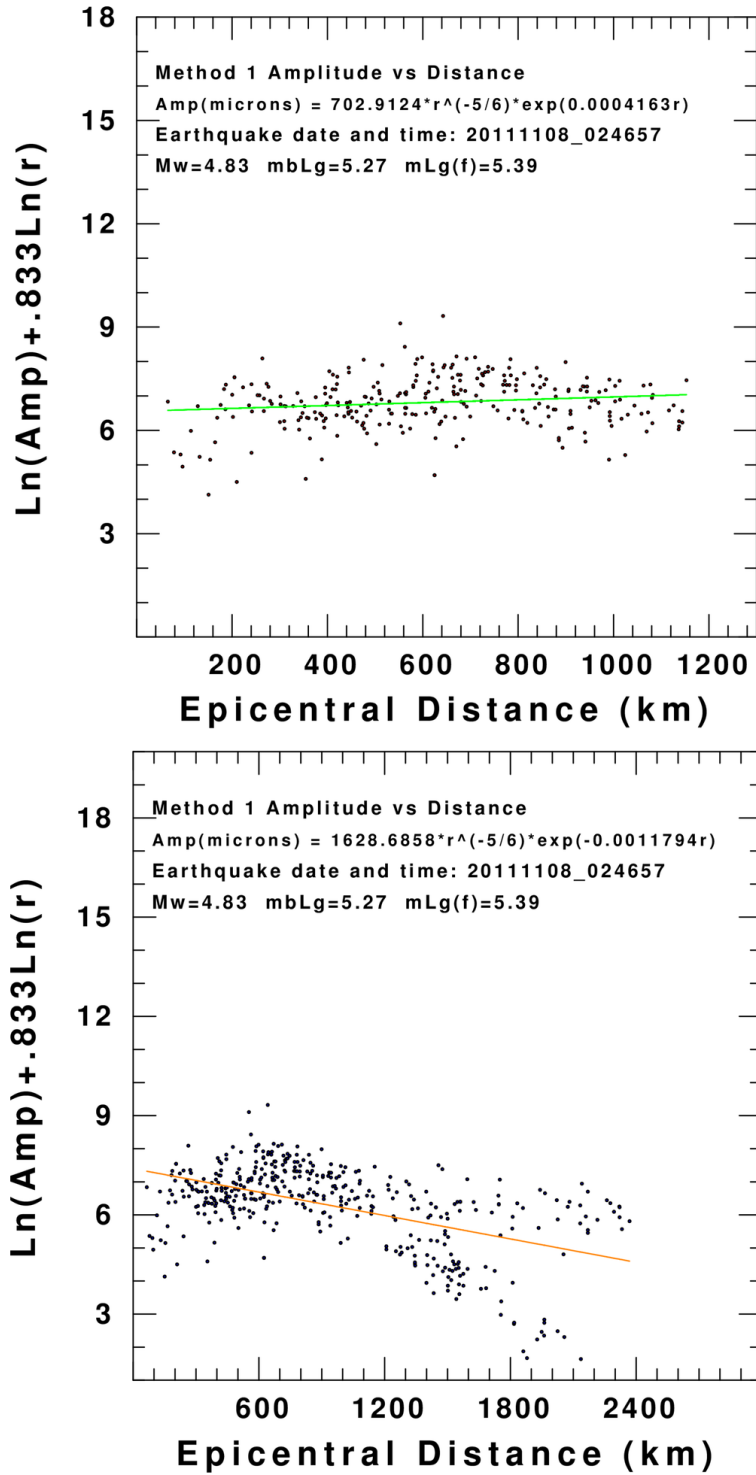


Figure 5.10. The linear least-squares regression analysis is shown for the 8 November 2011 earthquake. Two distance ranges, 50-1200 km (*top*) and all distances (*bottom*), are illustrated, and the accompanying M_w , Method 1 m_{bLg} , and Method 1 $m_{Lg}(f)$ are given.

to the south, and any particular site effects may explain the possible bifurcation. Figures 5.8–5.10 show distinctive spreading of $\ln(A) + (5/6).8333\ln(r)$ beyond 1500 km. For these earthquakes, the propagational paths surely affect the bifurcation. Figure 5.7 for an Arkansas earthquake is the most interesting figure, because there are two instances of bifurcation. One bifurcation seems to occur from 600 to 1200 km, and the other bifurcation occurs beyond 1800 km.

Figures 5.1–5.10 corroborate the use of m_{bLg} and $m_{Lg}(f)$ for a limited distance range, but those figures may suggest that the upper limit on epicentral distance could be greater than 1200 km.

CHAPTER 6: Summary and Conclusions

This thesis studies the relationships between m_{bLg} and M_w and between $m_{Lg}(f)$ and M_w by using two different methods for recent United States earthquakes and by modeling the relationships with random vibration theory. Method 1 attempts to replicate the NEIC methodology in its computation of m_{bLg} . Method 2 attempts to estimate the NEIC computations by using a proxy for the frequency of the Lg wave and by employing an empirical relation to obtain an estimate of half the instrument-corrected third-largest peak-to-peak amplitude. Random vibration theory predicts peak motion and the frequency of zero crossings through the computation of various moments in Method 2.

Based on the empirical work from Chapters 2 and 3 and the simulations from Chapter 4, either Equations (2.4)(m_{bLg}) and (2.5)($m_{Lg}(f)$) or Equations (2.6)(bilinear m_{bLg}) and (2.8)(bilinear $m_{Lg}(f)$) can be used to stably predict M_w for m_{bLg} or $m_{Lg}(f)$ equal to or less than 4.5. This predictive ability allows an estimate of M_w for earthquakes for which independent M_w from moment tensor inversion is not possible. For m_{bLg} or $m_{Lg}(f)$ between 4.5 and 5.5, the modeling from Chapter 4 supports a judicious use of the bilinear equations, Equations (2.6) and (2.8), if other estimates of M_w are not possible. For m_{bLg} or $m_{Lg}(f)$ greater than 5.5, the modeling from Chapter 4 cautions against the use of any of the regression equations, because a small error in m_{bLg} or $m_{Lg}(f)$ produces a large error in the M_w estimate.

The empirical work from Chapters 2 and 3 does not support a preference for either m_{bLg} or $m_{Lg}(f)$ as a predictor of M_w , as long as the definitions of the respective

magnitudes are followed closely. In addition, Figure 2.16 suggests that the distance range over which m_{bLg} and $m_{Lg}(f)$ can be calculated is 150–1350 km rather than the approximate 50–1100 km range used by the NEIC. However, if γ is frequency-dependent, as Chapter 5 suggests, then the simulations from Chapter 4 support the use of $m_{Lg}(f)$ over m_{bLg} . The simulations permit an understanding of M_w versus $m_{Lg}(f)$ as a function of earthquake size, without placing nearly as much significance on the distance of the observation as m_{bLg} does.

Modeling relationships between m_{bLg} and M_w and between $m_{Lg}(f)$ and M_w leads to two conclusions. First, m_{bLg} and $m_{Lg}(f)$ averages calculated within certain distance bins may lead to better theoretical relationships and allow better predictions. Second, the use of a correction factor between half the instrument-corrected maximum peak-to-peak amplitude and half the instrument-corrected third-largest amplitude for the computations of m_{bLg} and $m_{Lg}(f)$ may contribute to better modeling and understanding of the Lg magnitudes. Equations (2.10) and (2.11) relate $(m_{bLg})_{max}$ to $(m_{bLg})_{3rd}$ and $(m_{Lg}(f))_{max}$ to $(m_{Lg}(f))_{3rd}$, respectively.

Examining the coefficient of anelastic attenuation γ shows that a single-valued γ is probably inappropriate for the central and eastern United States. Instead, the empirically determined γ varies widely depending on the region and the size of the earthquake (only an empirical observation because of the different frequencies of a large earthquake versus a smaller earthquake), the distance of observations, and the propagational path of the waves. A frequency-dependent γ , even though its contribution to the magnitude computation is minimal, is a better parameter. The

investigation of a frequency-dependent γ emphasizes the need for further study of amplitude modeling and attenuation in the central and eastern United States if the purpose is to predict amplitudes as a function of earthquake magnitude.

This investigation recommends the following modifications to the NEIC procedure so that m_{bLg} can be used to robustly estimate M_w :

- 1) Use observations in the 150–1350 km range rather than the approximate 50–1200 km epicentral range.
- 2) Use Equations (2.6) and (2.7) to estimate M_w
- 3) Do not attempt to estimate M_w if m_{bLg} is greater than 5.3.

References

- Aki, K. (1967). Scaling Law of Seismic Spectrum, *J. Geophys. Res.*, **72**, 1217-1231.
- Atkinson, G. M. and D. M. Boore (1995). Ground-Motion Relations for Eastern North America, *Bull. Seism. Soc. Am.*, **85**, 17-30.
- Boore, D. M. (1983). Stochastic Simulation of High-Frequency Ground Motions Based on Seismological Models of the Radiated Spectra, *Bull. Seism. Soc. Am.*, **73**, 1865-1894.
- Boore, D. M. (2003). Simulation of Ground Motion Using the Stochastic Method, *Pure Appl. Geophys.*, **160**, 635-676.
- Brune, J. N. (1970). Tectonic Stress and the Spectra of Seismic Shear Waves from Earthquakes, *J. Geophys. Res.*, **75**, 4997-5009.
- Brune, J. N. (1971). Correction, *J. Geophys. Res.*, **76**, 5002.
- Cartwright, D. E. and M. S. Longuet-Higgins (1956). The Statistical Distribution of the Maxima of a Random Function, *Proc. Roy. Soc. London, Ser A237*, **237**, 212-232.
- Ewing, M., W. S. Jardetzky, and F. Press (1957). *Elastic Waves in Layered Media*, McGraw-Hill, New York.
- Frankel, A., C. Muller, T. Barnhard, D. Perkins, E. V. Leyendecker, N. Dickman, S. Hanson, and M. Hopper (1996). Oper-File Report 96-532. http://pubs.usgs.gov/of/1996/532/OFR-96-532_508.pdf
- Hanks, T. C. and H. Kanamori (1979). A Moment Magnitude Scale, *J. Geophys. Res.*, **84**, 2348-2350.
- Hanks, T. C. and R. K. McGuire (1981). The Character of High-Frequency Strong Ground Motion, *Bull. Seism. Soc. Am.*, **71**, 2071-2095.
- Herrmann, R. B. and A. Kijko (1983a). Short-Period *Lg* Magnitudes: Instrument, Attenuation, and Source Effects, *Bull. Seism. Soc. Am.*, **73**, 1835-1850.
- Herrmann, R. B. and A. Kijko (1983b). Modeling Some Empirical Vertical Component *Lg* Relations, *Bull. Seism. Soc. Am.*, **73**, 157-171.
- Herrmann, R. B. (1985). An Extension of Random Vibration Theory Estimates of Strong Ground Motion to Large Distances, *Bull. Seism. Soc. Am.*, **75**, 1447-1453.

- Herrmann, R. B. (1987). Broadband *Lg* Magnitude, *Seismol. Res. Lett.*, **58**, 125-133.
- Herrmann, R. B., H. Benz, and C. J. Ammon (2011). Monitoring the Earthquake Process in North America, *Bull. Seism. Soc. Am.*, **101**, 2609-2625
- Iyengar, R. N. and K. T. S. R. Iyengar (1969). A Nonstationary Random Process Model for Earthquake Accelerograms, *Bull. Seism. Soc. Am.*, **59**, 1163-1188.
- Kennett, B. L. N. (1983). *Seismic Wave Propagation in Stratified Media*, Cambridge University Press, Cambridge England.
- Kennett, B.L. N. (1986). *Lg* Waves and Structural Boundaries, *Bull. Seism. Soc. Am.*, **76**, 1133-1141.
- Nuttli, O. W. (1973). Seismic Wave Attenuation and Magnitude Relations for Eastern North America, *J. Geophys. Res.*, **78**, 876-885.
- Nuttli, O. W. (1986a). *Lg* Magnitudes of Selected East Kazakhstan Underground Explosions, *Bull. Seism. Soc. Am.*, **76**, 1241-1251.
- Nuttli, O.W. (1986b). Yield Estimates of Nevada Test Site Explosions from Seismic *Lg* Waves, *J. Geophys. Res.*, **91**, 2137-2151.
- Oliver, J. and M. Ewing (1957). Higher modes of continental Rayleigh waves, *Bull. Seism. Soc. Am.*, **47**, 187-204.
- Oliver, J. and M. Ewing (1958). Normal modes of continental Rayleigh waves, *Bull. Seism. Soc. Am.*, **48**, 33-49.
- Press, F. and M. Ewing (1952). Two slow surface waves across North America, *Bull. Seism. Soc. Am.*, **42**, 219-228.
- Vanmarcke, E. H. and S. P. Lai (1980). Strong-Motion Duration and RMS Amplitude of Earthquake Records, *Bull. Seism. Soc. Am.*, **70**, 1293-1307.
- Working Group on Magnitude Measurements (2011). Summary of Magnitude Working Group Recommendations on Standard Procedures for Determining Earthquake Magnitudes from Digital Data, http://www.iaspei.org/commissions/CSOI/Summary_WGRecommendations_20110909.pdf
- Yang, X. (2002). A Numerical Investigation of *Lg* Geometrical Spreading, *Bull. Seism. Soc. Am.*, **92**, 3067-3079.

Zhang, T. and T. Lay (1995). Why the *Lg* Phase Does Not Traverse Oceanic Crust, *Bull. Seism. Soc. Am.*, **85**, 1665-1678.

Vita Auctoris

Christopher Rigsby was born on 29 September 1985 in St. Louis, MO. He earned his B.S. from Fontbonne University in 2008, studying creative writing and mathematics. After an unexpected detour through Vanderbilt University Law School for 1.5 years, he began his master's degree in the Department of Earth and Atmospheric Sciences.

His current career plan is to work at an oil and gas company in Oklahoma City. His personal plan is to continue studying mathematics, seismology, computer programming, and foreign languages.